Development of New Nanocarriers for the Delivery of siRNA against *RUNX1/ETO* gene for the Treatment of Acute Myeloid Leukaemia

Milene Dalmina

A thesis submitted for the degree of
Doctor of Philosophy in Chemistry

School of Chemistry
Newcastle University
October 2019

Abstract

A new platform for the delivery of short interfering RNA (siRNA) was investigated. Polymer-coated AuNPs were functionalised with phosphorothioate modified (PS) nucleic acids. The PS-modification allows their conjugation onto AuNPs though the formation of Au-S bonds**.** The conjugation of PS-single strand oligonucleotide (PS-ssODN) on polymer-coated AuNPs resulted in high loading efficiency. Particles prepared with PS-siRNA, which is a double-stranded molecule, did not show loading of siRNA. The addition of three PS-modifications on the siRNA (3PS-siRNA) did not improve the loading efficiency. These observations suggest that the conjugation of PS-ssODN onto AuNPs was not exclusively driven by the Au-S bond formation, but that the exposed bases within the single strand can also drive the conjugation onto Au, presumably through the formation of Au-N bonds. Work in this thesis also investigated the introduction of pH-sensitivity into a siRNA delivery platform. An important feature of any nanocarrier is its stimuli response towards an intracellular trigger. Polymers presenting pH-responsiveness are potentially useful in siRNA delivery as the endosomal acidic environment within the target cells can be harnessed to trigger siRNA release. The pH-sensitivity of model hydrazone and imine bonds was evaluated. The model hydrazones tested did not show the required pH-sensitivity, however, two imines were identified stable at pH 7 and hydrolyzed at pH 5, a suitable pH-sensitivity for siRNA applications. Time limits prevented the further development of the imine system, however, the model hydrazone was successfully appended onto polymer scaffolds and conjugated onto AuNPs. Their complexation with siRNA resulted in 60 % loading efficiency, however, the particles did not release siRNA after incubation in a buffer at pH 5.0. This observation confirms the poor pH-sensitivity of hydrazone bonds. Further studies must be developed to determine the pH-sensitivity of imines in polymer systems, and thus, evaluate its potential as candidates for the safe delivery of siRNA.

Acknowledgements

First, I would like to thank my PhD supervisors Dr David A Fulton and Prof Olaf Heidenreich for their continuous support and encouragement during these four years. I have received from my PhD supervisors Dr David A Fulton and Prof Olaf Heidenreich. Their extensive knowledge of chemistry and drug delivery, and their enthusiasm for research helped my development as a scientist and I will be grateful for the opportunity to be part of their research groups. Being a PhD student from a completely different culture and from a such far country, I cannot emphasise enough how important was to me to have a good relationship with my supervisors. They were very welcoming and they were concerned not only with my results and productivity, but also with my well-being, always encouraging me to enjoy my time in Newcastle and not thinking only about science. I am truly grateful for their support.

I am grateful for the support from past and current members from DAF group. They helped me find my feet in the chemistry labs, teaching me techniques that I had not seen before. I would like to extend my gratitude to Dr Luke Dixon, Dr Claudia Ventura, Dr Antonio Ruiz-Sanchez, Dr Gema Dura, Dr Michael Bracchi, Dr Dan Coleman, Patrick Higgs and Cheney Leung, whose support has proved invaluable during my 4 years in Newcastle University. I would also like to express my gratitude to past and current members from the Chemical Nanoscience Laboratory outside Fulton's group, including Dr Osama El-Zubir, Dr Colette Whitfield, Dr Sam Bhat, Dr Sam Lunn, Dr Rachel Little, Dr Shams Ali Dr Glenn Lamming, Liam Mistry and Pablo Martinez. I cannot forget my MPharm student Siraaj Bukera and my Erasmus student Luisa Camerin. Their help was invaluable and I was truly lucky to have had such good students. I really appreciated their effort and dedication to the research project.

I would also like to extend my gratitude to the amazing and committed researchers working on Olaf's group. Even though I was not very present in their routine, they all made me feel as a part of the Olaf's family. Special mention to Dr 'Kasia' Szoltysek, Dr Ricky Tirtakusuma, Dr Lynsey McKenzie, Dr Helen Blair, Hesta McNeill, Dr Mojgan Reza, Dr Asmida Isa, Dr Hasan Issa, Melanie Beckett, Yuzhe Shi, Shalini Sankar, Mankaran Singh, Rachel Cameron and Dr Edward Law. I am truly grateful for your help and support during the last years and I will not forget all the amazing 'tea moments' that we shared.

I am extremely lucky to have so many friends in a foreign country. I would like to say a special thanks to my buddies since day one, Gema Dura, Cristina Navarro and

Rachel Little. Thank you for all the scientific support, but also and mostly thank your for the emotional support during my 4 years in Newcastle. A special thanks to my friends Andres Aldana, Arlene Arias and Andres Gonzales for taking my mind out of work, stress and anything that made me feel depressed. Also, I would like to mention my friends Asmida, Kasia, Ricky, and Yuzhe. Thank you for the hiking adventures where we could experience the best of UK.

Lastly, I would like to thank my family, my mum, my sisters, the cutest nephew in the world and my grandmother, whose support was invaluable during my PhD. Thank you for supporting me when I was desperate about my future or when I just wanted to come back home. I could not have done without them and I am truly grateful to have such a beautiful family.

Table of contents

List of Abbreviations

λ	Wavelength (lambda)
μL	Microliter
μm	Micrometre
^{13}C NMR	Carbon-13 nuclear magnetic resonance spectroscopy
^{1}H NMR	Hydrogen-1 nuclear magnetic resonance spectroscopy
3PS-siLUC	siRNA targeting the luciferase gene modified with three phosphorothioates
3PS-siRNA	siRNA modified with three phosphorothioates
AGO2	Argonaute 2
AIBN	2,2'-azobis(2-methylpropionitrile)
AML	Acute myeloid leukaemia
AP-1	Activation protein-1
AuNPs	Gold nanoparticles
$CDCl_3$	Deuterated chloroform
CTA	Chain transfer agent
CTPA	4-Cyano-4- (thiobenzoylthio)pentanoic acid
CCND2	Cyclin D2
D_2O	Deuterium oxide
DCM	Dichloromethane
DDT	Dithiothreitol
DLS	Dynamic light scattering
DMF	Dimethylformamide
DP	Degree of polymerisation
dsRNA	Double-stranded RNA
EDG	Electron donating groups
EPR	Enhanced permeability and retention effect
EWG	Electron withdrawing groups
FAB	French-American-British classification
FCS	Fetal calf serum
FTIR	Fourier-transform infrared spectroscopy
GPC	Gel permeation chromatography
GSH	Glutathione
HEMA	2- hydroxyethyl methacrylate

HiDAC	High doses of cytarabine
HSCs	Haematopoietic stem cells
LCST	Lower critical solution temperature
miRNA	microRNA
M_n	Average molecular weight distribution
M_w	Molecular weight
NHR	Nervy homology regions
nm	nanometre
PdI	Polydispersity index
PEG	Polyethylene glycol
PEGMA	Poly(ethylene glycol) methyl ether methacrylate monomer
PEI	Polyethyleneimine
PHEMA	Poly(ethylene glycol) methacrylate monomer
Pre-miRNA	precursor miRNA
Pri-miRNA	Primary miRNA transcripts
PS-siMM	siRNA targeting a mismatch gene modified with phosphorothioate
PS-siRE	siRNA targeting a *RUNX1/ETO* gene modified with phosphorothioate
PS-siRNA	siRNA modified with phosphorothioate
PS-ssODN	Single strand oligonucleotide modified with phosphorothioate
RAFT	Reversible addition-fragmentation chain transfer
RES	Reticuloendothelial system
RHD	Runt homology domain
RISC	RNA-Induced Silencing Complex
RNAi	RNA interference
siLUC	siRNA targeting the *luciferase* gene
siRNA	Short interfering RNA
SPR	Surface plasmon resonance
ssODN	Single strand oligonucleotide
TBE buffer	Tris-Borate-EDTA buffer
TEM	Transmission electron microscopy

List of Figures

List of Schemes

List of Tables

Chapter 1
Introduction

1. Introduction

Acute myeloid leukaemia (AML) is an uncontrolled clonal proliferation of the myeloid lineage progenitors in the bone marrow and in the blood.[1] The disease classification and prognosis is based on several cytogenetic abnormalities, such as the translocation *t(8;21) (q22;q22),* also called *RUNX1/ETO*.[2] The resulting RUNX1/ETO fusion protein is associated with cell proliferation and self-renewal capacity of the myeloid progenitor, leading to leukemic proliferation and AML maintenance.[3,4] Treatment of AML usually comprises intensive and genotoxic chemotherapy, causing undesired side effects which can severely decrease the quality of life of patients.[5] Therefore, depletion of *RUNX1/ETO* by short interfering RNAs (siRNA) presents as an interesting approach for the better prognosis and treatment of AML. The translation of synthetic siRNA from *in vitro* applications into therapeutic use still remains a major challenge for the therapy success.[6] The poor pharmacokinetics properties of siRNA requests the development of a delivery platform to safely transport and protect siRNA molecules against enzymatic degradation and fast renal clearance in the blood circulation.[7] In this work, the development of two different nanocarriers is discussed. The nanocarriers were designed to perform different functions at each stage of pharmacokinetics, promoting prolonged blood circulation, efficient cellular uptake and fast siRNA release.

1.1 Acute myeloid leukaemia

Acute myeloid leukaemia is a type of blood cancer that affect the myeloid cell lineage and is characterised by the uncontrolled proliferation of myeloid cells that fail to differentiate during the process of haematopoiesis.[8] Haematopoiesis takes place in the bone marrow and it leads to the differentiation of haematopoietic stem cells (HSCs) to generate all blood cell types. In normal haematopoiesis process, HSCs are capable of self-renewing and generate multipotent progenitors, that will further differentiate into the precursors of the myeloid and lymphoid lineage.[9]

At the onset of AML, the myeloid progenitors can undergo genetic mutations which leads to increased proliferation and self-renewing, and decreased differentiation into mature myeloid cells.[10] These genetic mutations result in uncontrolled production of immature (poorly differentiate) myeloid cells, called blasts, which overrun the bone marrow niche. The accumulation of blasts leads to bone marrow failure, resulting in decreased production of mature cells from the myeloid lineage (erythrocytes, leukocytes and platelets).[11] The clinical manifestations of AML reflects the

accumulation of malignant blasts in the bone marrow and peripheral blood, which includes anaemia, leucocytosis and thrombocytopenia. Patients usually show signs of fatigue, anorexia and weight loss.[12] The diagnosis of AML is usually confirmed by the presence of > 20 % blast cells in the peripheral blood or bone marrow, and also when several well characterised cytogenetic abnormalities associated with the disease are detected.[5,12]

AML is characterised as a clonal malignant disorder on account of the clonal expansion of a single malignant cell (Figure 1.1).[1] After genetic alteration on a progenitor cell, differentiation will be inhibited whilst self-renewing and proliferation will increase, resulting in the expansion of the malignant cells. As leukaemia progresses, some cells will gain additional mutations, producing sub-clonal populations.[13] Although all malignant cells will maintain the initial mutation, the genetic mutations accumulate and the subclones progress in parallel, increasing the heterogeneity of the tumour. Thus, the identification of the products from the genetic alterations of an original malignant cell is a very attractive approach for the treatment of AML.

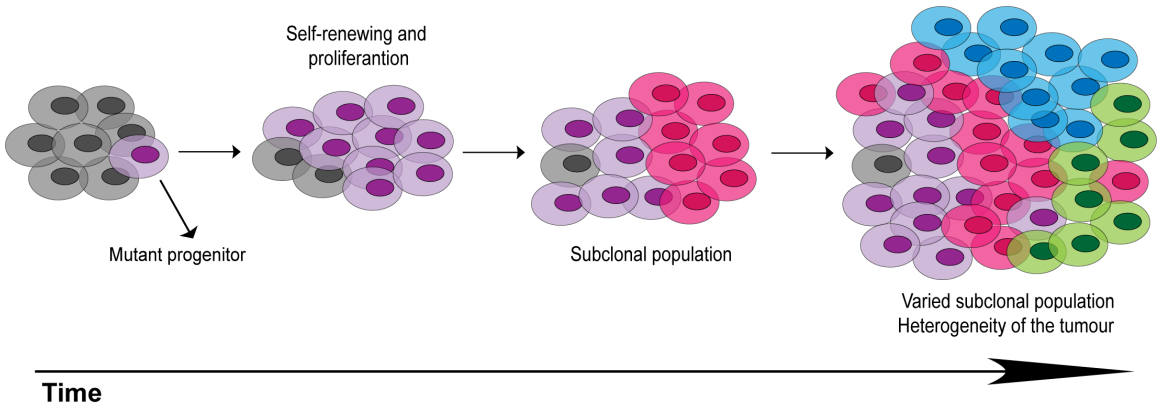

Figure 1.1: Clonal evolution in AML. The colours represent different sub-clonal populations. A single mutant cell can lead to clonal expansion with further genetic mutations creating sub-clonal populations in parallel, increasing the heterogeneity of the tumour.

1.1.2 Incidence and classification of AML

AML is the most common acute leukaemia in adults, and its estimated that 3,100 new cases are diagnosed every year (more than 8 per day), representing ~ 1 % of all cancer cases in the UK. The number of new cases in 2016 in the UK was 1,283 cases in women and 1,673 case in men. The incidence in the UK of AML have increased more than 20 % over the last 25 years.[14] Further studies by Dores *et al.,*[15] showed higher AML incidence rate according to the patient age, presenting 0.8 %, 1.5 %, 4.3 %, 23.1 % and 28.7 % for age groups 0-1, 1-4, 5-19, 40-59 and 60-74, respectively.

These observations largely reflect the higher incidence for AML in older people, a population that is related with poor prognosis of the disease.

AML had been first divided into 8 subtypes categories by the French-American-British cooperative group (FAB).[16] They subdivided AML according to the cellular type, morphology and differentiation status into the categories: **M0** (undifferentiated acute myeloblastic leukaemia), **M1** (acute myeloblastic leukaemia with minimal maturation), **M2** (acute myeloblastic leukaemia with maturation), **M3** (acute promyelocytic leukaemia), **M4** (acute myelomonocytic leukaemia), **M5** (acute monocytic leukaemia), **M6** (acute erythroid leukaemia) and **M7** (acute megakaryoblastic leukaemia). However, since the advance of cytogenetics and the identification of unique biomarkers that can improve the diagnostic criteria and dictate the patient prognosis, the World Health Organization (WHO) combined the old FAB classification and the most recent cytogenetics abnormalities into a new and more complete classification (Table 1.1 and Table 1.2).[17]

Table 1.1: World Health Organization (WHO) classification of AML. Adapted from Arber, et al.[17]

Classification	Description
AML with recurrent genetic abnormalities	AML with t(8;21)(q22;q22.1);RUNX1-RUNX1T1 AML with inv(16)(p13.1q22) or t(16;16)(p13.1;q22);CBFB-MYH11 APL with PML-RARA AML with t(9;11)(p21.3;q23.3);MLLT3-KMT2A AML with t(6;9)(p23;q34.1);DEK-NUP214 AML with inv(3)(q21.3q26.2) or t(3;3)(q21.3;q26.2); GATA2, MECOM AML (megakaryoblastic) with t(1;22)(p13.3;q13.3);RBM15-MKL1 Provisional entity: AML with BCR-ABL1 AML with mutated NPM1 AML with biallelic mutations of CEBPA Provisional entity: AML with mutated RUNX1
AML with myelodysplasia-related changes	**Cytogenetic abnormalities sufficient to diagnose AML with myelodysplasia-related changes when > 20% PB or BM blasts are present and prior therapy has been excluded** Cytogenetic abnormalities Complex karyotype (3 or more abnormalities): *Unbalanced abnormalities:* −7/del(7q) del(5q)/t(5q) i(17q)/t(17p) −13/del(13q) del(11q) del(12p)/t(12p) i dic(X)(q13) *Balanced abnormalities:* t(11;16)(q23.3;p13.3) t(3;21)(q26.2;q22.1) t(1;3)(p36.3;q21.2)

Table 1.2: Continuation of WHO classification for AML.

Classification	Description
AML with myelodysplasia-related changes	t(2;11)(p21;q23.3) t(5;12)(q32;p13.2) t(5;7)(q32;q11.2) t(5;17)(q32;p13.2) t(5;10)(q32;q21.2) t(3;5)(q25.3;q35.1)
Therapy-related myeloid neoplasms	AML with genetic abnormalities associated with chemotherapy
AML not otherwise specified	AML with minimal differentiation AML without maturation AML with maturation Acute myelomonocytic leukaemia Acute monoblastic/monocytic leukaemia Pure erythroid leukaemia Acute megakaryoblastic leukaemia Acute basophilic leukaemia Acute panmyelosis with myelofibrosis
Myeloid sarcoma	**Myeloid sarcoma**
Myeloid proliferations related to Down syndrome	Transient abnormal myelopoiesis (TAM) Myeloid leukaemia associated with Down syndrome

1.1.3 Treatment of AML

The standard treatment for AML patients consists of two stages: induction and post-remission (or consolidation) therapy.[12] The induction therapy consists of a "7+3" regime scheme, which combines 7 days of continuous administration of cytarabine (interferes in the DNA synthesis by replacing cytosine) with 3 days of anthracycline (DNA damaging agent).[18] The induction therapy aims to reduce the bulk of leukemic blasts and induce complete remission of the disease. The induction therapy should be followed by the consolidation therapy in order to completely eradicate any residual disease and achieve lasting remission. The consolidation therapy is tailored to each individual, depending on the individual's age, health and leukaemia karyotype.[19] It can include high doses of cytarabine (HiDAC) administered over five days for approximately four weeks (total of 3 or 4 cycles) and co-administration of mitoxantrone. Consolidation therapy can also consists of HiDAC followed by autologous or allogenic stem cell transplantation.[20] Despite the advances of the current treatments, 10-40 % of AML patient do not achieve complete remission, which increase the risks of relapse, associated with poor prognosis.[19,21] Moreover, the poor prognosis for the elderly, who account for the majority of new cases, remains a concern. Even with the existing treatment, up to 70 % of patients over the age of 65 will die of AML within one year of diagnosis.[22] The current treatment for AML is extremely aggressive which can severely impair the quality of life of patients, leading to early and long-term undesired side-

effects, such as the development of treatment-related secondary cancers.[19] The cytogenetic abnormalities are the most critical factors in achieving complete remission and avoiding relapse in patients.[23] Thus, the development of new treatments targeting the products of these abnormalities is a promising strategy for a better prognosis of AML, especially for elderly and relapsed patients.

1.1.4 The translocation t(8;21)(q22;q22) and the leukemic fusion protein RUNX1/ETO

The chromosomal translocation t(8;21) is one example of cytogenetic abnormality that is highly prevalent in AML and results in the expression of the fusion protein RUNX1/ETO.[24] Chromosomal translocations occur when a segment of one chromosome is exchanged with a segment from a nonhomologous one, resulting in the expression of a chimeric fusion protein consisting of regions from both original chromosomes. The resulting fusion proteins are known to play an important role in the development of tumours and represent an important parameter for diagnosis and prognosis of several cancers, especially malignant haematological disorders.[25]

In the t(8;21) leukaemia (Figure 1.2 A), *RUNX1* gene from chromosome 21 fuses to *ETO* gene located on chromosome 8. The fusion usually occurs within breakpoints in intron 5 of *RUNX1* and in intron 1a-1b of *ETO*.[2] This chimeric gene generates the fusion protein RUNX1/ETO (Figure 1.2 B) consisted of the 177 N-terminal amino acids of RUNX1 and the most of amino acids that are located on the C-terminus of ETO, presenting in total 752 amino acids.[26]

In normal cells, the *RUNX1* gene encodes RUNX1 protein that contains Runt homology domain (RHD). RHD facilitates RUNX1 binding to DNA and is indispensable for the regulation of haematopoiesis and homeostasis of HSCs.[27,28] The eight twenty-one (*ETO*) gene encodes ETO proteins that comprises four Nervy homology regions named NHR-1, NHR-2, NHR-3 and NHR-4 . The ETO proteins bind to different co-repressors, such as N-CoR and SMRT resulting in transcription repression.[29] In the case of t(8;21), the repressor activity of ETO inhibits the DNA-binding activity of RUNX1, and thus, defines the suppressive roles of RUNX1/ETO fusion protein is this subtype of leukaemia.[4,30]

The translocation *t(8;21)* is related with approximately 40 % of M2 subtype of AML (FAB classification) and 8 – 20 % of all AML cases. The translocation is also associated with 6 % of M1 subtype of AML and it is rarely detected in M4 and M5 AML subtypes.[2]

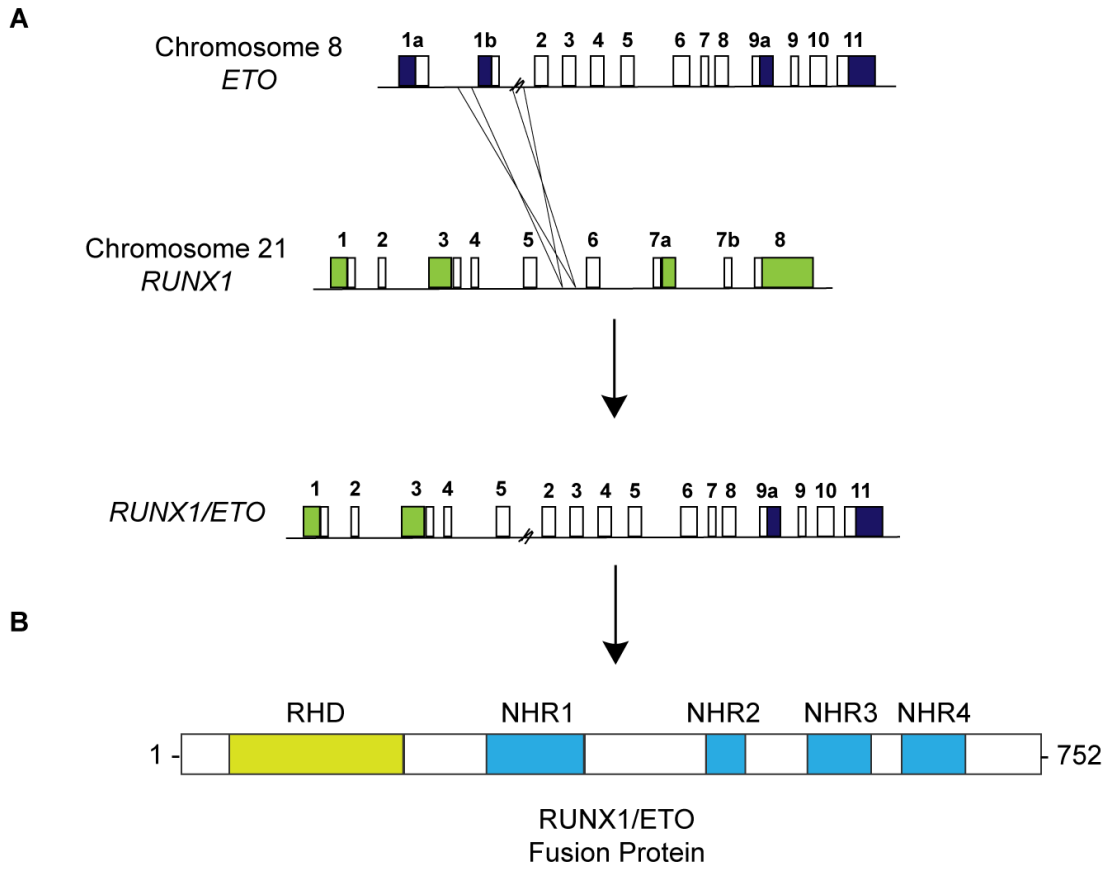

Figure 1.2: Schematic representation of the translocation t(8;21) (q22;q22). (A) Genomic structure of t(8;21). The breakpoint occurs in two possible locations in intron 1a-1b in *ETO* and one location in intron 5 in *RUNX1*. (B) Protein structure of RUNX1/ETO featuring 752 amino acids. The RHD domain of *RUNX1* is fused to most of the *ETO* including the NHR regions.[2,26]

The RUNX1/ETO fusion protein is a leukaemia initiator transcription factor that interferes with the RUNX1 function, inhibiting cell differentiation. The RUNX1/ETO protein is known to enhance leukemic cells proliferation and self-renewal of the myeloid progenitors, resulting on the development of AML.[31] The fusion protein affects a wide range of cellular mechanisms and can also contribute for the development of additional genetic abnormalities.[26] One of the main mutations associated with patients carrying the *t(8;21)* is the mutations in the c-KIT tyrosine kinase receptor. The oncogenic cooperativity between these oncoproteins leads to AML development and maintenance, and its usually associated with an aggressive leukemic phenotype and poor prognosis.[32] Moreover, Martinez-Soria, *et al.*[33] demonstrated that RUNX1/ETO cooperates with the activation protein 1 (AP-1) to drive cyclin D2 (CCND2) expression that is crucial to promote and maintain the progression of the cycling cells. Therefore, depletion of RUNX1/ETO reduces the expression of CCND2 and consequently, inhibits cell cycle and proliferation. The group also demonstrated that depletion on

RUNX1/ETO inhibited cell proliferation colony formation *in vitro*.[4,34] The *in vivo* depletion of RUNX1/ETO resulted in decreased tumour formation and increased median survival in a xenotransplantation model. Taken together, the knockdown of *RUNX1/ETO* by RNA interference (RNAi) therapy is a promising strategy for the treatment of AML.[3]

1.2 RNA interference therapy and short interfering RNAs

RNA interference (RNAi) therapy enables the control of protein expression by silencing the expression of an endogenous gene.[35] The RNAi mechanism was first described by Andrew Fire and Craig Mello in 1998.[36] Their work demonstrated the ability of exogenous double strand RNA (dsRNA) to sequence-specific silence gene expression in the nematode worm *Caenorhabditis elegans*, rendering them the Nobel Prize in Medicine of 2006. However, was only after the work of Hammond, *et al.*[37] that the RNAi mechanism was fully elucidated with the discovery of the RNA-Induced Silencing Complex (RISC).

The mechanism of RNAi (Figure 1.3) is triggered by the presence of long pieces of dsRNA in the cell cytoplasm (Figure 1.3 A). The dsRNA is then cleaved by the enzyme Dicer into smaller fragments known as short interfering RNA (siRNA).[35] The produced siRNA is incorporated into a protein complex called the RNA-Induced Silencing Complex (RISC).[38] A multifunctional protein contained within RISC, known as Argonaute 2 (AGO2), unwinds the siRNA. The guide strand (antisense strand) forms and activates RISC, whereas the passenger strand (sense strand) of the siRNA is cleaved.[39] The activated RISC selectively seeks out and degrades the complementary sequence of messenger RNA (mRNA) to the guide strand.[40] The activated RISC complex will continuously seek for additional mRNA targets, which further propagates gene silencing[41].

Another small RNA that produces RNAi effect includes the microRNAs (miRNA) (Figure 1.3 B), a stem-loop like structure featuring 21-25 nucleotides.[42] The miRNA pathway begins with endogenously encoded primary miRNA transcripts (pri-miRNAs) that are transcribed by RNA polymerase II and are processed by the Drosha enzyme complex to yield the precursor miRNAs (pre-miRNAs). These precursors are then exported to the cytoplasm by Exportin 5 and subsequently bind to the Dicer enzyme complex, which processes the pre-miRNA for loading onto the AGO2–RISC complex.[42,43]

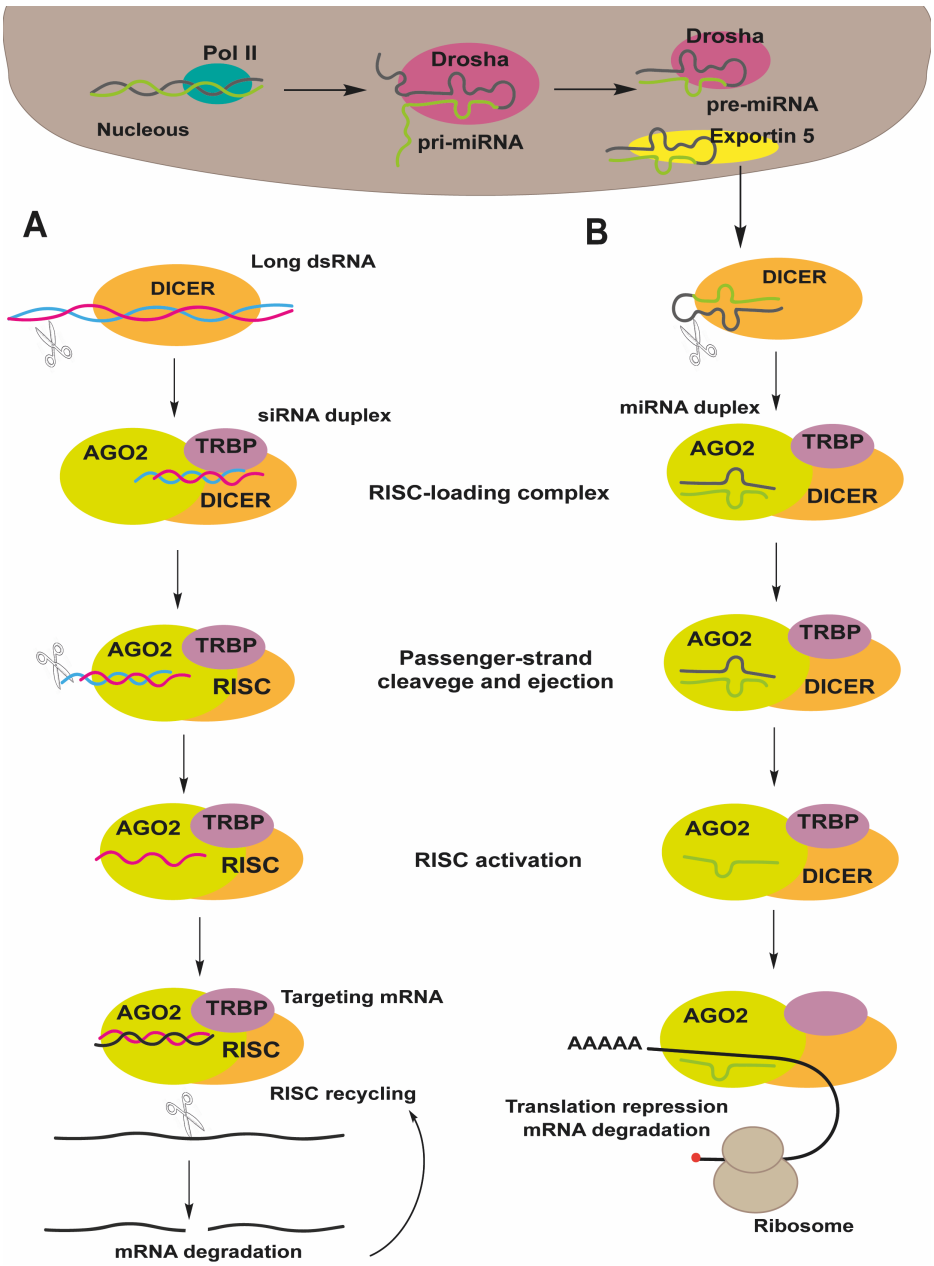

Figure 1.3: Mechanism of RNA interference. (A) Long dsRNA is cleaved into siRNA by the Dicer enzyme and its incorporated into the RISC complex containing the AGO2 enzyme. AGO2 cleaves the passenger (sense) strand of siRNA so that active RISC containing the guide (antisense) siRNA strand recognises the target sites of the complimentary mRNA. AGO2 then promotes the cleavage of the mRNA and the activated RISC is recycled. (B) The pre-miRNAs are formed by the endogenously encoded pri-miRNAs and are then exported to the cytoplasm by Exportin 5. The pre-miRNA binds to the Dicer enzyme complex, where it is processed for loading onto the AGO2–RISC complex and promote the mRNA cleavage.

Elbashir, *et al.*[44] showed the RNAi effect in mammalian cells by introducing synthetic siRNA sequences and proved that exogenous siRNAs could indeed achieve sequence-specific gene silencing.[44] Synthetic siRNA molecules are well-defined structures of double strand RNA of 19-22 nucleotides with 2 nucleotide overhangs at either 3' ends.[35,45] The antisense sequence (guide strand) of the siRNA is designated to be complementary to the sequence of the targeted mRNA. Once siRNAs are

internalised in the cell cytoplasm, it is directly loaded into the AGO2-RISC complex, activating the RNAi mechanism (Figure 1.3) to seek out and promote degradation of the targeted mRNA. As siRNAs enter the RNAi pathway later (skipping the DICER step), it is less likely to interfere in the endogenous miRNA pathway,[46] and therefore it is an attractive candidate for RNAi therapeutics.

1.3 Application and challenges of siRNA delivery *in vivo*

The first successful application of siRNA *in vivo* was reported by McCaffrey, *et al.*[47] only one year after the application of synthetic siRNA in mammalian cells demonstrated by Elbashir and co-workers.[44] The group co-injected high doses of luciferase-expression plasmid with naked siRNA targeting the firefly luciferase into the tail vein of the mice. The mice treated with the targeted siRNA showed a decrease in the luminescence signal of 70 %. Moreover, the group also evaluated the co-injection of the luciferase plasmid with an unrelated siRNA sequence. The mice treated with the siRNA unrelated sequence did not show decrease in luciferase expression, showing the specific gene silencing of siRNA molecules *in vivo*. The delivery method used by the group is based on the injection of large volumes of the solution and its called the hydrodynamic delivery method. Although the group showed promising results, this method results in hemodynamic changes in the blood flow and lack of tissue specificity (molecules mainly accumulate in the liver), limiting its use for clinical applications. Thus the delivery of nucleic acids to the target cells remains a major obstacle to translate the siRNA therapeutics into clinical applications.

In order to activate the RNAi pathway, siRNA molecules must travel through the bloodstream and cross the cellular membrane of the target cell. However, siRNAs are hydrophilic and polyanionic molecules with high molecular weight ~ 13 kDa and, therefore, are too large and negatively charged to successfully enter the cell cytoplasm.[48] Localised siRNA delivery, when siRNA molecules are directly injected into the target tissue, results in high bioavailability and consequently, effective RNAi silencing.[49] However, localised administration is only available for a few tissues (e.g. eye, skin) and superficial tumours, being the systemic administration ideal as a non-invasive method for the treatment of a large number of diseases. Naked siRNA presents poor pharmacokinetics when administered systemically, once it is subjected to fast renal clearance and degradation by nucleases in the blood.[50] Hence, for the systemic delivery of siRNA the use of nanocarriers is essential to achieve efficient transfection into the target cell or tissue.

The success of the nanocarriers will be dependent on the capacity of the delivery platform to overcome the biological barriers associated with *in vivo* siRNA delivery (Figure 1.4). To overcome these challenges, the nanocarrier must be able to protect the siRNA from the fast renal clearance and from degradation by nucleases, accumulate on the desired cell or tissue, facilitate the cellular uptake usually by endocytosis, promote the siRNA release in the cytosol of the target cell and present negligible toxicity.

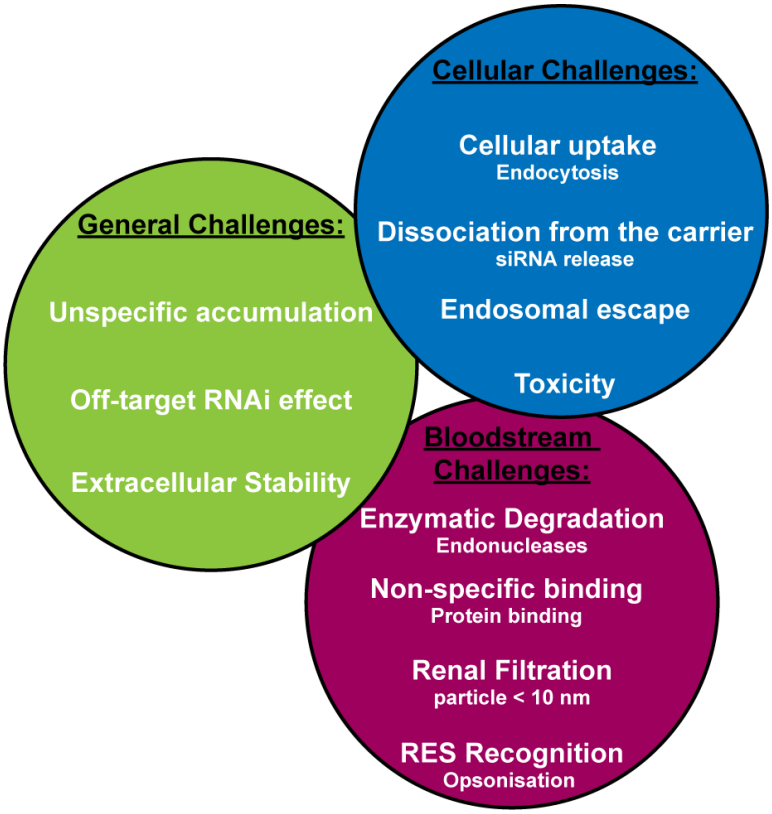

Figure 1.4: Biological barriers associated with the *in vivo* delivery of siRNA.

The particle size of the nanocarriers is an important factor in order to overcome the biological barriers for *in vivo* applications. Nanoparticles smaller than < 10 nm (or < 50 kDa) are rapidly excreted through the renal clearance,[45] reducing the particle half-life and consequently, the accumulation into the target tissue. Particles presenting large particle size (> 200 nm) are easily recognised by the reticuloendothelial system (RES), a phenomenon known as opsonisation that results in the phagocytosis of the particles and decreased blood circulation time.[51] Moreover, due to the high proliferation rate and unbalanced growth of solid tumours, the angiogenesis (formation of new blood vessels) results in new blood vessels structurally abnormal with wide fenestrations (large spaces), allowing the extravasation of molecules presenting < 200 nm size from

the blood stream to the tumour tissue. This phenomenon is known as Enhanced Permeability and Retention effect (EPR effect)[52] and is a specific feature of tumour vessels, not occurring in healthy tissue (such as bone marrow sinusoids). The EPR effect facilitates the passive accumulation of prolonged-circulation nanocarriers (size < 200 nm) in the tumour site. Thus, particles between 10 nm and 200 nm are ideal for delivery applications.

The particle surface charge is also an important factor for the development of nanocarriers. Positively charged nanoparticles are usually exploited for siRNA delivery purposes. The positive charges are effective for loading siRNA due to electrostatic interactions with the polyanionic molecule.[53] In addition, the negative charges of the cellular membrane enhances the cellular uptake of positively charged nanoparticles, resulting in high transfection efficiencies of these particles *in vitro.* However, *in vivo* applications result in non-specific binding with negatively charged proteins in the bloodstream, leading to recognition by the RES system and removal of the nanoparticles from the blood vessels.[45] Hence the minimum surface charge should be maintained for *in vivo* applications of nanocarriers. Neutrally charged nanoparticles present low colloidal stability due to particle aggregation, therefore, a sterical stabilisation is needed. Polyethylene glycol (PEG) is a hydrophilic polymer that when added to nanoparticles can substantially decrease RES recognition. Because of its inherent hydrophilicity and steric repulsion effects, PEG reduces phagocyte interactions and complement activation,[54] providing at the same time colloidal stability to the formulations. In addition, PEG has proved to be safe and effective in prolonging the half-life of many nanocarriers.[55–58] It also allows the attachment of targeting moieties that enable accumulation of the nanoparticles only in the target tissue. Targeting nanoparticles to specific tissues results in enhanced accumulation and specific cellular internalisation of siRNA, decreasing off-target RNAi effects.

After cellular uptake and internalisation of the nanocarriers by endocytosis, the particles often become entrapped in an endocytic vesicle, called endosome.[59] The escape from the endosome membrane and release of the siRNA cargo into the cytosol is vital for the perpetuation of the RNAi machinery. The intracellular trafficking (Figure 1.5) of siRNA begins in the early endosome, where the pH environment is ~ 6.0 – 5.5 and is rapidly carried to the late endosome, where the pH decreases rapidly (~ 5.0). Subsequently, the nanoparticles trafficking continues until it reach the lysosomes vesicles, in which the pH decreases further (~ 4.5) and contains a variety of enzymes (nucleases) that promote the degradation of siRNA.[56,60]

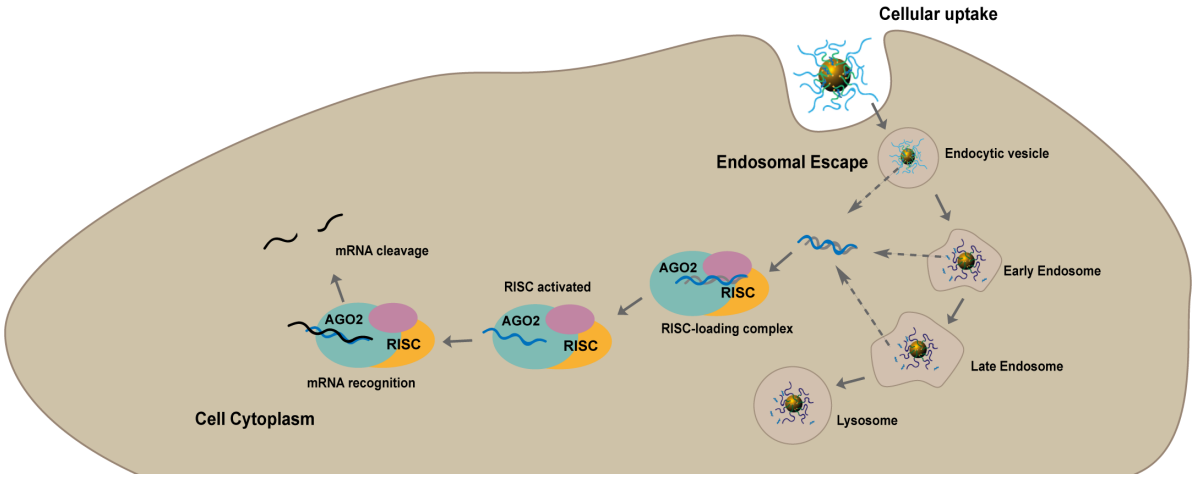

Figure 1.5: Cellular uptake of the nanocarriers by endocytosis and endosomal escape for the perpetuation of the RNAi mechanism .

Strategies that could stimulate the siRNA release and endosomal escape have been extensively studied. Cationic polymers, such as polyethyleneimine (PEI) can escape from the endosomes by a phenomenon known as the “proton-sponge effect” (Figure 1.6). In this approach, the positive charges of the polymer promote a buffering effect inside the endosome vesicle, which leads to an increase of the influx of protons and counter-ions. This phenomenon results in an osmotic swelling followed by membrane rupture, allowing the nanocarriers to escape from the endosome into the cytoplasm.[56,61]

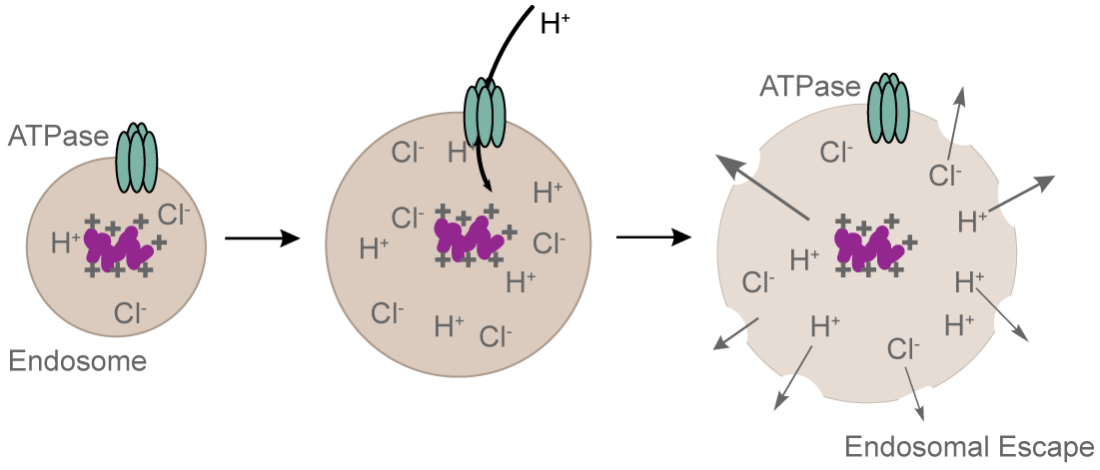

Figure 1.6: Endosomal escape by "Proton-sponge Effect". Cationic polymer is internalised in the endocytic vesicles called endosomes. The positive charges of the polymer cause influx of protons and counter-ions resulting in the increase of the osmotic pressure. The endosome swells causing membrane rupture and release of the contents.

The development of a new nanocarrier for efficient delivery of siRNA demands a deep understanding of the interaction mechanisms between nanoparticles, cells and

tissues and blood circulation. The nanocarriers must be thoroughly designed to overcome the challenges regarding the clinical applications of siRNA. The development of nanocarriers that present features that can be triggered in specific conditions, such as the endosome compartment, are crucial for siRNA delivery strategies.

1.4 Nanocarriers for siRNA delivery

The main classes of delivery platforms are categorised in viral and non-viral vectors. Due to the natural ability of viruses to transfect cells with genetic material, viral vectors have been studied for the delivery of therapeutic nucleic acids.[62] Viruses such as lentivirus, adenovirus, retrovirus and adeno-associated virus can be transformed into delivery systems by changing part of the virus genome with a therapeutic nucleic acid.[54,63] However, viral vectors presented high cytotoxicity and immunogenic problems during clinical trials,[63,64] limiting the use of these vectors for clinical applications. Thus, synthetic approaches have been presented as exciting alternatives for the delivery of nucleic acids in clinical applications, showing improved safety and more facile manufacture in large scales.

The non-viral vectors comprise nanoparticle like lipid-based platforms, polymeric nanoparticles and inorganic nanoparticles (such as iron oxide nanoparticles and gold nanoparticles).

1.4.1 Lipid-based nanoparticles

Lipid-based delivery systems have been extensively reported for siRNA delivery as liposomes or lipid nanoparticles. They are usually formed from the disposition of a lipid bilayer in aqueous environment, forming an unilamellar or multilamellar sphere with an aqueous core that can load siRNA.[65] Cholesterol is commonly used as a component of a delivery platform due to its lipophilic properties and cellular transport mechanisms. The addition of cholesterol to the formulation increases the stability of the lipid bilayer[66] and it can also facilitate the cellular uptake of the nanocarriers mediated by endocytosis.[67,68] Cationic lipids such as 1,2-dioleoyl-sn-glycero-3-phosphatidylcholine (DOPC) are usually included into liposome formulations to facilitate endocytosis and siRNA loading.[69] However, these lipids can have cytotoxic effects and fast clearance of the body on account of their positive charges.[70] To overcome the cytotoxicity challenges of cationic liposomes, PEG can be added to the formulations. However, pegylated liposomes can show decreased transfection

efficiencies.[71] Although liposomes are popular siRNA delivery platforms, concerns regarding the toxicity of cationic lipids still remains. Despite these problems, lipid-based delivery platforms have been successfully applied into clinics. Onpattro® by Alnylam Pharmaceuticals has been recently approved for the treatment of a neurodegenerative disease. The formulation is the first RNAi drug into clinics and it will be further discussed.

1.4.2 Polymeric nanoparticles

An alternative to lipid-based nanocarriers is the use of synthetic polymers as components of siRNA delivery platforms. Polymeric micelles are formed by self-assembly of block copolymers where one or more of the blocks convey an amphiphilic nature to the polymer system, resulting in spherical particles when placed in aqueous solvents.[72] The concept of polymeric micelles for drug delivery was introduced by Kataoka's group in 1992 (Figure 1.7).[73] The group developed the block copolymer **PEG-PAsp**, where the hydrophobic drug **doxorubicin** was conjugated onto the **PAsp** block through a covalent bond. The final copolymer **PEG-PAsp-DOX** formed spherical micelles of controlled size (< 100 nm), featuring a hydrophobic core and a hydrophilic outer-layer.

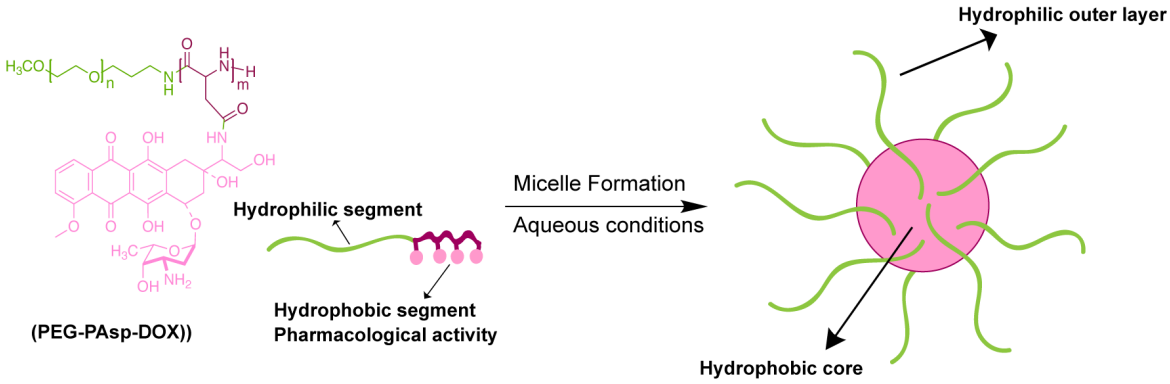

Figure 1.7: Micelle formation in aqueous solutions by self-assembly of **PEG-PAsp-DOX** copolymers.[73]

Cationic polymers are often included in polymeric micelles for complexation with siRNA through the electrostatic interactions with the negative charges of the nucleic acid sequence.[74] Pujol *et al.*[75] developed a polymeric nanoparticle consisted of two amphiphilic diblock copolymers, **PEG-*b*-PCL** and **PDMAEMA-*b*-PCL** (Figure 1.8). The self-assembly of the diblock copolymers resulted in monodisperse micelles with varied hydrodynamic diameters (ranging from 30 – 100 nm) depending on the copolymer

ratio. They further evaluated the gene knockdown efficiency and toxicity of particles carrying siRNA targeting the luciferase gene. The particles were prepared in different ratios of **PEG-*b*-PCL** and **PDMAEMA-*b*-PCL** to evaluate the cytotoxic effect of positively charged particles. The group demonstrated that cytotoxicity increased when higher ratios of the cationic polymer were used. From the comparison between gene knockdown efficiency and cytotoxicity, the group could determine the optimal formulation (formulation that presented the highest gene knockdown and the lowest cytotoxicity) to efficiently promote gene silencing without associated toxicity.

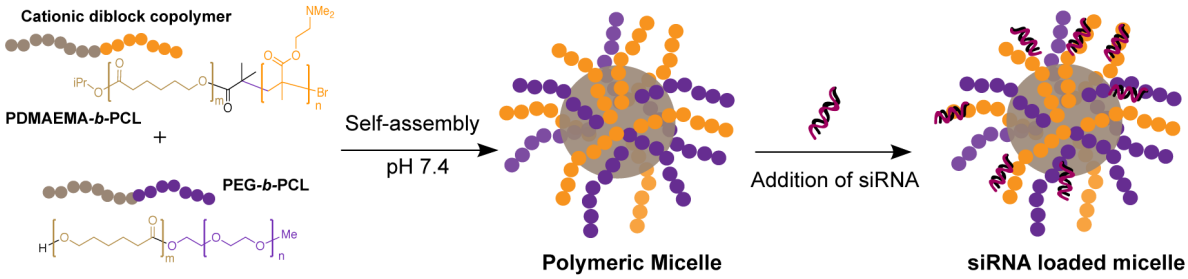

Figure 1.8: Polymeric nanoparticle for siRNA delivery. The nanoparticles were formed by the self-assembly of the amphiphilic copolymer **PEG-*b*-PCL** and the cationic copolymer **PDMAEMA-*b*-PCL**.[75]

Cationic polymers can also be easily complexed with siRNA on its own, forming stable particles called polyplexes.[76] A good example is poly-lysine (PLL), a small polypeptide of the essential amino acid L-lysine[45] which was one of the first cationic polymers to be used as a nucleic acid delivery platform.[77] However, the high cytotoxicity of PLL and lack of buffering capacity results in poor endosomal escape, limiting its application into clinics.[78] Besides the natural capability of cationic polymers to load nucleic acids on account of the charge ionic interactions, cationic polymers have also showed to facilitate the endosomal escape through the “proton-sponge” effect.[49] PEI is considered the gold standard for nucleic acid transfection on account of its high buffering capacity.[79] Yin, *et al.*[80] demonstrate the transfection efficiency *in vivo* of polyplexes formed by a thiol modified PEI-deoxycholic acid (**TP-DA-PEI**) (Figure 1.9). The polymer **TP-DA-PEI** was crosslinked with a thiolated siRNA to form more compact and stable polyplexes on account of the formation of disulfides bonds. The particles presenting hydrodynamic diameters of ~ 200 nm showed great stability in serum for 48 h and high transfection efficiency in A549 cells (adenocarcinoma). The group also demonstrated the *in vivo* antitumor effect of polyplexes carrying siRNA targeting the VEGF gene. After systemic administration on tumour-bearing mice, the

cross-linked polyplexes showed successful transfection of siRNA and significant tumour growth inhibition.

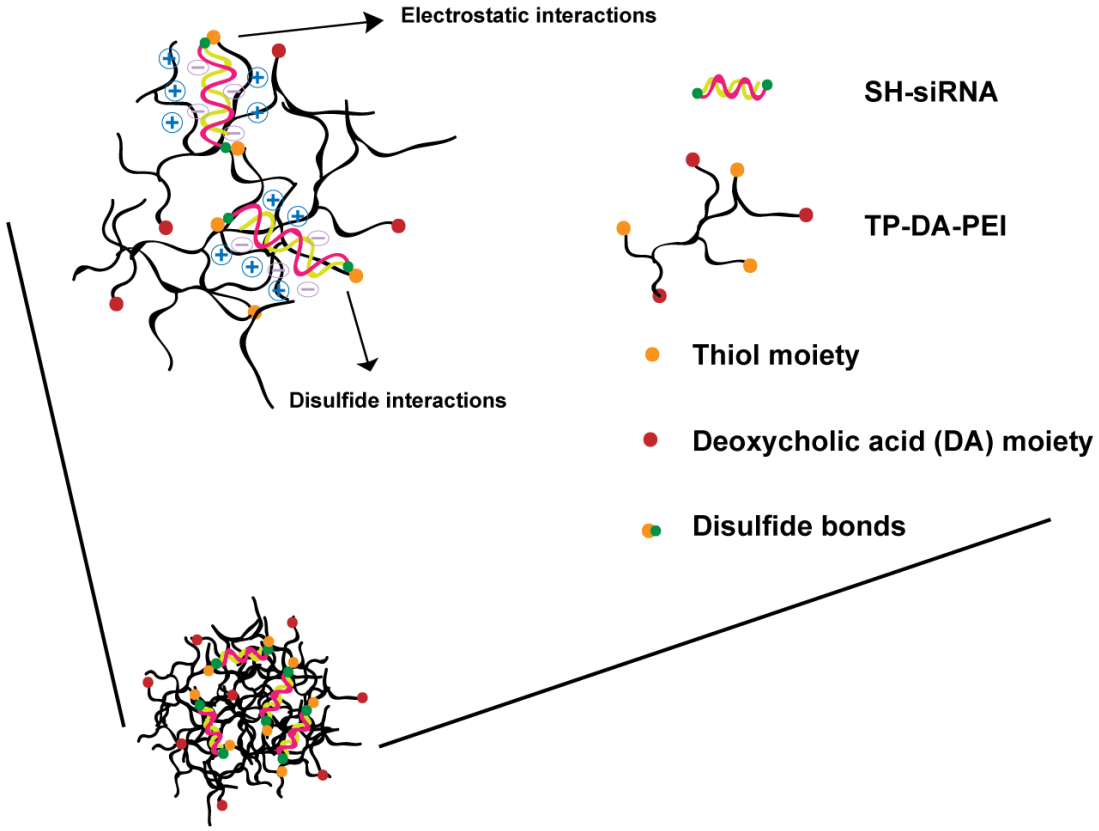

Figure 1.9: Cross-linked polyplexes for efficient siRNA transfection. **TP-DA-PEI** copolymer was cross-linked with a thiol-modified siRNA to form more compact and stable polyplexes.[80]

Another example of polymeric nanoparticles presenting multiple function was demonstrated by Pittella, *et al*. (Figure 1.10).[81] The group developed a hybrid nanocarrier composed of a charge conversional copolymer (**PEG-*b*-CPP**) and calcium phosphate (**CaP**). The **CaP** forms a stable core incorporating the polyanions siRNA and **PEG-*b*-CPP**. The conversional charge copolymer induces the proton-sponge effect and consequently, endosomal escape on account of the polycation formed in acidic pH. The hybrid nanocarrier presented as spherical nanoparticles of ~ 40 nm size. Moreover, the group showed the successfully delivery of siRNA targeting the VEGF gene in pancreatic cell lines, resulting in ~ 80 % of VEGF gene knockdown.

Polymeric nanoparticles have been widely studied for nucleic acid delivery and show a great potential as siRNA delivery platforms. Furthermore, polymers can be combined with inorganic nanoparticles to form hybrid systems. In an example, through electrostatic interactions or through covalent binding, cationic copolymers can be assembled onto gold nanoparticles to form multicomponent delivery platforms.

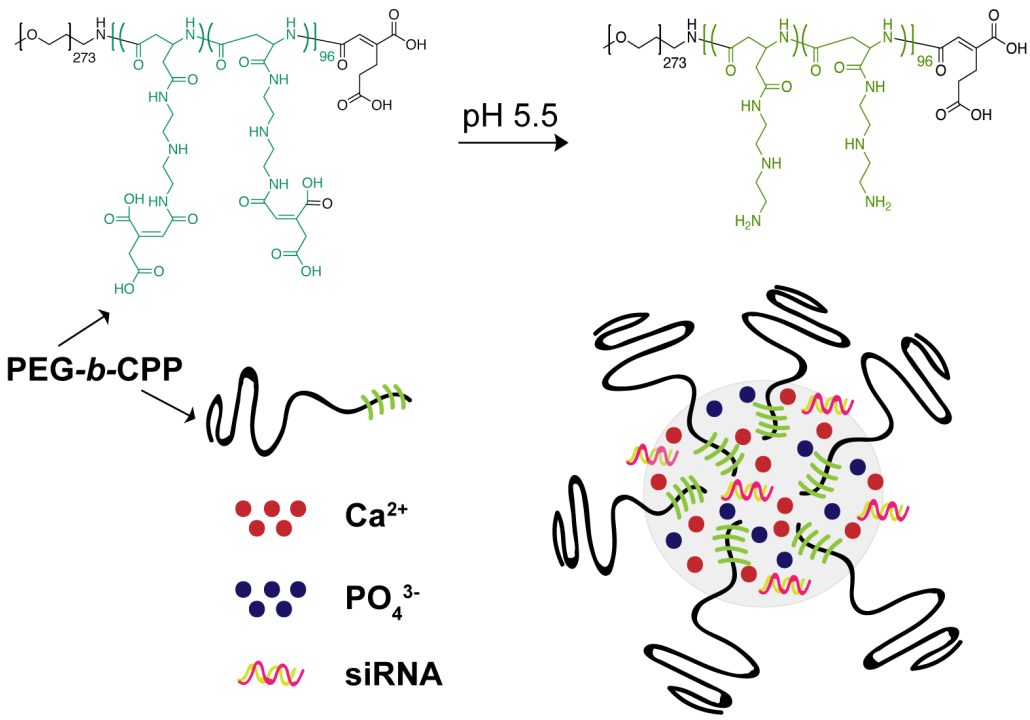

Figure 1.10: Hybrid nanoparticles featuring a charge conversional polymer (**PEG-*b*-CPP**) and calcium phosphate (**CaP**) for the delivery of siRNA.[81]

1.4.3 Gold nanoparticles

Gold nanoparticles (AuNPs) have been widely employed for biomedical applications on account of their unique properties and multiple surface functionalities.[82] AuNPs can be easily synthesised in a wide range of size and shapes and their surface can be easily functionalised with biomolecules through sulfur-gold chemistry. Moreover, AuNPs presents different physicochemical properties associated to their size and shape.[83] The Surface Plasmon Resonance (SPR) phenomenon is one of the most important physicochemical properties of AuNPs.[84] When a metal particle is exposed to light, the oscillating electromagnetic field of the light induces a collective coherent oscillation of the free electrons on the metal surface (Figure 1.11).[85] The amplitude of the electron's oscillation reaches a maximum at a specific frequency, and therefore, the optical properties (absorption and scattering of light) of AuNPs can be monitored by UV-Vis spectroscopy. The SPR can be modulated by changing the size, morphology, surface charge and ligands on the surface of the AuNPs.[86] The versatility of AuNPs provides a range of materials for biomedical applications such as biosensing,[87,88] bioimaging[89–91] and therapeutics.[92,93]

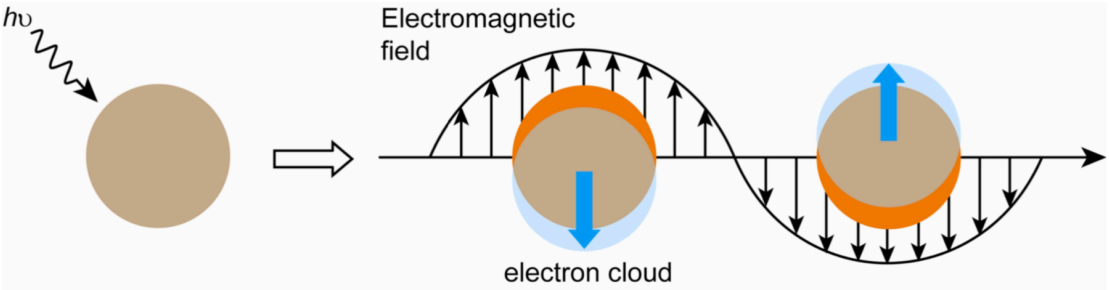

Figure 1.11: Surface Plasmon Resonance (SPR) phenomenon. Schematic representation of the oscillation of the free electrons on the AuNP surface on account of the electromagnetic field of the incident light.[85]

Mirkin, *et al.*[94] was one of the pioneers in conjugating nucleic acids onto AuNPs. Since then, the group have developed AuNPs coated with nucleic acids mainly focusing on biosensing applications[95] and gene regulation.[93] The group functionalised 13 nm AuNPs with a thiol-modified ethylene glycol (**SH-EG**) and a thiol-modified siRNA (Figure 1.12).[93] The siRNA sequence included the **SH-EG** on the 3' end of the sense strand. Conjugation onto the AuNP surface occurred though sulfur-gold chemistry, resulting in ~ 30 siRNA duplexes per AuNP. The particles successfully promoted the gene silencing of the luciferase protein *in vitro*, showing the promising use of this particle for gene knockdown.

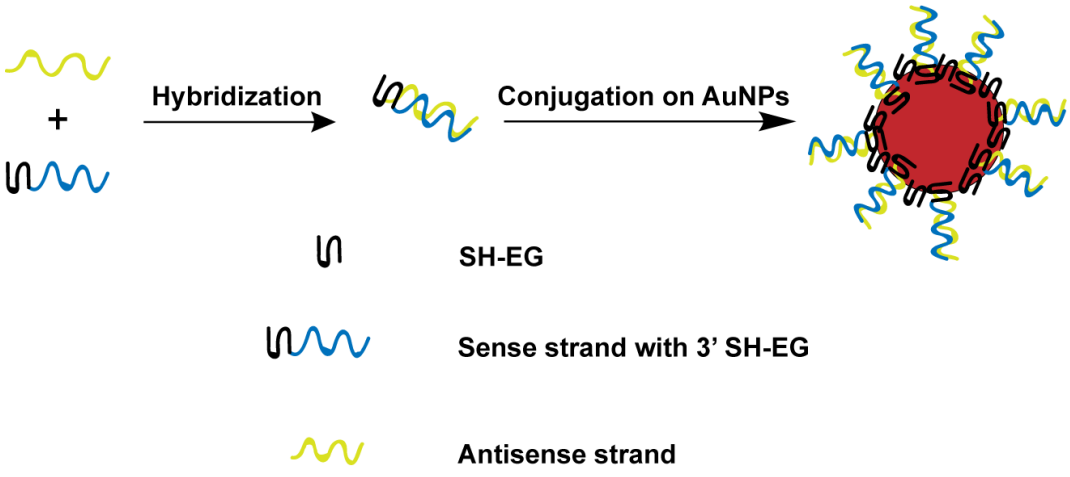

Figure 1.12: Conjugation of thiol-modified siRNA onto AuNPs surface through the sulfur-gold chemistry.[93]

Yi and co-workers[96] developed a multifunctional delivery platform based on functionalised 20 nm AuNPs (Figure 1.13). The group synthesised a diblock copolymer modified with a lipoic acid at the ω-end. The lipoic acid facilitated the conjugation onto AuNPs via the sulfur-gold bond. Moreover, they also modified the PEG terminus at the block copolymer by adding the cyclic Arg-Gly-Asp (cRGD) peptide to construct the

target moiety of the delivery platform. cRGD specifically binds to $\alpha_v\beta_3/\alpha_v\beta_5$ integrins which are overexpressed in a range of tumour cells, therefore facilitating the active accumulation of the nanocarriers. The resulting polymer (**cRGD-PEG-PLL-LA**) was first complexed with siRNA (**uPIC**) thorough ionic interactions between the cationic block **PLL** and the siRNA sequences. AuNPs were then functionalised with **uPICs** to obtain the multifunctional nanocarrier **cRGD-uPIC-AuNP**. The group confirmed the efficacy of the targeting moiety cRGD by *in vivo* tumour accumulation in a subcutaneous HeLa model. After systemic administration, the **cRGD-uPIC-AuNP** enhanced gene silencing efficacy in the subcutaneous tumour when compared with a non-target control nanocarrier. Moreover, systemic administration of nanocarriers loaded with siRNA targeting the papilloma virus-derived E6 oncogene significantly inhibited the growth of subcutaneous HeLa tumours.

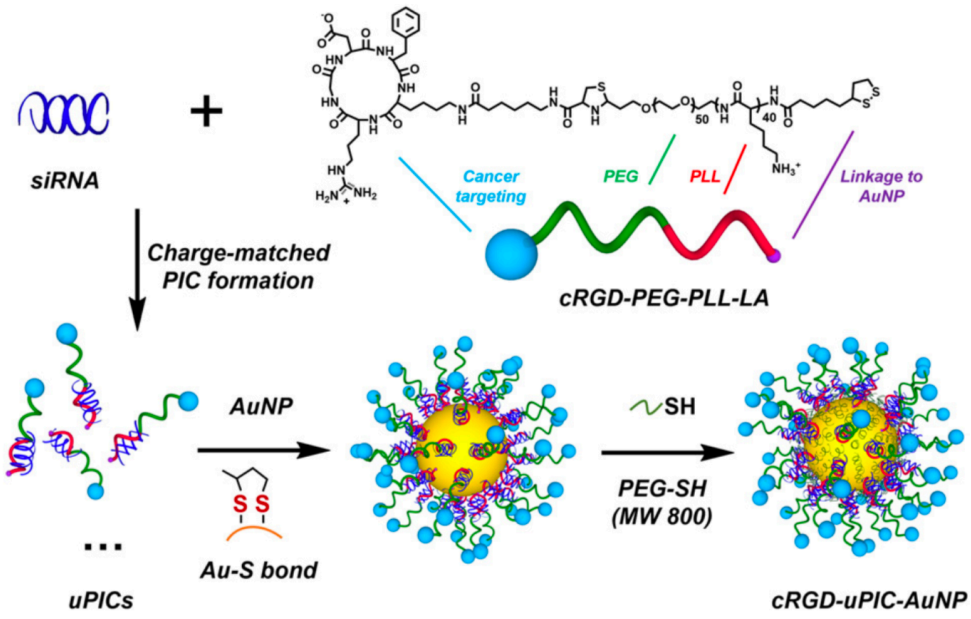

Figure 1.13: Schematic illustration of **cRGD-uPIC-AuNP**. First, uPIC was formed by the complexation of **cRGD-PEG-PLL-LA** with siRNA. cRGD was used as a targeting moiety for cancer cell lines. Second, uPICs were conjugated onto AuNPs through the double Au-S bonds from the lipoic acid moieties. Additional thiolated PEG (PEG-SH) was conjugated onto AuNPs to constructed **cRGD-uPIC-AuNP** particle of 40 nm size.[96]

These examples highlight the versatility of AuNPs in biomedical applications. By combining AuNPs with diblock copolymers it is possible to create a multifunctional delivery platform able to perform according to each stage of the siRNA delivery in clinical use. The development of a delivery platform that features physicochemical stability, prolonged blood circulation and is able to release siRNA according to the acidic stimulus of the endosome enhances the application of siRNA into therapeutics.

1.5 Current status in clinical trials of siRNA therapies

Since the discovery of RNAi therapy and its utilisation on silencing genes that encode proteins that are hard to target with conventional drugs, remarkable progress has been achieved in the development of siRNA therapeutics. The first clinical trial (clinical trial registration number NCT00689065, CALAA-01) was published in 2010 by Davis, *et al.*[97] The group showed the first systemic delivery of synthetic siRNA for the treatment of solid tumours. They reported the reduction of mRNA levels of the subunit M2 of the ribonucleotide reductase (RRM2) followed by a reduction in the expression of the RRM2 protein after systemic administration of nanoparticles containing RRM2 siRNA. The nanoparticles were composed of a cyclodextrin-based polymer and a PEG polymer decorated with a transferrin protein (TF) ligand. The TF ligand facilitates the binding to TF receptors that are upregulated in malignant cells. The clinical trial was terminated in 2013 due to nonspecific toxicity and a low rate of efficacy.

In 2012, Alnylam Pharmaceuticals started the Phase I clinical trial for the drug Patisiran (ALN-TTR02) for the treatment of hereditary transthyretin amyloidosis (hATTR) with polyneuropathy[98] (clinical trial registration number NCT01559077). Almost six years later, the US Food and Drug Administration (FDA) approved patisiran as the first RNAi drug for the treatment of hATTR, named Onpattro by Alnylam Pharmaceuticals (clinical trial phase II registrations numbers NCT01961921, NCT016117067[99] and phase III registration number NCT01960348[100,101]). hATTR is an autosomal dominant, progressive and life-threatening neurodegenerative disease caused by a mutation in the gene encoding the transthyretin protein (TTR), which is mainly produced in the liver. This mutation results in the misfolding of the TTR protein and formation of amyloid fibrils that accumulate in the heart, nerves and other organs, causing polyneuropathy and cardiomyopathy.[102] Patients affected by this disease suffer progressive impaired ambulation and other debilitating symptoms, with a median survival after diagnosis of 5 to 15 years.[103] Patisiran is a lipid nanoparticle (**LNP**) carrying siRNA for silencing of both wild-type and mutant TTR proteins. The drug is a target for the liver and by targeting the TTR mRNA reduces the TTR protein serum levels, improving the patient's symptoms and treatment. The **LNP** (Figure 1.14) comprises of **cholesterol**, a polar lipid (**DSPC**), a pegylated lipid (**PEG2000-C-DMG**) and an ionizable amino lipid (**Dlin-MC3-DMA**). The ionizable lipid is neutral at pH 7.0 but becomes protonated under acidic pH (pH < 6.5), and therefore, is an advantageous feature for endosomal escape. The particles are formed in acidic pH by self-assembly

of the components with siRNA. Because of the ionizable nature of **DLin-MC3-DMA**, the protonation in acidic pH promotes electrostatic interactions with the negative charges of the siRNA and, therefore, successful siRNA loading. Once the nanoparticles are assembled, the hydrophilic outer layer of PEG promotes colloidal stability during storage.[104] After cellular uptake and once internalised in the endosome compartment, the acidic pH protonates the ionizable lipid **DLin-MC3-DMA** promoting disassembly of the particles. The positive charges increase the influx of protons together with the interaction of the lipids to the endosome membrane, contributing to the membrane rupture and release of siRNA into the cytosol.[105]

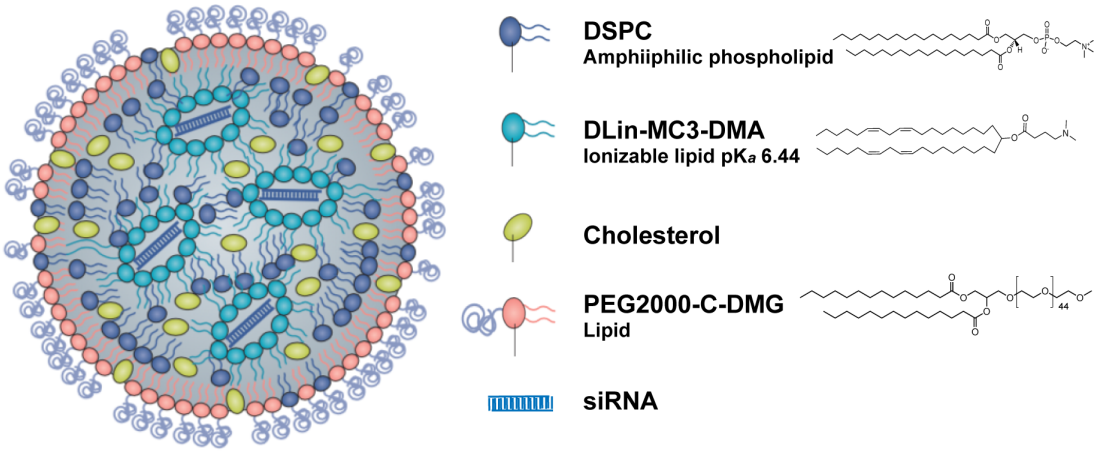

Figure 1.14: First RNAi drug approved by the FDA for treatment of hATTR. Patisiran (Onpattro, Alnylam Pharmaceuticals) is composed of lipid nanoparticle (**LNP**) carrying siRNA targeting the 3' untranslated region of the mutant and wild-type TTR mRNAs. **LNP** schematic representation adapted from Setten, *et al*.[103]

Much effort has been made to translate RNAi biology into RNAi therapeutics. According to the US National Library of Medicine (NIH clinical trials), the number of clinical trials in RNAi therapy has significantly increased in the past years.[67,103] Alnylam Pharmaceuticals holds the majority of clinical trials involving the delivery of siRNA that are in latter stages (Phase II and III) (Table 1.3). At the moment, only one clinical trial is active for the treatment of haematological malignancies by siRNA silencing (NCT02528682) (Table 1.3). The clinical trial consists of lipid nanoparticles for systemic administration of siRNA. The siRNA targets the PD-L1/PD-L2 ligand that is involved in the reduction of the graft-versus-tumour response after allogenic stem cell transplantation. The trial is still at an early stage (Phase I and II) and no studies have been published so far.[106]

Table 1.3: Selected siRNA therapies currently in clinical trials.

Sponsor	Formulation	Disease	Target	Administration route	Clinical Trial Phase NTC number
Alnylam Pharmaceuticals	RSC-GalNAc-siRNA	Primary Hyperoxaluria type I	Glycolate oxidase	Subcutaneous	**Phase II** NCT03350451 NCT03681184 **Phase III** NCT03905694
Alnylam Pharmaceuticals	RSC-GalNAc-siRNA	Haemophilia A/B	Antithrombin	Subcutaneous	**Phase II** NCT03974113 **Phase III** NCT03549871 NCT03754790 NCT03417245 NCT03549871
Alnylam Pharmaceuticals	RSC-GalNAc-siRNA	Hypercholesterolaemia, atherosclerotic cardiovascular disease, renal impairment	PCSK 9	Subcutaneous	**Phase II** NCT03060577 **Phase III** NCT03705234 NCT03705234 NCT03399370 NCT03397121 NCT03705234
Alnylam Pharmaceuticals	RSC-GalNAc-siRNA	Chronic B Hepatitis	All mRNA HBV	Subcutaneous	**Phase I/II** NCT03672188
Alnylam Pharmaceuticals	RSC-GalNAc-siRNA	Acute Intermitent Porphyria	ALAS1	Subcutaneous	**Phase I/II** NCT02949830
Alnylam Pharmaceuticals	RSC-GalNAc-siRNA	Hypertension	Angiotensinogen (AGT)	Subcutaneous	**Phase I** NCT03934307
M. D. Anderson Cancer Center	DOPC encapsulated siRNA (liposome) 1,2-dioleoyl-sn-glycero-3-phosphatidylcholine lipid	Advanced solid Tumours	EphA2	Intravenous	**Phase I** NCT01591356
Silenseed Ltd.	Polymer matrix siRNA	Pancreatic Ductal Adeno carcinoma	Mutant KRAS	Intratumoral	**Phase II** NCT01676259
M. D. Anderson Cancer Center	Exosomes	Metastatic Pancreatic Adenocarcinoma	KRAS G12	Intravenous	**Phase I** NCT03608631
Radboud University	Lipid Nanoparticles	Hematological Malignancies	PD-1		**Phase I/II** NCT02528682

The FDA approval of Patisiran marks a new era for RNAi therapy. Over the next five years, it is expected that many new breakthrough treatments will be published or will be in latter stages for clinical approval. Despite the current success, siRNA therapeutics targeting non-liver tissues still need further development. In this regard, this study proposes a novel nanocarrier for siRNA delivery targeting the RUNX1/ETO fusion protein. The delivery platform was designed to present multifunctional properties to enhance siRNA silencing efficacy. Two nanocarriers are developed in this study based on the combination of gold nanoparticles and polymers. The nanoparticles were designed to present redox and pH stimuli-responses for siRNA release. The experimental research includes the design, chemical synthesis of the polymers, preparation and characterisation of particles and evaluation of siRNA loading efficiency.

1.6 Aims of the project

The main goal of the project was the development of a new delivery platform for the safe and successful delivery of siRNA into AML cells. The detailed goals are as follow:

1) Conjugation of phosphorothioate-modified siRNA and polymer onto AuNPs to obtain a redox-responsive delivery platform;
2) Synthesis of model hydrazones and imines for evaluation of the pH-sensitivity of the C=N bonds;
3) Synthesis of diblock copolymers featuring hydrazone/imine moieties to obtain pH-responsive copolymers;
4) Functionalisation of AuNPs with pH-responsive copolymers and complexation with siRNA to obtain a novel pH-responsive delivery platform.

1.7 References

1 C. S. Grove and G. S. Vassiliou, *Dis. Model. Mech.*, 2014, **7**, 941–951.

2 L. F. Peterson, A. Boyapati, E. Y. Ahn, J. R. Biggs, J. O. Akiko, M. C. Lo, M. Yan and D. E. Zhang, *Blood*, 2007, **110**, 799–805.

3 N. Martinez Soria, R. Tussiwand, P. Ziegler, M. G. Manz and O. Heidenreich, *Leuk. Off. J. Leuk. Soc. Am. Leuk. Res. Fund, U.K*, 2009, **23**, 188–190.

4 O. Heidenreich, J. Krauter, H. Riehle, P. Hadwiger, M. John, G. Heil, H. P. Vornlocher and A. Nordheim, *Blood*, 2003, **101**, 3157–3163.

5 U. Creutzig, M. M. van den Heuvel-Eibrink, B. Gibson, M. N. Dworzak, S. Adachi, E. de Bont, J. Harbott, H. Hasle, D. Johnston, A. Kinoshita, T. Lehrnbecher, G. Leverger, E. Mejstrikova, S. Meshinchi, A. Pession, S. C. Raimondi, L. Sung, J. Stary, C. M. Zwaan, G. J. L. Kaspers and D. Reinhardt, *Blood*, 2012, **120**, 3187–3205.

6 F. Pittella, H. Cabral, Y. Maeda, P. Mi, S. Watanabe, H. Takemoto, H. J. Kim, N. Nishiyama, K. Miyata and K. Kataoka, *J. Control. Release*, 2014, **178**, 18–24.

7 M. Dalmina, F. Pittella, J. A. Sierra, G. R. R. Souza, A. H. Silva, A. A. Pasa and T. B. Creczynski-Pasa, *Mater. Sci. Eng. C*, 2019, **99**, 1182–1190.

8 V. Hoffbrand and P. Moss, *Essential Haematology*, Wiley-Blackwell, Sussex, 6th edn., 2011.

9 S. Haas, A. Trumpp and M. D. Milsom, *Cell Stem Cell*, 2018, **22**, 627–638.

10 K. J. Hope, L. Jin and J. E. Dick, *Nat. Immunol.*, 2004, **5**, 738–743.

11 A. Redaelli, J. M. Stephens, B. L. Laskin, C. L. Pashos and M. F. Botteman, *Expert Rev. Anticancer Ther.*, 2003, **3**, 311–329.

12 I. De Kouchkovsky and M. Abdul-Hay, *Blood Cancer J.*, 2016, 6, 441.

13 A. Kreso and J. E. Dick, *Cell Stem Cell*, 2014, **14**, 275–291.

14 Cancer Research UK, Acute myeloid leukaemia (AML) | Cancer Research UK, https://www.cancerresearchuk.org/health-professional/cancer-statistics/statistics-by-cancer-type/leukaemia-aml#heading-Zero, (accessed 21 July 2019).

15 G. M. Dores, S. S. Devesa, R. E. Curtis, M. S. Linet and L. M. Morton, *Blood*, 2012, **119**, 34–43.

16 J. M. Bennett, D. Catovsky, M. -T Daniel, G. Flandrin, D. A. G. Galton, H. R. Gralnick and C. Sultan, *Br. J. Haematol.*, 1976, **33**, 451–458.

17 D. A. Arber, A. Orazi, R. Hasserjian, J. Thiele, M. J. Borowitz, M. M. Le Beau, C. D. Bloomfield, M. Cazzola and J. W. Vardiman, *Blood*, 2016, **127**, 2391–2405.

18 X. Yang and J. Wang, *J. Hematol. Oncol.*, 2018, **11**, 3.

19 H. Döhner, E. H. Estey, S. Amadori, F. R. Appelbaum, T. Büchner, A. K. Burnett, H. Dombret, P. Fenaux, D. Grimwade, R. A. Larson, F. Lo-Coco, T. Naoe, D. Niederwieser, G. J. Ossenkoppele, M. A. Sanz, J. Sierra, M. S. Tallman, B. Löwenberg and C. D. Bloomfield, *Blood*, 2010, **115**, 453 LP – 474.

20 H. Dombret and C. Gardin, *Blood*, 2015, **127**, 1–10.

21 F. Thol, R. F. Schlenk, M. Heuser and A. Ganser, *Blood*, 2015, **126**, 319–327.

22 J. Meyers, Y. Yu, J. A. Kaye and K. L. Davis, *Appl. Health Econ. Health Policy*, 2013, **11**, 275–286.

23 E. H. Estey, *Am. J. Hematol.*, 2018, **93**, 1267–1291.

24 J. D. Rowley, *Ann. Genet.*, 1973, **16**, 109–12.

25 F. Mitelman, B. Johansson and F. Mertens, *Nat. Rev. Cancer*, 2007, **7**, 233–245.

26 H. Reikvam, K. J. Hatfield, A. O. Kittang, R. Hovland and O. Bruserud, *J. Biomed. Biotechnol.*, 2011, **2011**, 1–23.

27 R. Sood, Y. Kamikubo and P. Liu, *Blood*, 2017, **129**, 2070–2082.

28 M. Ichikawa, A. Yoshimi, M. Nakagawa, N. Nishimoto, N. Watanabe-Okochi and M. Kurokawa, *Int. J. Hematol.*, 2013, **97**, 726–734.

29 K. Lam and D.-E. Zhang, *Front. Biosci.*, 2012, **17**, 1120.

30 J. Wildonger, *Development*, 2005, **132**, 2263–2272.

31 A. Ptasinska, S. A. Assi, D. Mannari, S. R. James, D. Williamson, J. Dunne, M. Hoogenkamp, M. Wu, M. Care, H. McNeill, P. Cauchy, M. Cullen, R. M. Tooze, D. G. Tenen, B. D. Young, P. N. Cockerill, D. R. Westhead, O. Heidenreich and C. Bonifer, *Depletion of RUNX1/ETO in t(8;21) AML cells leads to genome-wide changes in chromatin structure and transcription factor binding*, Nature Publishing Group, 2012, vol. 26.

32 C. Wichmann, I. Quagliano-Lo Coco, Yildiz, L. Chen-Wichmann, H. Weber, T. Syzonenko, C. Döring, C. Brendel, K. Ponnusamy, A. Kinner, C. Brandts, R. Henschler and M. Grez, *Leukemia*, 2015, **29**, 279–289.

33 N. Martinez-Soria, L. McKenzie, J. Draper, A. Ptasinska, H. Issa, S. Potluri, H. J. Blair, A. Pickin, A. Isa, P. S. Chin, R. Tirtakusuma, D. Coleman, S. Nakjang, S. Assi, V. Forster, M. Reza, E. Law, P. Berry, D. Mueller, A. Elder, S. N. Bomken, D. Pal, J. M. Allan, G. J. Veal, P. N. Cockerill, C. Wichmann, J. Vormoor, G. Lacaud, C. Bonifer and O. Heidenreich, *Cancer Cell*, 2018, **34**, 626-642.e8.

34 N. Martinez, B. Drescher, H. Riehle, C. Cullmann, H.-P. Vornlocher, A. Ganser,

G. Heil, A. Nordheim, J. Krauter and O. Heidenreich, *BMC Cancer*, 2004, **4**, 44.

35 G. J. Hannon, *Nature*, 2002, **418**, 244–251.

36 A. Fire, A. Fire, S. Xu, S. Xu, M. K. Montgomery, M. K. Montgomery, S. A. Kostas, S. A. Kostas, S. E. Driver, S. E. Driver, C. C. Mello and C. C. Mello, *Nature*, 1998, **391**, 806–811.

37 M. H. Scott, B. Emily, B. David and J. H. Gregory, *Nature*, 2000, **404**, 293.

38 A. de Fougerolles, H. P. Vornlocher, J. Maraganore and J. Lieberman, *Nat. Rev. Drug Discov.*, 2007, **6**, 443–453.

39 C. Matranga, Y. Tomari, C. Shin, D. P. Bartel and P. D. Zamore, *Cell*, 2005, **123**, 607–620.

40 S. L. Ameres, J. Martinez and R. Schroeder, *Cell*, 2007, **130**, 101–112.

41 G. Hutvágner and P. D. Zamore, *Science*, 2002, **297**, 2056–2060.

42 G. Meister and T. Tuschl, *Nature*, 2004, **431**, 343–349.

43 Y. Lee, M. Kim, J. Han, K. H. Yeom, S. Lee, S. H. Baek and V. N. Kim, *EMBO J.*, 2004, **23**, 4051–4060.

44 S. M. Elbashir, J. Harborth and W. Lendeckel, *Nature*, 2001, **411**, 1–5.

45 J. Guo, L. Bourre, D. M. Soden, G. C. O'Sullivan and C. O'Driscoll, *Biotechnol. Adv.*, 2011, **29**, 402–417.

46 D. Grimm, K. L. Streetz, C. L. Jopling, T. A. Storm, K. Pandey, C. R. Davis, P. Marion, F. Salazar and M. A. Kay, *Nature*, 2006, **441**, 537–41.

47 A. P. McCaffrey, L. Meuse, T.-T. T. Pham, D. S. Conklin, G. J. Hannon and M. A. Kay, *Nature*, 2002, **418**, 38–39.

48 J. Zhang, X. Li and L. Huang, *J. Control. Release*, 2014, **190**, 440–50.

49 K. A. Whitehead, R. Langer and D. G. Anderson, *Nat. Rev. Drug Discov.*, 2009, **8**, 129–138.

50 D. W. Bartlett and M. E. Davis, *Nucleic Acids Res.*, 2006, **34**, 322–333.

51 H. H. Gustafson, D. Holt-Casper, D. W. Grainger and H. Ghandehari, *Nano Today*, 2015, **10**, 487–510.

52 Y. Matsumura and H. Maeda, *Cancer Res.*, 1986, **46**, 6387–92.

53 J. Valencia-Serna, H. M. Aliabadi, A. Manfrin, M. Mohseni, X. Jiang and H. Uludag, *Eur. J. Pharm. Biopharm.*, 2018, **130**, 66–70.

54 D. W. Pack, A. S. Hoffman, S. Pun and P. S. Stayton, *Nat. Rev. Drug Discov.*, 2005, **4**, 581–593.

55 C. Monfardini and F. M. Veronese, *Bioconjug. Chem.*, 1998, 9, 418–450.

56 L. Huang and S. Guo, *J. Nanomater.*, , DOI:10.1155/2011/742895.

57 S. Santos, *J. Mol. Pharm. Org. Process Res.*, 2015, **03**, 1–2.

58 J. Suh, K.-L. Choy, S. K. Lai, J. S. Suk, B. C. Tang, S. Prabhu and J. Hanes, *Int. J. Nanomedicine*, 2007, **2**, 735–41.

59 H. J. Kim, A. Kim, K. Miyata and K. Kataoka, *Adv. Drug Deliv. Rev.*, 2016, **104**, 61–77.

60 M. Dominska and D. M. Dykxhoorn, *J. Cell Sci.*, 2010, **123**, 1183–1189.

61 N. D. Sonawane, F. C. Szoka and A. S. Verkman, *J. Biol. Chem.*, 2003, **278**, 44826–44831.

62 C. E. Thomas, A. Ehrhardt and M. A. Kay, *Nat. Rev. Genet.*, 2003, **4**, 346–358.

63 A. R. Marquez, C. O. Madu and Y. Lu, *Oncomedicine*, 2018, **3**, 48–58.

64 R. Tomanin and M. Scarpa, *Curr. Gene Ther.*, 2012, **4**, 357–372.

65 V. P. Torchilin, *Nat. Rev. Drug Discov.*, 2005, **4**, 145–160.

66 M. L. Briuglia, C. Rotella, A. McFarlane and D. A. Lamprou, *Drug Deliv. Transl. Res.*, 2015, **5**, 231–242.

67 I. V Chernikov, V. V Vlassov and E. L. Chernolovskaya, *Front. Pharmacol.*, 2019, **10**, 444.

68 A. Alshehri, A. Grabowska and S. Stolnik, *Sci. Rep.*, 2018, **8**, 3748.

69 M. J. Wagner, R. Mitra, M. J. McArthur, W. Baze, K. Barnhart, S. Y. Wu, C. Rodriguez-Aguayo, X. Zhang, R. L. Coleman, G. Lopez-Berestein and A. K. Sood, *Mol. Cancer Ther.*, 2017, **16**, 1114–1123.

70 Z. Lin, M. Bao, Z. Yu, L. Xue, C. Ju and C. Zhang, *Biomater. Sci.*, 2019, **7**, 2777–2792.

71 J. Lee and H. J. Ahn, *Biochem. Biophys. Res. Commun.*, 2018, **503**, 1716–1722.

72 U. Kedar, P. Phutane, S. Shidhaye and V. Kadam, *Nanomedicine Nanotechnology, Biol. Med.*, 2010, **6**, 714–729.

73 M. Yokoyama, G. S. Kwon, T. Okano, Y. Sakurai, T. Seto and K. Kataoka, *Bioconjugate Chem*, 1992, **3**, 295–301.

74 S. K. Samal, M. Dash, S. Van Vlierberghe, D. L. Kaplan, E. Chiellini, C. Van Blitterswijk, L. Moroni and P. Dubruel, *Chem. Soc. Rev.*, 2012, **41**, 7147–7194.

75 M. Omedes Pujol, D. J. L. Coleman, C. D. Allen, O. Heidenreich and D. A. Fulton, *J. Control. Release*, 2013, **172**, 939–945.

76 D. J. Gary, N. Puri and Y. Y. Won, *J. Control. Release*, 2007, 121, 64–73.

77 W. Zauner, M. Ogris and E. Wagner, *Adv. Drug Deliv. Rev.*, 1998, **30**, 97–113.

78 M. A. Mintzer and E. E. Simanek, *Chem. Rev.*, 2009, **109**, 259–302.

79 R. V Benjaminsen, M. A. Mattebjerg, J. R. Henriksen, S. M. Moghimi and T. L.

Andresen, *Mol. Ther.*, 2013, **21**, 149–157.

80 Y. Yin, J. H. J. E. Lee, N. W. Kim, J. H. J. E. Lee, S. Y. Lim, E. S. Kim, J. W. Park, M. S. Lee, J. H. Jeong, E. J. Lee, W. N. Kim, H. J. Lee, Y. S. Lim, S. E. Kim, W. J. Park, S. M. Lee and H. J. Jeong, *Polymers (Basel).*, , DOI:10.3390/polym10090953.

81 F. Pittella, M. Zhang, Y. Lee, H. J. Kim, T. Tockary, K. Osada, T. Ishii, K. Miyata, N. Nishiyama and K. Kataoka, *Biomaterials*, 2011, **32**, 3106–3114.

82 M. Sengani, A. M. Grumezescu and V. D. Rajeswari, *OpenNano*, 2017, **2**, 37–46.

83 Y. C. Yeh, B. Creran and V. M. Rotello, *Nanoscale*, 2012, **4**, 1871–1880.

84 X. Huang and M. A. El-Sayed, *J. Adv. Res.*, 2010, **1**, 13–28.

85 V. Amendola, R. Pilot, M. Frasconi, O. M. Maragò and M. A. Iatì, *J. Phys. Condens. Matter*, , DOI:10.1088/1361-648X/aa60f3.

86 S. Srivastava, B. L. Frankamp and V. M. Rotello, *Chem. Mater.*, 2005, **17**, 487–490.

87 C. S. Thaxton, R. Elghanian, A. D. Thomas, S. I. Stoeva, J.-S. Lee, N. D. Smith, A. J. Schaeffer, H. Klocker, W. Horninger, G. Bartsch and C. A. Mirkin, *Proc. Natl. Acad. Sci.*, 2009, **106**, 18437–18442.

88 C. D. Medley, J. E. Smith, Z. Tang, Y. Wu, S. Bamrungsap and W. Tan, *Anal. Chem.*, 2008, **80**, 1067–1072.

89 X. Huang, B. Kang, W. Qian, M. A. Mackey, P. C. Chen, A. K. Oyelere, I. H. El-Sayed and M. A. El-Sayed, *J. Biomed. Opt.*, 2010, **15**, 058002.

90 C. Leduc, J. M. Jung, R. R. Carney, F. Stellacci and B. Lounis, *ACS Nano*, 2011, **5**, 2587–2592.

91 S. Lu, X. Li, J. Zhang, C. Peng, M. Shen and X. Shi, *Adv. Sci.*, 2018, **5**, 1801612.

92 N. L. Rosi, D. A. Giljohann, C. S. Thaxton, A. K. R. Lytton-Jean, M. S. Han and C. A. Mirkin, *Science (80-.).*, 2006, **312**, 1027–1030.

93 D. A. Giljohann, D. S. Seferos, A. E. Prigodich, P. C. Patel and C. A. Mirkin, *J. Am. Chem. Soc.*, 2009, **131**, 2072–2073.

94 C. A. Mirkin, R. L. Letsinger, R. C. Mucic and J. J. Storhoff, *Nature*, 1996, **382**, 607.

95 L. Li, Z. Jin, R. Mirkin C, A. Letsinger R, *Nucleic Acids Res.*, 2002, **30**, 1558–1562.

96 Y. Yi, H. J. Kim, P. Mi, M. Zheng, H. Takemoto, K. Toh, B. S. Kim, K. Hayashi, M. Naito, Y. Matsumoto, K. Miyata and K. Kataoka, *J. Control. Release*, 2016,

244, 247–256.

97 M. E. Davis, J. E. Zuckerman, C. H. J. Choi, D. Seligson, A. Tolcher, C. A. Alabi, Y. Yen, J. D. Heidel and A. Ribas, *Nature*, 2010, **464**, 1067–1070.

98 T. Coelho, D. Adams, A. Silva, P. Lozeron, P. N. Hawkins, T. Mant, J. Perez, J. Chiesa, S. Warrington, E. Tranter, M. Munisamy, R. Falzone, J. Harrop, J. Cehelsky, B. R. Bettencourt, M. Geissler, J. S. Butler, A. Sehgal, R. E. Meyers, Q. Chen, T. Borland, R. M. Hutabarat, V. A. Clausen, R. Alvarez, K. Fitzgerald, C. Gamba-Vitalo, S. V. Nochur, A. K. Vaishnaw, D. W. Y. Sah, J. A. Gollob and O. B. Suhr, *N. Engl. J. Med.*, 2013, **369**, 819–829.

99 O. B. Suhr, T. Coelho, J. Buades, J. Pouget, I. Conceicao, J. Berk, H. Schmidt, M. Waddington-Cruz, J. M. Campistol, B. R. Bettencourt, A. Vaishnaw, J. Gollob and D. Adams, *Orphanet J. Rare Dis.*, 2015, **10**, 109.

100 M. Minamisawa, B. Claggett, D. Adams, A. V. Kristen, G. Merlini, M. S. Slama, A. Dispenzieri, A. M. Shah, R. H. Falk, V. Karsten, M. T. Sweetser, J. Chen, R. Riese, J. Vest and S. D. Solomon, *JAMA Cardiol.*, 2019, **4**, 466–472.

101 S. D. Solomon, D. Adams, A. Kristen, M. Grogan, A. González-Duarte, M. S. Maurer, G. Merlini, T. Damy, M. S. Slama, T. H. Brannagan, A. Dispenzieri, J. L. Berk, A. M. Shah, P. Garg, A. Vaishnaw, V. Karsten, J. Chen, J. Gollob, J. Vest and O. Suhr, *Circulation*, 2019, **139**, 431–443.

102 D. Adams, A. Gonzalez-Duarte, W. D. O'Riordan, C.-C. Yang, M. Ueda, A. V. Kristen, I. Tournev, H. H. Schmidt, T. Coelho, J. L. Berk, K.-P. Lin, G. Vita, S. Attarian, V. Planté-Bordeneuve, M. M. Mezei, J. M. Campistol, J. Buades, T. H. Brannagan, B. J. Kim, J. Oh, Y. Parman, Y. Sekijima, P. N. Hawkins, S. D. Solomon, M. Polydefkis, P. J. Dyck, P. J. Gandhi, S. Goyal, J. Chen, A. L. Strahs, S. V. Nochur, M. T. Sweetser, P. P. Garg, A. K. Vaishnaw, J. A. Gollob and O. B. Suhr, *N. Engl. J. Med.*, 2018, **379**, 11–21.

103 R. L. Setten, J. J. Rossi and S. ping Han, *Nat. Rev. Drug Discov.*, 2019, **18**, 421–446.

104 J. A. Kulkarni, M. M. Darjuan, J. E. Mercer, S. Chen, R. Van Der Meel, J. L. Thewalt, Y. Y. C. Tam and P. R. Cullis, *ACS Nano*, 2018, **12**, 4787–4795.

105 S. M. Hoy, *Drugs*, 2018, **78**, 1625–1631.

106 R. University, Clinical Trial MiHA-loaded PD-L-silenced DC Vaccination After Allogeneic SCT, https://clinicaltrials.gov/ct2/show/NCT02528682?term=NCT02528682&recrs=abdf&rank=1, (accessed 24 July 2019).

Chapter 2
Materials and Methods

2.1 Materials

2.1.1 Instruments and Software

Table 2.1: Instruments and their respective softwares and manufacturers

Instrument	Manufacturer	Software
Allegra X-12R centrifuge	Beckman Coulter	
5415R microfuge	Eppendorf	
RF6000 Spectro		
FLUOstar Omega Microplate Reader	BMG labtech	Omega Software *v3.1* MARS software *v2.1*
GraphPad Prism	GraphPad Software Inc	*v8.00*
GeneAmp PCR System 9700	Applied Biosystems	
Bruker Avance III spectrometer		MestreNova *v12.0.3*
ND-1000 spectrophotometer	Nanodrop Technologies	
QuantStudio Real Time PCR	Applied Biosystems	
Qubit™ 4 Fluorometer	ThermoFisher	
Zetasizer Nano ZS	Malvern Panalytical	Zetasizer Software *v7.03*
Varian ProStar instrument	Varian Inc.	Galaxie Software Cirrus offiline Astra
Viia7 PCR System	Applied Biosystems	QuantStudio Real Time PCR

2.1.2 Chemicals and reagents

Table 2.2: Reagents and their respective suppliers

Reagents	Supplier
(2-Aminoethyl)trimethylammonium chloride hydrochloride 99%	Sigma-Aldrich
(Carboxymethyl)trimethylammonium chloride hydrazide 98%	Sigma-Aldrich
1-(Carboxymethyl)pyridinium chloride hydrazide 99%	Sigma-Aldrich
1,3,5-Trioxane ≥ 99%	Sigma-Aldrich
1,4-Dioxane anhydrous, 99.8%	Sigma-Aldrich
2-Aminoethyl methacrylate hydrochloride 90%	Sigma-Aldrich

Table 2.3: Cont. reagents and their respective suppliers

Reagents	Supplier
2-Fluoro-4-formylbenzoic acid 97%	Apollo Scientific
2-Hydroxyethyl methacrylate 97%	Sigma-Aldrich
2,2′-Azobis(2-methylpropionitrile) 98%	Sigma-Aldrich
3-Morpholinopropylamine 95%	Sigma-Aldrich
4-(2-Aminoethyl)morpholine 99%	Sigma-Aldrich
4-[3-(Dimethylamino)propoxy]benzaldehyde 96%	Sigma-Aldrich
4-Carboxybenzaldehyde 98%	Alfa Aesar
4-Cyano-4-(phenylcarbonothioylthio)pentanoic acid > 97%	Sigma-Aldrich
6X DNA loading buffer	Fermentas
Agmatine sulfate salt ≥ 97%	Sigma-Aldrich
Amberlite IRA-410	Sigma-Aldrich
Chloroform-d 100%, 99.96 atom % D	Sigma-Aldrich
Deuterium oxide, 99.9 atom % D	Sigma-Aldrich
Dimethylformamide distilled grade	Rathburn Chemicals
Ethylenediamine, 99.5%	Sigma-Aldrich
Fetal calf serum	Gibco
GelRed staining (Biotium)	Biotium
Glutathione	Sigma-Aldrich
Gold nanoparticles 20 nm	BBi Solutions
HEPES, 99.5%	Sigma-Aldrich
Iodomethane, > 99%	Sigma-Aldrich
Lithium bromide, > 99%	Sigma-Aldrich
Luciferin	Roche
N,N-Dimethylethylenediamine, 95%	Sigma-Aldrich
Poly(ethylene glycol) methyl ether methacrylate M_n: 300 g mol^{-1}	Sigma-Aldrich
Poly(ethylene glycol) methyl ether methacrylate M_n: 500 g mol^{-1}	Sigma-Aldrich
Poly(methyl methacrylate) standards	Agilent Technologies
Potassium hexafluorphosphate ≥99%	Sigma-Aldrich
RPMI	Sigma-Aldrich

Table 2.4: Cont. reagents and their respective suppliers

Reagents	Supplier
SyBR Green	Life Tech
Tetramethylsilane	Sigma-Aldrich
Thionyl chloride	Sigma-Aldrich
Triethylamine	Sigma-Aldrich
Trimethyl orthoformate	Alfa Aesar
Trypan blue	Sigma-Aldrich

2.1.3 Experimental kits

Table 2.5: Experimental kits and their respective suppliers

Kit	Manufacturer
Qiashredder	Qiagen
Qubit miRNA assay kit	ThermoFisher
Qubit ssDNA assay kit	ThermoFisher
RNeasy Mini Kit	Qiagen
RevertAid^{TM} H Minus cDNA Synthesis Kit	ThermoFisher

2.1.4 Oligonucleotides and short interfering RNAs (siRNAs)

Table 2.6: Sequences of oligonucleotides and siRNAs. * = Phosphorothioate modification.

Oligonucleotides	Manufacturer	Sequence
Primers		
RUNX1/ETO forward	Sigma-Aldrich	5′-AATCACAGTGGATGGGCCC -3′
RUNX1/ETO reverse	Sigma-Aldrich	5′-TGCGTCTTCACATCCACAGG-3′
GPDH forward	Sigma-Aldrich	5′-TGGCATGGCCTTCCGT-3′
GAPDH reverse	Sigma-Aldrich	5′-TCTCCAGGCGGCACGTT-3′
ssODN		
ssODN	Sigma-Aldrich	5′-Cy5-CAGTACGATTTCGAGGTT-3′
PS-ssODN	Sigma-Aldrich	5′-Cy5-CAGTACGATTTCGAGGT*T-3′
siRNAs		
PS-siRE sense	AxoLabs	5′-CUCGAAAUCGUACUGAGAAdT*dT-3′
siRE antisense	AxoLabs	5′-UCUCAGUACGAUUUCGAGGdTdT-3′
PS-siMM sense	AxoLabs	5′-CCUCGAAUUCGUUCUGAGAdT*dT-3′
siMM antisense	AxoLabs	5′-UCUCAGAACGAAUUCGAGGdTdT-3′
3PS-siLUC sense	Sigma-Aldrich	5′-CUUACGCUGAGUACUUCG*A*dT*dT -3′

siLUC antisense	Sigma-Aldrich	5′-UCGAAGUACUCAGCGUAAGdTdT-3′

Short interfering RNAs (siRNAs) were provided as separate sense and antisense strands in lyophilised form. In order to prepare double-stranded siRNA, hybridisation buffer (Hepes buffer 25 mM, NaCl 100 mM, pH 7.4) was added to each strand at a final concentration of 100 μM. An equal molar ratio of each strand was transferred to a RNase-free Eppendorf tube and heated for 5 min at 95 °C. The reaction was allowed to cool to room temperature and siRNAs were stored at -20 °C.

2.2 Tissue culture and cell lines

2.2.1 Cell lines

Table 2.7: Cell lines, tissue culture conditions and their cytogenetics

Cell line	Origin	Tissue Culture	Cytogenetics
Kasumi-1	Relapsed childhood AML	RPMI 1640 supplemented with 10% FCS	t(8;21)(q22;q22) *RUNX1/ETO*
Kasumi-1 pSLIEW	Relapsed childhood AML	RPMI 1640 supplemented with 10% FCS	t(8;21)(q22;q22) *RUNX1/ETO* *Firefly luciferase*

Cells were split every 48-72 h in fresh media to keep cell concentration at 0.5 x 10^6 cells mL^{-1}. The cell lines were cultured in upright culture flasks in an incubator set to 37 °C, 5% CO_2, fully humidified.

2.2.2 Cell counting

All cell lines were counted using Trypan Blue which selectively stains the dead cells a dark blue colour. The negatively charged Trypan Blue molecules pass only through the membrane of damaged dead cells while live viable cells do not absorb the dye. Equal volumes from the cell suspension and the dye were mixed giving a dilution factor of 2 that was loaded into a haemocytometer. The live/dead cells were counted under 10 × microscope magnification and the cell concentration (mL^{-1}) was determined by the following equation:

$$C = n \times D \times f$$

Equation 1

Where, *C* is the cell concentration in mL^{-1}, *n* is the number of live cells, *D* is the dilution factor used and *f* is the chamber depth factor (= 10,000).

2.3 General methods

2.3.1 Nuclear Magnetic Resonance spectroscopy (NMR)

^{1}H NMR Analysis was performed using a Bruker Avance III spectrometer at 300 and 700 MHz. ^{13}C NMR analysis was performed on a Bruker Avance III spectrometer at 75 MHz. Samples were dissolved in deuterated solvent ($CDCl_3$ or D_2O) and the residual solvent signal was used as an internal standard. MestreNova *v12.0.3* was used to process the spectra.

2.3.2 Gel Permeation Chromatography (GPC)

The polymers were analysed by gel permeation chromatography (GPC) using a Varian ProStar instrument (Varian Inc.) equipped with a Varian 325 UV-Vis dual wavelength detector with a 254 nm laser, a Dawn Heleos II multi-angle laser light scattering detector (Wyatt Technology Corp.), a Viscotek 3580 differential refractive index detector and two PL gel 5 μm Mixed D 300 × 7.5 mm columns with a guard column (Polymer Laboratories Inc.) in series. Chromatogram analysis was performed on Galaxie software (Varian Inc.) and analysed with the Cirrus software (Varian Inc.) and Astra software (Wyatt Technology Corp.). Near monodisperse poly(methyl methacrylate) standards (Agilent Technologies) were used for calibration. Samples were prepared at 8 mg/mL and filtered through a 0.22 μm membrane. LiBr (1 g/l) in DMF at 50 °C was used as the mobile phase (flow rate: 0.6mL/min).

2.3.3 Dynamic Light Scattering

For the determination of the size distribution of the nanoparticles, DLS measurements were carried out at 25 ºC using a Zetasizer Nano ZS (Malvern Instruments) at a detection angle of 173º with an incident He-Ne laser beam (633 nm). Data obtained from the rate of decay in the photon correlation function were analysed using the cumulant method to obtain the corresponding hydrodynamic diameters and polydispersity index (PdI) of the nanoparticles. The particles size is calculated from the translational frictional coefficient that is determined by the Stokes-Einsten[1,2] equation as described below:

$$d(H) = kT / 3\pi\eta D$$

Equation 2

Where d(H) is the hydrodynamic diameter, k is the Boltzmann's constant, T is the absolute temperature and η is the viscosity.

2.3.4 Determination of λ_{SPR} in 20 nm gold nanoparticles

On account of the specific optical properties of spherical AuNPs, UV-Vis spectroscopy was used to characterise AuNPs and determine their stability in different media. UV-Vis Spectra were acquired on a FLUOstar Omega Microplate reader (BMG Labtech) between 350-700 nm and a wavelength interval of 2 nm and the absorbances were normalised. The λ_{SPR} was calculated between 470-600 nm according to the equation[3] below:

$$\lambda_{SPR} = \Sigma(Abs_{470\text{-}600} \times \lambda_{470\text{-}600}) / \Sigma Abs_{470\text{-}600}$$

Equation 3

Where Abs is the normalised absorbance values from 470 nm to 600 nm and λ is the wavelength from 470 to 600 nm.[3]

2.3.5 Loading efficiency of the nanocarriers

The loading efficiencies of the nanocarriers were determined by an indirect quantification method and a direct quantification method. The indirect method determines the amount of unloaded cargo, which gives an indirect quantification of the amount of cargo that was therefore loaded onto the nanoparticles. The direct method quantifies the amount of loaded cargo and is determined after cleavage of the cargo from the surface of the particles. For particles prepared with Cy5-labelled PS-ssODN and Cy5-labelled ssODN, the quantification was determined by fluorescence spectroscopy. The quantification of particles prepared with siRNA was determined using the QuBit miRNA assay kit (Thermofisher) following the manufacture's protocol. Briefly, the QuBit working solution is prepared by diluting the QuBit miRNA reagent (fluorescent dye) in the QuBit miRNA buffer at 1:200. The two QuBit miRNA standards and the samples were diluted with the QuBit working solution at 1:20. The fluorescence reading were acquired using the QuBit 3.0 fluorimeter at the blue excitation (420 – 495 nm) and green emission (500 – 550 nm).

2.3.5.1 Indirect Quantification

In a typical example, the amount of unloaded PS-ssODN was determined using the RF6000 spectrofluorometer (Shimadzu). Particles were centrifuged at 15,000 $\times$ g for 10 min. The supernatants were carefully collected and the amount of unloaded ssODN was determined by fluorescence spectroscopy. Fluorescence was recorded at

excitation/emission wavelengths of 650/670 nm. A calibration curve of PS-ssODN in Hepes buffer pH 7.4 was prepared at 0, 0.5, 3.0, 5.0 and 9.0 μM (Appendix A). The fluorescence measurements of the supernatants were interpolated from the calibration curve to determine the amount of unloaded PS-ssODN. The loading efficiency was calculated according to the equation bellow:

$$Loading\ efficiency\ \% = 100\ - \frac{unloaded\ ssODN}{initial\ concentration} \times\ 100$$

Equation 4

2.3.5.2 Direct Quantification

In a typical example, particles were purified by centrifugation 15,000 × g for 10 min and then washed with Hepes buffer pH 7.4 (900 μL) three times. The particles were then treated with dithiothreitol (DDT) 100 mM for 4 h to release the amount of loaded PS-ssODN. The centrifugation procedure was repeated and the supernatants collected for quantification by fluorescence spectroscopy. Fluorescence was recorded at excitation/emission wavelengths of 650/670 nm. The concentration of PS-ssODN in the supernatants was interpolated from calibration curves (Appendix A) to determine the amount of loaded PS-ssODN onto AuNPs. The loading efficiency was calculated according to the equation:

$$Loading\ efficiency\ \% = 100\ \times \frac{loaded\ ssODN}{initial\ concentration}$$

Equation 5

2.4 Experimental Chapter 3

2.4.1 Synthesis of pPEGMA polymers (P1 and P2)

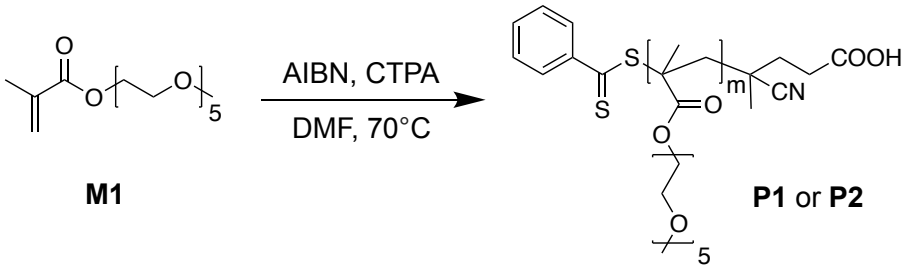

M1 **P1** or **P2**

Scheme 2.1: Synthesis of pPEGMA **P1** and **P2**

RAFT Polymerisation was used to prepare pPEGMA polymers for conjugation onto AuNPs (Scheme 2.1). Poly(ethylene glycol) methyl ether methacrylate monomer **M1** ($PEGMA_{300}$ M_n: 300 g mol^{-1}) was passed through a column of activated basic alumina to remove the inhibitor and stored at -20 °C before use**.** 4-Cyano-4-(thiobenzoylthio)pentanoic acid (CTPA) and 2,2'-azobis(2-methylpropionitrile) (AIBN) was used as chain transfer agent (CTA) and initiator, respectively. In a typical example, $PEGMA_{300}$ (7.00 g, 23.33 mmol, 50.0 eq.) and CTPA (130.2 mg, 0.466 mmol, 1.0 eq.) were added to a Schlenk tube. AIBN (15.3 mg, 0.093 mmol, 0.2 eq.) and 1,3,5-trioxane (50.0 mg, 0.555 mmol, 1.2 eq) were then added followed by DMF (10.5 mL). The reaction mixture was degassed through five freeze-pump-thaw cycles and purged with N_2 and allowed to warm to room temperature. The reaction mixture was then placed in an oil bath at 70 °C. After 2 h, the reaction was quenched by freezing in liquid nitrogen. The reaction mixture was dialysed in distilled water and freeze-dried to obtain **P1** as a pink oil. ^{1}H NMR (300 MHz, $CDCl_3$): δ = 0.64 – 1.14 (br, -$CHCH_3$, polymer backbone), 1.62 – 2.06 (br, -$CHCH_2$, polymer backbone), 3.30 – 3.43 (br, -OCH_3), 3.47 – 3.56 (br, -OCH_2CH_2), 3.57 – 3.77 (br, -OCH_2CH_2, ethylene glycol chain), 3.96 – 4.22 (br, -OCH_2), 7.30 – 7.40 (br, Ar, polymer endgroup), 7.45 – 7.54 (br, Ar, polymer endgroup), 7.81 – 7.89 (br, Ar, polymer endgroup). The composition of **P1** was determined by comparing the integration of the aromatic CTA protons with the integration of the methoxy methyl (-OCH_3) of the monomer side chains. **P2** was synthesised in the same conditions, however the polymerisation time was increased to 5 h to obtain a polymer of larger molecular weight. The same analysis was used to determine the composition of **P2**. ^{1}H NMR (300 MHz, $CDCl_3$): δ = 0.63 – 1.13 (br, $CHCH_3$, polymer backbone), 1.53 – 2.07 (br, $CHCH_2$, polymer backbone), 3.34 – 3.40 (br, -OCH_3), 3.45 – 3.50 (br, -OCH_2CH_2), 3.59 – 3.69 (br, -OCH_2CH_2, ethylene glycol chain), 3.94 – 4.20 (br, -OCH_2), 7.30 – 7.39 (br, Ar, polymer endgroup), 7.46 – 7.54 (br, Ar, polymer endgroup), 7.81 – 7.89 (br, Ar, polymer endgroup).

The monomer conversion was monitored by ^{1}H NMR spectroscopy using the integrals of $PEGMA_{300}$ vinyl group signals at 5.45 ppm and 6.01 ppm. 1,3,5-Trioxane was used as internal standard (5.10 ppm). The table below shows the RAFT polymerisation conditions for **P1** and **P2**.

Table 2.8: RAFT polymerisations of P1 and P2. [a] Determined by 1H NMR spectroscopy.

Polymer	Ratios [M]/[CTA]/[I]	Solvent	Time	Monomer conversion
P1	100/1.0/0.2	DMF	2 h	46%
P2	100/1.0/0.2	DMF	5 h	72%

2.4.2 Conjugation of pPEGMA to gold nanoparticles (AuNPs)

For the conjugation of pPEGMA onto AuNPs, particles (1.16 nM, 100 μL) were incubated overnight with different molar ratios of **P1** or **P2** in a 96 well-plate. After 24h, 10 μL of $NaCl_{(aq)}$ (1 M) was added and the UV-Vis spectrum was acquired using a FLUOstar Omega Microplate Reader between 350-700 nm and a wavelength interval of 2 nm. The induced aggregation factor was determined by calculating the ratio $\lambda_{615}/\lambda_{524}$. High aggregation factor indicates salt-induced aggregation and therefore, by evaluating the induced aggregation factor it is possible to determine the appropriate polymer concentration to successfully coat AuNPs. Uncoated AuNPs were used as a control.

2.4.3 Conjugation of ssODN and siRNA onto AuNPs

In a typical example, AuNPs (11.6 nM, 100 μL) were incubated with 4 μL of PS-ssODN at 100 μM (final concentration 2.2 μM). After 10 min sonication, the suspension was left at room temperature overnight. The polymer was added (10 μL, final conc. 0.7 μM) to the suspension and the particles were sonicated for 10 min. After 6 hours, 60 μL of a solution containing 0.3% $SDS_{(aq)}$ and 0.3 M of $NaCl_{(aq)}$ was added (final concentration 0.1% and 0.1M). After 1 hour, 3.75 μL of $NaCl_{(aq)}$ (1.4 M) was added and the particles were incubated for 1 h. This step was repeated twice until the final concentration of NaCl reached 0.16 M and the suspension was allowed to react overnight. Nanoparticles were purified by centrifugation at 15,000 x g for 10 min and washed 3 times with Hepes buffer (10 mM) pH 7.4. Figure 2.1 and Table 2.9 describe the conjugation procedure. The same procedure was used to conjugate non-modified ssODN (Table 2.10) and PS-siRNA and 3PS-siRNA (Table 2.11). To optimize the loading of siRNA onto AuNPs, the protocol was adjusted by changing the final salt concentration during the salt aging process, the final SDS concentration, the titration time and also the temperature during loading (Table 2.11).

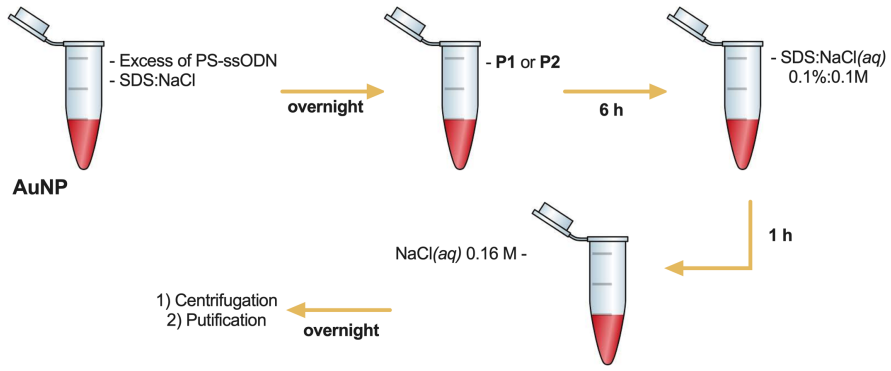

Figure 2.1: Preparation of gold nanoparticles coated with ssODN and polymer.

Table 2.9: Conditions for preparation of AuNPs coated with PS-ssODN.

PSssNPs

Molar ratios AuNP:PS-ssODN:pPEGMA	[$NaCl_{(aq)}$]	[$SDS_{(aq)}$]	NaCl titration time
1:350:110	160 mM	0.1 %	3 h

Table 2.10: Conditions for preparation of AuNPs coated with non-modified ssODN.

ssNPs

Molar ratios AuNP:PS-ssODN:pPEGMA	[$NaCl_{(aq)}$]	[$SDS_{(aq)}$]	NaCl titration time
1:350:110	160 mM	0.1 %	3 h

Table 2.11: Conditions for conjugation of PS-siRNA and 3PS-siRNA onto AuNPs.

PSsiNPs

	Molar ratios AuNP:PS-siRNA:pPEGMA	[$NaCl_{(aq)}$]	[$SDS_{(aq)}$]	NaCl titration time	Heat
PSsiNP.P1	1:350:110	160 mM	0.1%	3 h	-
PSsiNP.P2-T1	1:350:110	160 mM	0.1%	12 h	-
PSsiNP.P2-T2	1:350:870	160 mM	-	-	-
PSsiNP.P2-T3	1:3500:870	-	-	-	-

3PSsiNPs

	Molar ratios AuNP:3PS-siRNA:P2	[$NaCl_{(aq)}$]	[$SDS_{(aq)}$]	NaCl titration time	Heat
3PSsiNP-T1	1:344:110	160 mM	0.1%	3 h	-
3PSsiNP-T2	1:850:110	260 mM	0.1 %	3 h	-
3PSsiNP-T3	1:350	160 mM	0.1 %	3 h	-
3PSsiNP-T4	1:350	-	-	3 h	95 °C, 5 min
3PSsiNP-T5	1:350	160 mM	0.1%	3 h	95 °C, 5 min

2.4.4 Stability of PSssNP.P2

The stability of nanoparticles loaded with PS-ssODN was assessed by incubating 50 μl of **PSssNP.P2** in 50 μl of tissue culture medium RPMI containing 10% FCS. The final concentration of PS-ssODN in the samples was 0.5 μM. At different time points, the particles were isolated by centrifugation and the supernatant collected for quantification by fluorescence. The fluorescence measurements were interpolated from a calibration curve (Appendix A) and the concentration of PS-ssODN released from **PSssNP.P2** determined.

2.4.5 Glutathione mediated release of PSssNP.P2

Samples at time points 0 h and 1 h from the stability assay were collected and GSH was added at a final concentration of 10 mM. After 1 h incubation, the samples were centrifuged at 15,000 × g for 10 min to precipitate the particles. The supernatants were carefully collected for quantification of PS-ssODN by fluorescence spectroscopy. The values were interpolated from a standard curve (Appendix A) and the amount of PS-ssODN released was determined.

2.4.6 In vitro gene silencing

To evaluate the gene silencing efficiency of siRNA contained in PSsiNPs, 0.5 mL of Kasumi-1 cells were seeded at 0.5 x 10^6 cells.mL^{-1} in a 24 well plate. PSsiNPs were added at a final siRNA (siRE and siMM) concentration of 200 nM. After 24 and 48 h, cells were collected and centrifuged at 300 x g for 5 min. The supernatant was discarded and the pellet resuspended in 500 μL of PBS 10 mM before further centrifugation at 300 x G for 5 min after which the supernatant was discarded and the pellet resuspended in RLT buffer (RNeasy kit). Samples were frozen at -20 °C for storage.

2.4.6.1 RNA extraction

Cell samples in RLT buffer were thawed and vortexed. mRNA was extracted using RNeasy Kit according to the manufacture's protocol. Briefly, cell lysates were loaded into a QIAshredder column and centrifuged at 8,000 × g for 2 min. Ethanol (350 μL) was added to each lysate and the sample was loaded into a RNeasy column and centrifuged at 8,000 × g for 30 s. The RNeasy spin column was then washed with 700μL of RW1 buffer and twice with 500 μL of RPE, with centrifugation at 8,000 × g for 30 s between each step. In order to remove the excess of RPE buffer, samples

were centrifuged for a further 2 min at 8,000 × g before 50 µL RNase-free water was added to each column. After 1 min incubation the samples were centrifuged for 1 min at 8,000 × g and the concentration of RNA in the flow through was determined using the Nanodrop 2000. Samples were stored at -20 °C.

2.4.6.2 cDNA synthesis

cDNA was synthesised from the mRNA samples by reverse transcription using Revert Aid H minus 1st strand cDNA Kit (Thermo Fisher). RNA (1,000 ng) was added to 1 µL random hexamers and deionised water to a final total volume of 12 µL. The reaction was incubated at 70 °C for 5 min to disrupt mRNA secondary structures. The mixture was cooled to 4 °C and 8 µL of master mix (Table 2.12) was added to each reaction and the reverse transcription occurred under the following conditions: 25 °C, 10 min; 42 °C, 60 min; 70 °C, 10 min; held at 4 °C. After cDNA synthesis, 30-80 µL of RNA-free water was added to samples and stored at -20 °C.

Table 2.12: cDNA Master Mix formulation

Reagent	Amount
5X Reaction buffer	4
dNTP mix (10mM)	2
Riboblock RNase inhibitor	1
RevertAid H minus reverse transptase	1

2.4.6.3 Real-time quantitative reverse transcriptional PCR (RT-qPCR)

Real-time RT-qPCR was performed on an ABI Prism 7000 sequence detection system using SYBRGreen PCR Master Mix (Table 2.13). GAPDH was used as the house-keeper gene to normalise data before statistical analysis. The master mix (Table 2.13) was prepared according to manufacturer's protocol. In a 384 well plate 8 µL of master mix was added to each well. cDNA from each sample (2 µL) was pipetted into wells in triplicate and a water control was included. The plate was sealed and centrifuged at 1000 × g for 1 min before being loaded into the sequence detection system. The reaction was performed as follows: 50 °C, 2 min; 95 °C, 10 min; 60 °C, 15 seconds; followed by 40 cycles of 95 °C, 15 seconds; 60 °C, 1 min; followed by a single cycle of 95 °C, 15 seconds; 60 °C 15 seconds; 95 °C 15 seconds. Analysis was performed using the QuantStudio Real-Time PCR software and relative RUNX1/ETO expression was calculated according to the formula bellow:

$$-\Delta Ct_{RUNX1/ETOt} = Ct_{RUNX1/ETOt} - Ct_{GAPDH} \quad \textit{Equation6}$$

$$-\Delta\Delta Ct_{RUNX1/ETO} = -\Delta Ct_{RUNX1/ETOt} - \Delta Ct_{RUNX1/ETOc} \quad \textit{Equation 7}$$

$$\text{Rel. RNA expression} = 2^{-(-\Delta\Delta CtRUNX1/ETO)} \quad \textit{Equation 8}$$

Where, Ct is the mean cycle threshold of each replicate.

Table 2.13: RT-qPCR Master Mix

Reagent	Amount
SyBr Green	5 μl
Primer Mix (10 μM)	0.3 μl
RNA-free water	2.7 μl

2.4.7 Luciferase gene knockdown

Luciferase assay was used to fast determine the gene knockdown efficiency of 3PS-siLUC. Kasumi-1 pSLIEW cells (90 μL) were seeded at 0.5 x 10^6 cells mL^{-1} in a 96 well plate. To determine the sequence efficiency to promote gene knockdown, 3PS-siLUC was eletroporated to the cells at 50, 100 and 200 nM. After 24 and 48 h incubation time, luciferin (10 μL at 4.5 $mg.mL^{-1}$ in RPMI) was added to samples. The luminescence of samples was read using the Omega plate reader after 3, 5 and 10 min. Results were averaged to determine the luminescence of each well.

2.5 Experimental Chapter 4

2.5.1 Synthesis of A1

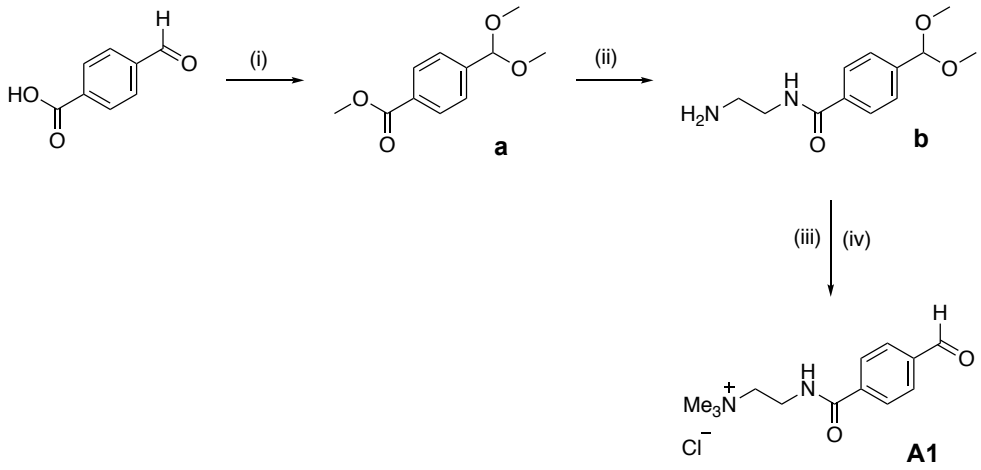

Scheme 2.2: Synthesis of aldehyde **A1**. (i) $CH(OCH_3)_3$ MeOH, H_2SO_4, 24 h. (ii) Ethylenediamine, 130 °C, 18 h. (iii) MeI, K_2CO_3, MeOH, 18 h, 55 °C. (iv) HCl, acetone:H_2O (1:1, v/v), 2 h.

Aldehyde **A1** was prepared in a four-step synthesis(Scheme 2.2). Synthetic intermediates are labelled with lower case letters.

2.5.1.1 Synthesis of methyl-4-(dimethoxymethyl)-benzoate (a)

4-Carboxybenzaldehyde (20.0 g, 0.133 mol) was dissolved in MeOH (120 mL) and acidified with concentrated H_2SO_4 (20 drops). Trimethyl orthoformate (44 mL, 0.400 mol) was added in one portion and the mixture was refluxed for 24 h with stirring. The mixture was transferred to a separating funnel with saturated $NaHCO_3$ (100 mL) and the aqueous layer was extracted with CH_2Cl_2 (3 x 150 mL). The organic extracts were combined and dried over $MgSO_4$, filtered and evaporated to dryness to afford a yellow oil (23.83 g, 0.11 mol, 85 %) which was used without further purification. ^{1}H NMR ($CDCl_3$, 300 MHz): δ = 3.30 (s, 6H), 3.89 (s, 3H), 5.41 (s, 1H), 7.52 (d, 2H, J = 9 Hz) and 8.00 ppm (d, 2H, J = 9 Hz). ^{13}C NMR ($CDCl_3$, 75 MHz) δ = 52.2, 52.7, 102.4, 126.9, 129.6, 130.3, 143.0 and 166.9 ppm.

2.5.1.2 Synthesis of N-(2-aminoethyl)-4-(dimethoxymethyl)benzamide (b)

Purified **a** (16.40 g, 78.0 mmol) was refluxed in ethylenediamine (200 mL) for 18 h. Ethylenediamine was removed under pressure to afford a deep brown solid which was purified by column chromatography (SiO_2, CH_2Cl_2:EtOH:Et_3N, 80:15:5 v/v). The fractions were collected and evaporate to dryness to afford a pale white solid (7.2 g, 30.2 mmol, 44 % yield). ^{1}H NMR ($CDCl_3$, 300 MHz): δ = 2.29 (s, 2H), 2.90 (t, 2H, J = 6.0 Hz), 3.28 (s, 6H), 3.45 (q, 2H, J = 6.0 Hz), 5.37 (s, 1H), 7.22 (br t, 1H), 7.47 (d, 2H, J = 9.0 Hz) and 7.81 ppm (d, 2H, J = 9.0 Hz). ^{13}C NMR ($CDCl_3$, 75 MHz): δ = 42.2, 52.7, 58.0, 102.5, 126.9, 127.1, 134.6, 141.4 and 167.6 ppm.

2.5.1.3 Synthesis of 2-(4-Formylbenzamido)-N,N,N-trimethylethan-1-aminium

N-(2-Aminoethyl)-4-(dimethoxymethyl)benzamide (**b**) (4.0 g, 16.8 mmol) was dissolved in MeOH (100 mL). K_2CO_3 (4.6 g, 33.6 mmol was added followed by addition of iodomethane (48.0 g, 336 mmol) in one portion, and this mixture was stirred for 8 h at 55 °C. Residual iodomethane was removed under reduced pressure and Et_2O (30 mL) was added and the suspension was agitated in a sonic bath for 30 min and filtered to afford a pale brown solid. This solid was dissolved in 1:1 acetone:water (50 mL) and acidified with 2 mL of concentrated HCl. After stirring at room temperature for 2 h the mixture was filtered and the filtrate evaporated to dryness. The resulting pale brown solid was purified by precipitation in a saturated aqueous solution of KPF_6 and isolated

by filtration. The hexafluorophosphate is an anion that exhibits low solubility in water and therefore, can be isolated by filtration. Then, the filtrate was dissolved in MeOH in the presence of trimethylammonium-functionalised Amberlite (chloride form) (IRA-410) to exchange the counter ion and obtain the water-soluble aldehyde **A1** as a white solid (3.6 g, 13.4 mmol, 80 %) ^{1}H NMR (D_2O, 300 MHz): δ = 3.07 (s, 9H), 3.46 (t, 2H, J = 6.0 Hz), 3.73 (t, 2H, J = 6.0 Hz), 7.73 (d, 2H, J = 9.0 Hz), 7.83 (d, 2H, J = 9.0 Hz), 9.80 (s, 1H). ^{13}C NMR ($CDCl_3$, 75MHz): δ = 34.1, 53.2, 64.0, 127.8, 130.1, 138.0, 138.3, 169.7 and 195.5 ppm (Appendix B). High-resolution mass spectrometry was performed using a Waters LCT Premier mass spectrometer (water Inc.). HRMS^{+} $C_{13}H_{19}N_2O_2$: Theoretical: 235.14. Actual: 235.15.

2.5.2 Synthesis of 4-formylbenzoyl chloride (1) and 2-fluoro-4-formylbenzoyl chloride (2).

4-Carboxybenzaldehyde (3.0 g, 20 mmol) was dissolved in $PhCH_3$ (300 mL) followed by the addition of $SOCl_2$ (11 mL, 160 mmol). The mixture was refluxed for 18 h and residual $SOCl_2$ was removed under reduced pressure to obtain **1**. ^{1}H NMR ($CDCl_3$, 300 MHz): δ = 8.04 (d, 2H, J = 9.0 Hz, 8.27 (d, 2H, J = 9.0 Hz), 10.15 (s, 1H). ^{13}C NMR ($CDCl_3$, 75MHz): δ = 129.9, 131.9, 140.5, 166.8, 167.7, 169.7 and 191.1 ppm. The same procedure was repeated using 2-fluoro-4-formylbenzoic acid to obtain 2-fluoro-4-formylbenzoyl chloride **2** as pale-yellow oil. ^{1}H NMR ($CDCl_3$, 300 MHz): δ = 7.66 (dd, 1H, J = 12.0 Hz), 7.75 (dd, 1H, J = 6.0 Hz), 8.19 (t, 1H, J = 6), 10.1 (s, 1H). ^{13}C NMR ($CDCl_3$, 75MHz): δ = 117.2, 117.5, 119.9, 125.2, 134.6, 163.2, 165.3 and 189.5 ppm.

2.5.3 Hydrazone and imine hydrolysis

All pH measurements were made using a Hanna HI 90103 instrument which was calibrated regularly using commercial buffer solutions (Sigma-Aldrich). Aliquots of 1 M or 0.1 M NaOH and HCl were used to increase and lower the pH in all reactions. In a typical experiment, aldehyde **A1** (3 mL, 20 mM) and (carboxymethyl)trimethylammonium chloride hydrazide **HZ1** (3 mL, 20 mM) were dissolved in D_2O at room temperature. The solutions were mixed and the pH adjusted to pH 12.0 with aliquots of $NaOH_{(aq)}$ (1 M). The mixture was analysed by ^{1}H NMR spectroscopy and the complete conversion of the reaction was confirmed by appearance of the CH signal of the hydrazone bond ($\delta \sim 8$ ppm). The pH of the mixture

was slowly titrated with $H_3PO_{4(aq)}$ (1 M) and the hydrolysis monitored by ^1H NMR spectroscopy. After titration with $H_3PO_{4(aq)}$ (1 M), the sample was left to equilibrate for 30 min and the pH was measured again to confirm the pH value. The sample was then analysed by ^1H NMR spectroscopy to determine the yield of hydrazone by integration of aldehyde and hydrazone signals, using tetramethylsilane (TMS) as an internal standard. The same procedure was repeated for all aldehydes, hydrazides and amines, and the polymer system described in Chapter 4. The formation of imines was also performed in 1:10 molar ratios. The yields of hydrazones or imines were calculated according to equation 9 and 10, respectively:

$$\text{Yield of hydrazone (\%)} = 100 \times ((f_{\text{Hydrazone}})/ (f_{\text{Hydrazone}}+f_{\text{aldehyde}})) \qquad \textit{Equation 9}$$

$$\text{Yield of imine (\%)} = 100 \times ((f_{\text{Imine}})/ (f_{\text{Imine}}+f_{\text{aldehyde}})) \qquad \textit{Equation 10}$$

Where f is the integral value of each signal.

2.5.4 Synthesis of pHEMA-b-pPEGMA by RAFT polymerisation

2.5.4.1 Synthesis of macroCTA pPEGMA (P5)

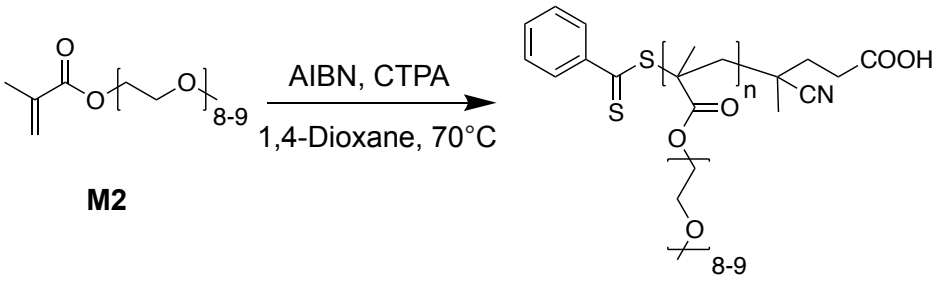

M2

Scheme 2.3: Synthesis of macroCTA **P5** by RAFT polymerisation**.**

CTPA (22.4 mg, 0.08 mmol, 1 eq) and AIBN (2.63 mg, 0.016 mmol, 0.2 eq) were added to a small Schlenk tube (Scheme 2.3). Poly(ethylene glycol) methyl ether methacrylate (PEGMA, M_n: 500 g mol^{-1}) (**M2)** (4 g, 8.0 mmol, 100 eq) was passed through a column of activated basic alumina to remove the inhibitor and then added to the mixture. After addition of 1,4-dioxane (5 mL), the reaction mixture was degassed through five freeze-pump-thaw cycles before the vessel was backfilled with N_2 and allowed to warm to room temperature. The reaction mixture was then placed in an oil bath at 70 °C and the polymerisation was quenched after 3 h (Scheme 2.3). The reaction mixture was dialysed in CH_2Cl_2:MeOH (50:50 v/v) and evaporated to dryness

to obtain **P5** as a pink oil. ^{1}H NMR (300 MHz, $CDCl_3$): δ = 0.65 – 1.13 (br, $CHCH_3$, polymer backbone), 1.54 – 2.06 (br, $CHCH_2$, polymer backbone), 3.31 – 3.40 (br, -OCH_3), 3.42 – 3.48 (br, -CH_2O), 3.50 – 3.77 (br, -CH_2CH_2, ethylene glycol chain), 3.95 – 4.25 (br, -OCH_2), 7.30 – 7.43 (br, Ar, polymer endgroup), 7.45 – 7.56 (br, Ar, polymer endgroup), 7.73 – 7.90 (br, Ar, polymer endgroup). The composition of **P5** was determined by comparing the integrals of the characteristic aromatic protons of the polymer endgroup with the integral of the methoxy methyl (-OCH_3) protons of the side chain of the monomer.

2.5.4.2 Copolymerisation of HEMA monomer M3 (P6)

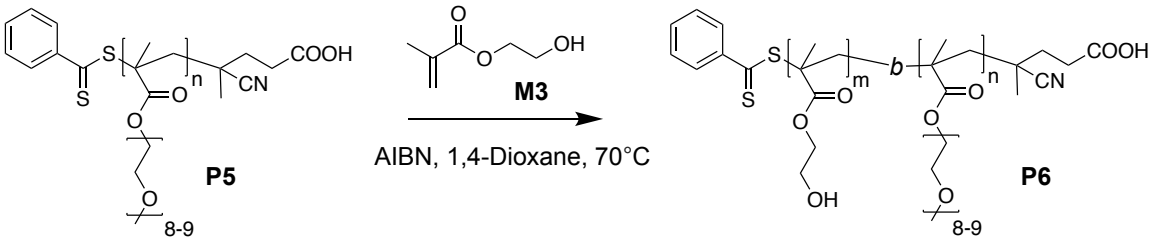

Scheme 2.4: Synthesis of diblock copolymer **P6** by RAFT polymerisation.

In a typical example, the macroCTA **P5** (463.0 mg, 0.01 mmol, 1 eq) and AIBN (0.82 mg, 0.005 mmol, 0.3 eq) were added to a small Schlenk tube (Scheme 2.4). 2-hydroxyethyl methacrylate **M3** (HEMA, M_w: 130.14 g mol^{-1},130.14 mg, 1.0 mmol, 100 eq) was added to the mixture followed by the addition of 1,4-dioxane (3 mL). The reaction mixture was degassed through five freeze-pump-thaw cycles and then was backfilled with N_2 and placed in an oil bath at 70 °C. After 6 h the polymerisation was quenched in liquid nitrogen and the reaction mixture was dialysed in CH_2Cl_2:MeOH (50:50 v/v) and evaporated to dryness to obtain **P6** as a pink oil. ^{1}H NMR (300 MHz, D_2O): δ = 0.64 – 1.30 (br, $CHCH_3$, polymer backbone), 1.70 – 2.35 (br, $CHCH_2$, polymer backbone), 3.37 – 3.45 (br, -OCH_3, pPEGMA block), 3.58 – 4.00 (br, -OCH_2CH_2, ethylene glycol chain), 4.04 – 4.34 (br, -OCH_2, pHEMA and pPEGMA block). The composition of **P6** was determined by comparing the integration of the methoxy methyl (-OCH_3) protons from the pPEGMA block with the integration of the overlapped signals of the ethylene glycol chain (-OCH_2) of the pHEMA and pPEGMA blocks. The same procedure was repeated for poly(ethylene glycol) methacrylate monomer **M4** (PHEMA, M_n: 500 g mol^{-1}) varying the equivalence of AIBN and the polymerisation solvent to obtain the diblock copolymers **P8**, **P9**, **P10** and **P11** (Table 2.14).

Table 2.14: Conditions for the RAFT polymerisation of diblock copolymers.

Polymer	Molar Ratios [M]/[CTA]/[I]	Solvent	Time	Monomer conversion
P6	100/1.0/**0.3**	1,4-dioxane	6 hours	47 %
P8	100/1.0/**0.3**	1,4-dioxane	3 h	32 %
P9	100/1.0/**0.5**	1,4-dioxane	3 h	50 %
P10	100/1.0/**0.5**	**Toluene**	Overnight	34 %
P11	100/1.0/**0.5**	**DMF**	3 h	54 %

2.5.5 Synthesis of aldehyde-functionalised di-blocks

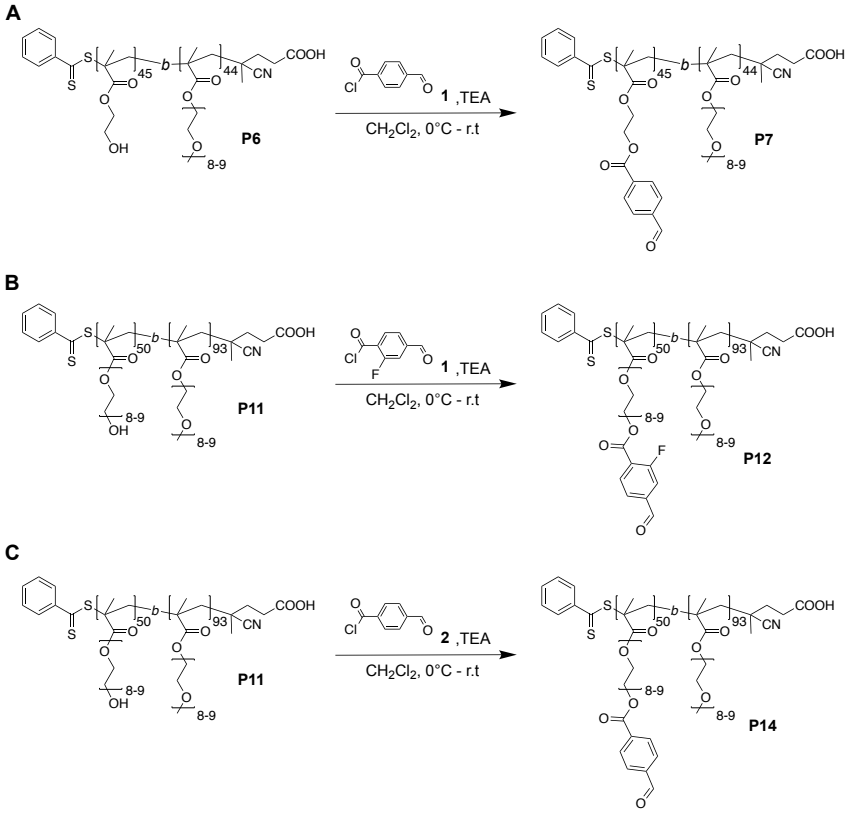

Scheme 2.5: *Synthesis of aldehyde functionalised polymers.*

Diblock copolymer pHEMA-*b*-pPEGMA (**P6**, M_n: 28,200 g mol^{-1}, 126 mg, 0.196 mmol -OH, 1.0 eq) was dissolved in CH_2Cl_2 (8 mL) and added to a round bottom flask in an ice-bath followed by addition of triethylamine (39.5 mg, 0.40 mmol, 2.0 eq). 4-Formylbenzoyl chloride **1** (165 .0mg, 0.975 mmol, 5.0 eq) was dissolved in CH_2Cl_2 (8 mL) and added dropwise to the reaction mixture (Scheme 2.5 A). After 18 h, the reaction mixture was evaporated to dryness and dialysed in MeOH. The polymer was evaporated to dryness to obtain **P7** as a pale pink oil. The same procedure was repeated with **P11** to obtain the aldehyde-functionalised polymer **P14** (Scheme 2.5 C). For the fluoro-monosubstituted aldehyde polymer, **P11** was reacted with 2-fluoro-4-

formylbenzoyl chloride **2** to obtain **P12** (Scheme 2.5 B) as a pale yellow solid. ^{1}H NMR (300 MHz, $CDCl_3$) **P7**: The polymer showed the characteristics signals of the polymer backbone and the ethylene glycol chain of the pPEGMA block. The signal of the ethylene glycol chain from the pPHEMA block appeared shifted to downfield at δ = 4.19 – 4.36 (br, -OCH_2) and 4.40 – 4.66 (br, -CH_2O). The aldehyde signals appeared at δ = 7.83 – 8.36 (br, aromatic protons) and 9.84 and 10.30 br, -CH, aldehyde protons). The yield of the aldehyde functionalisation of **P7** was determined by comparing the integration of the methoxy methyl (-OCH_3) protons from the pPEGMA block with the integration of the aldehyde signals (-CH and Ar protons) of the pPHEMA block. The same procedure was repeated for polymer **P12** and **P13**.

2.5.6 Synthesis of hydrazone-functionalised polymers

In a typical example, **P12** (Scheme 2.6 A) (M_n: 76,400 g mol^{-1},146 mg, 0.115 mmol aldehyde, 1.0 eq) was dissolved in MeOH followed by the addition of (77 mg, 0.46 mmol, 4.0 eq) **HZ1**. After 24 h, the reaction mixture was purified by dialysis in ultra-pure water and freeze-dried to obtain **P13** as a pale-yellow solid. The yield of hydrazone functionalisation was determined by the disappearance of the aldehyde signals ($\delta \sim$ 10.0 ppm) in the ^{1}H NMR spectrum. The same procedure was repeated to obtain **P15** (Scheme 2.6 B).

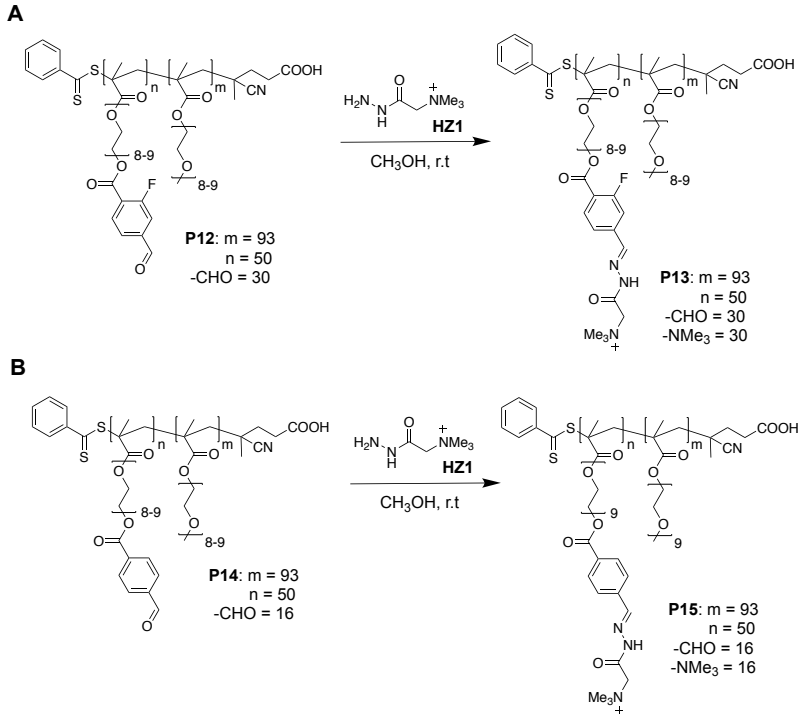

Scheme 2.6: Synthesis of hydrazone functionalised polymers.

2.5.7 Polyplex formation between hydrazone-polymers and siRNA

The polyplexes (**P13siPP** and **P15siPP**) were obtained by self-assembly of the polymer solutions with siRNA. A solution of siRNA in RNAse-free water (50 μL, 4 μM) was mixed with the polymer solutions (50 μL) in different molar ratios. The N/P ratios were calculated by the ratio of the positive charges (ammonium groups within the polymer) to the negative charges (phosphate groups within siRNA, final conc. 80 μM). After complexation at different N/P ratios, the samples were incubated for 1 h at room temperature.

2.5.8 Gel retardation assay

An agarose gel electrophoresis assay or gel retardation assay was performed to evaluate the loading capacity of the polyplexes. A 3 % agarose gel was prepared in 0.5 X TBE buffer. 5 μL of 10,000X GelRed staining (Biotium) was added to the gel before casting. 2 μL of 6X DNA loading buffer (Fermentas) was mixed with 8 μL of sample, and samples were loaded into wells. The gel was allowed to run for 1 h at 80 V in 0.5 X TBE buffer and visualised with a BioRad transluminator (UV).

2.5.9 Conjugation of hydrazone-polymers to AuNPs

AuNPs (1.16 nM, 100 μL) were incubated overnight with different molar ratios of **P13** or **P15** in a 96 well-plate. After 24 h, 10 μL of $NaCl_{(aq)}$ (1 M) (final conc. 100 mM) was added and the UV-Vis spectrum was acquired using a FLUOstar Omega Microplate Reader between 350-700 nm and wavelength interval of 2 nm. To determine the ideal polymer concentration to be used on the coating of 20 nm AuNPs, the induced aggregation factor was determined by calculating the ratio $\lambda_{615}/\lambda_{524}$. Uncoated AuNPs were used as a control.

2.5.10 Preparation of AuNPs coated with hydrazone-polymers and siRNA

AuNPs (11.6 nM, 100 μL) were first incubated overnight with **P13** (10 μL) at different molar ratios (1:100, 1:500 and 1:1,000). Particles were then purified by centrifugation at 15,000 × g for 10 min and washed three times with Hepes buffer pH 7.4. 2 μL of siRNA (final concentration 0.4 μM) was added and the suspension was allowed to equilibrate for 1 h. The loading efficiency was determined by the indirect quantification method using the Qubit miRNA kit as previously described in section 2.3.5.1. Table 2.15 shows the composition for the particles formed.

Table 2.15: Compositions of AuNPs coated with hydrazone-polymers and siRNA.

Particles	AuNP:Polymer molar ratios	N/P ratios
$P13_{100}si_2NP$	1:100	2
$P13_{500}si_{10}NP$	1:500	10
$P13_{1,000}si_{20}NP$	1:1,000	20
$P15_{100}si_{1.2}NP$	1:100	1.2
$P15_{500}si_6NP$	1:500	6
$P15_{1,000}si_{12}NP$	1:1,000	12

2.5.11 Stability of $P13_{1,000}si_{20}NP$ in different pHs

Particles **$P13_{1,000}si_{20}NP$** (25 μL) were incubated with phosphate buffer 10 mM (75 μL) at pH 7.2 and 5.0. After 24 h, the particles were isolated by centrifugation at 15,000 × g for 15 min and the supernatants collected for quantification of released siRNA. The concentration of siRNA was determined using the QubiT microRNA kit.

2.6 References

1 J. Stetefeld, S. A. McKenna and T. R. Patel, *Biophys. Rev.*, 2016, **8**, 409–427.

2 D. E. Koppel, *J. Chem. Phys.*, 1972, **57**, 4814–4820.

3 D. A. Chalton and J. H. Lakey, *Anal. Chem.*, 2010, **82**, 3073–3076.

Chapter 3
Phosphorothioate modified siRNA for conjugation onto gold nanoparticles

3.1 Introduction

Since the discovery of RNA interference by Fire & Mello,[1] siRNA provides a new perspective for treatment of intractable and genetic related diseases. However, the safe and efficient delivery of siRNA to the target cytoplasm is still a major challenge in RNAi therapy.[2] This challenge arises as naked siRNA molecules are susceptible to enzymatic degradation in the body and also possess anionic charges that supress the penetration into cellular membrane.[3] Hence, the design and development of new nanocarriers is essential to overcome these delivery challenges.

Gold nanoparticles (AuNPs) have been a promising tool for bioapplications such as biosensing, bioimaging and drug delivery on account of their unique chemical and physical properties. In addition to the specific optical properties depending on their size and morphology, AuNPs can be surface modified with biomolecules and polymers through thiol chemistry to optimise colloidal stability and biocompatibility.[4] Thiol modification of nucleic acids is the main approach successfully used for the functionalisation of gold surfaces, a process driven by the formation of the strong gold-thiol interactions.[5,6] Mirkin *et al*.[7] were one of the first groups to report the chemisorption of thiolated oligonucleotides to AuNPs. The group prepared 13 nm AuNPs coated with two different single strands of thiolated DNA oligonucleotides. After addition of a complementary sequence that binds to a portion of both strands (linker), AuNP aggregation was observed. The findings demonstrated the successful coating of AuNPs with thiolated oligonucleotides and post-hybridisation of the grafted sequences. They further reported[8] the synthesis of DNA oligonucleotide-AuNPs conjugates by evaluating the surface coverage and stability of oligonucleotide probes featuring one thiol modification, a disulfide or three thiol modifications. They reported that the conjugates prepared with the trithiol oligonucleotide showed significantly higher stability against DDT than the conjugates prepared with monothiol or disulfide terminated oligonucleotides. Moreover, the conjugates prepared with the trithiol oligonucleotide showed the highest surface coverage, and thus, indicated that the oligonucleotides bearing three thiol modifications exhibit higher loading on the AuNPs surface.[8]

Although thiolated nucleic acids have been widely used to achieve successful functionalisation of gold nanoparticles, thiol-modified siRNAs are expensive to synthesize and can be difficult to work with as thiol groups can easily be oxidised to disulfides. An interesting alternative approach is the utilisation of nucleic acids whose

non-bridging phosphate oxygen atoms have been substitute by sulfurs, so-called phosphorothioate modification (PS) (Figure 3.1).

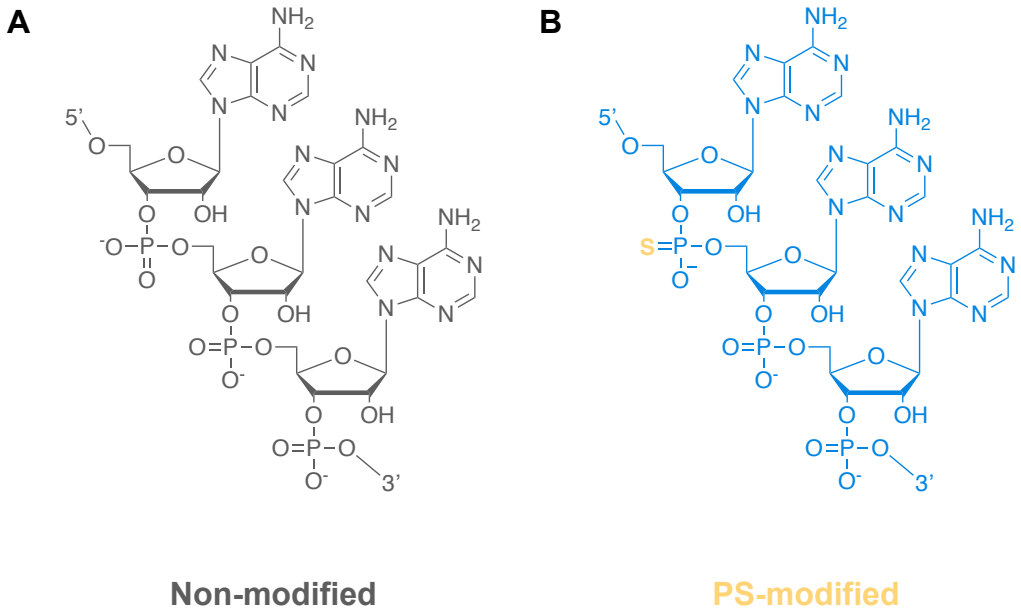

Figure 3.1: Chemical structure of (A) non-modified and (B) phosphorothioate (PS) modified nucleic acids.

Phosphorothioate-modified nucleic acids can be synthesised by conventional solid phase synthesis and cost only 3% of the price of thiol-modified oligo.[9] Moreover, phosphorothioates can also be adsorbed to gold surfaces,[10] possess increased stability towards degradation by nucleases,[11] and thus are promising candidates for conjugation of modified siRNAs to AuNPs.

For the success of RNAi therapy, the safe release of siRNA into the cell cytoplasm is essential. The ideal delivery platform must be stable at physiological pH and promote the fast release of siRNA into the cytosol, allowing the RNAi mechanism to operate. Nanoparticles that possess a bioresponsive behaviour are essential for siRNA delivery platforms. The sulfur-Au bond is relatively stable in physiological fluids and in the extracellular space, however, it is labile in the cytosol due to a redox imbalance of glutathione (GSH), a thiol reducing agent that can bind to Au.[12] The difference in the extracellular concentrations (~ 2–10 $\times$ 10^{-6} M) versus intracellular concentrations (~ 2–10 $\times$ 10^{-3} M) of GSH[13] offers an intracellular specifc response to AuNPs coated with PS-modified siRNA. In extracellular conditions, the delivery platform would remain stable, however, once in the cytosol, the higher concentrations of GSH would bind to the AuNPs, triggering the displacement and release of PS-siRNA (Figure 3.2).

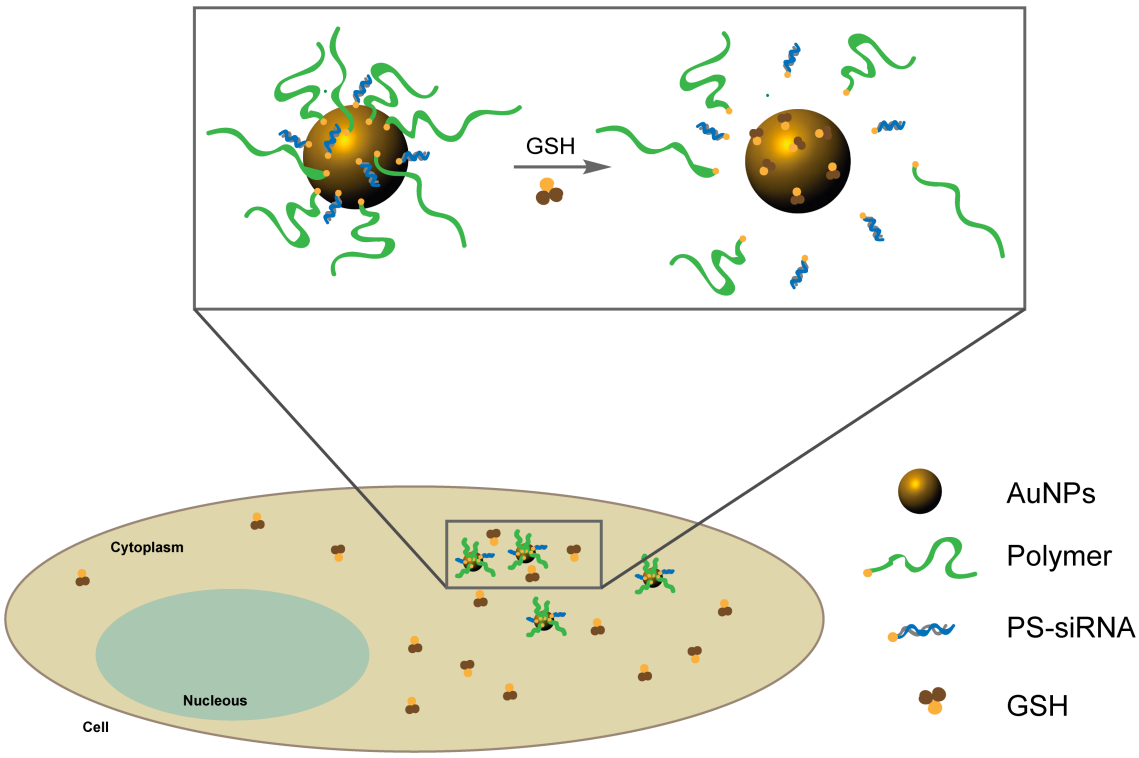

Figure 3.2: Mechanism for intracellular siRNA release mediated by glutathione (GSH). High intracellular concentrations of GSH competitively bind to AuNPs, displacing the PS-siRNA and polymer into the cytosol of target cell.

A main concern in siRNA delivery is the colloidal stability and biocompatibility of *in vivo* nanocarriers. To be able to deliver therapeutic concentrations of siRNA to the target cell, a nanocarrier must be sufficiently stable in the blood circulation and present prolonged half-life circulation. Surface modification of nanoparticles with polyethylene glycol, termed PEGylation, has shown to be safe and effective in providing stability and increased blood circulation *in vivo.*[14] The hydrophilicity of PEG provides steric shielding of the AuNP in aqueous solutions, resulting in colloidal stability and preventing unwanted recognition of particles by the immune system.[15]

In this chapter, AuNPs functionalised with hydrophilic PEG chains and modified PS-siRNA were prepared (Figure 3.3). The polymer poly(ethylene glycol methyl ether methacrylate) (pPEGMA) was synthesised by reversible addition fragmentation chain transfer (RAFT) polymerisation. The polymers were conjugated onto AuNPs through chemisorption of their dithioester end groups. The loading efficiency of PS-siRNA was evaluated and gene silencing of *RUNX1/ETO* gene assessed.

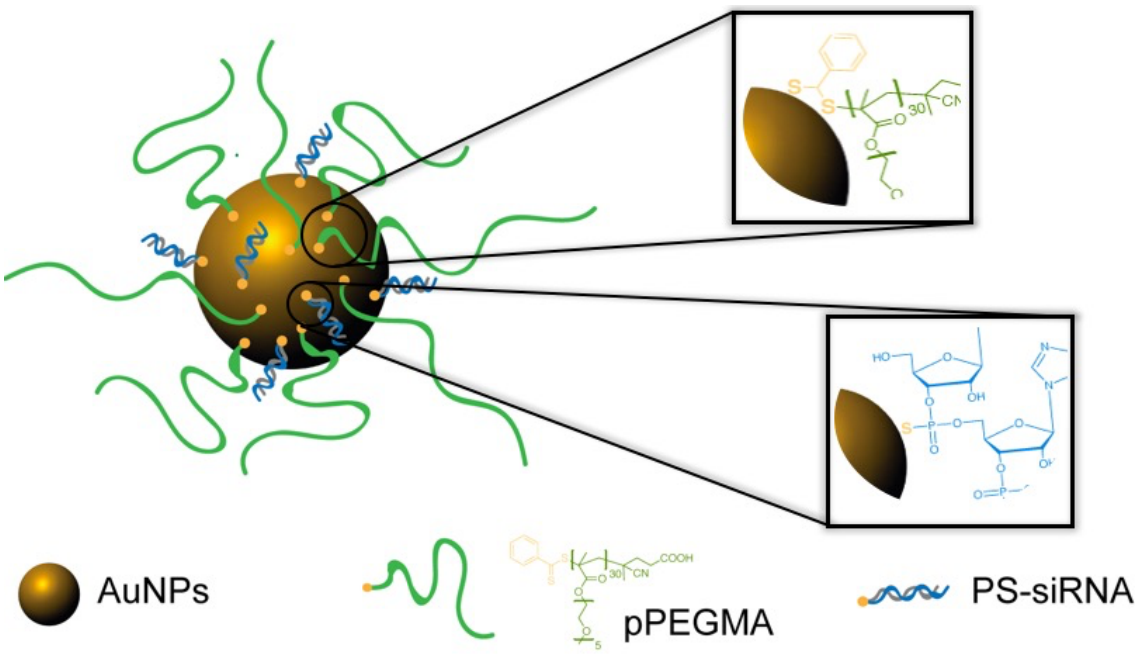

Figure 3.3: Scheme of AuNPs coated with PS-siRNA and pPEGMA. pPEGMA is conjugated through anchoring the dithioester of the polymer end groups into gold. Modified siRNA is conjugated through the PS substitution in the non-bridging phosphate oxygen atom.

3.2 Results and Discussion

Herein the design, preparation and characterisation of AuNPs coated with PS-modified nucleic acids and pPEGMA are described. The nomenclature of the nanoparticles is summarised (Figure 3.4) and describes the type of modified nucleic acid and the polymer formulation conjugated onto the AuNP. When different protocols were tested, or by changing the formulation conditions or the components added, the letter T was added to the nomenclature followed by the formulation number (*e.g.* **PSsiNP.P1-T1**).

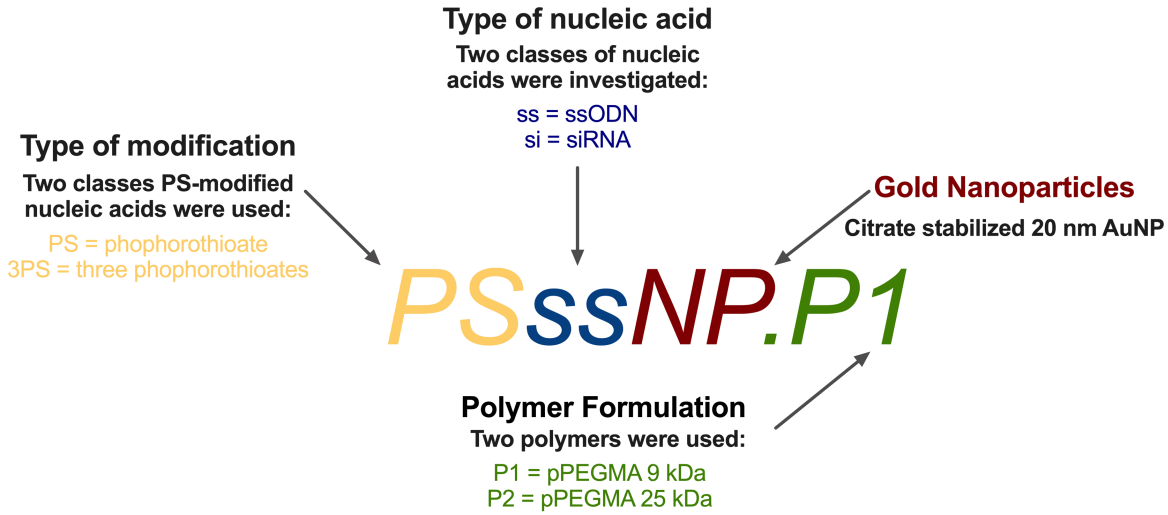

Figure 3.4: Nanoparticle nomenclature. AuNPs were coated with single strand oligonucleotide (ssODN) or short interfering RNA (siRNA) and pPEGMA polymer of different molecular weight (**P1** or **P2**).

Two generations of functionalised AuNPs were investigated. The first generation of nanoparticles (**PSssNP**) investigated were prepared by coating AuNPs of 20 nm size with PS-modified single strand oligonucleotide (PS-ssODN) and pPEGMA. The PS-ssODN was first conjugated to AuNPs because is cheaper to purchase than modified siRNAs, and thus was used to prove the hypothesis of functionalisation onto gold surfaces through the PS modification. The second generation of nanoparticles were developed to load siRNA (**PSsiNP**). **PSsiNPs** were prepared by functionalizing AuNPs with pPEGMA and PS-modified siRNA that features either one (PS-siRNA) or three (3PS-siRNA) PS modifications on their siRNA sequences. The resulting particles were characterised and the loading efficiency and gene silencing were evaluated. Figure 3.5 shows the particles prepared in this chapter.

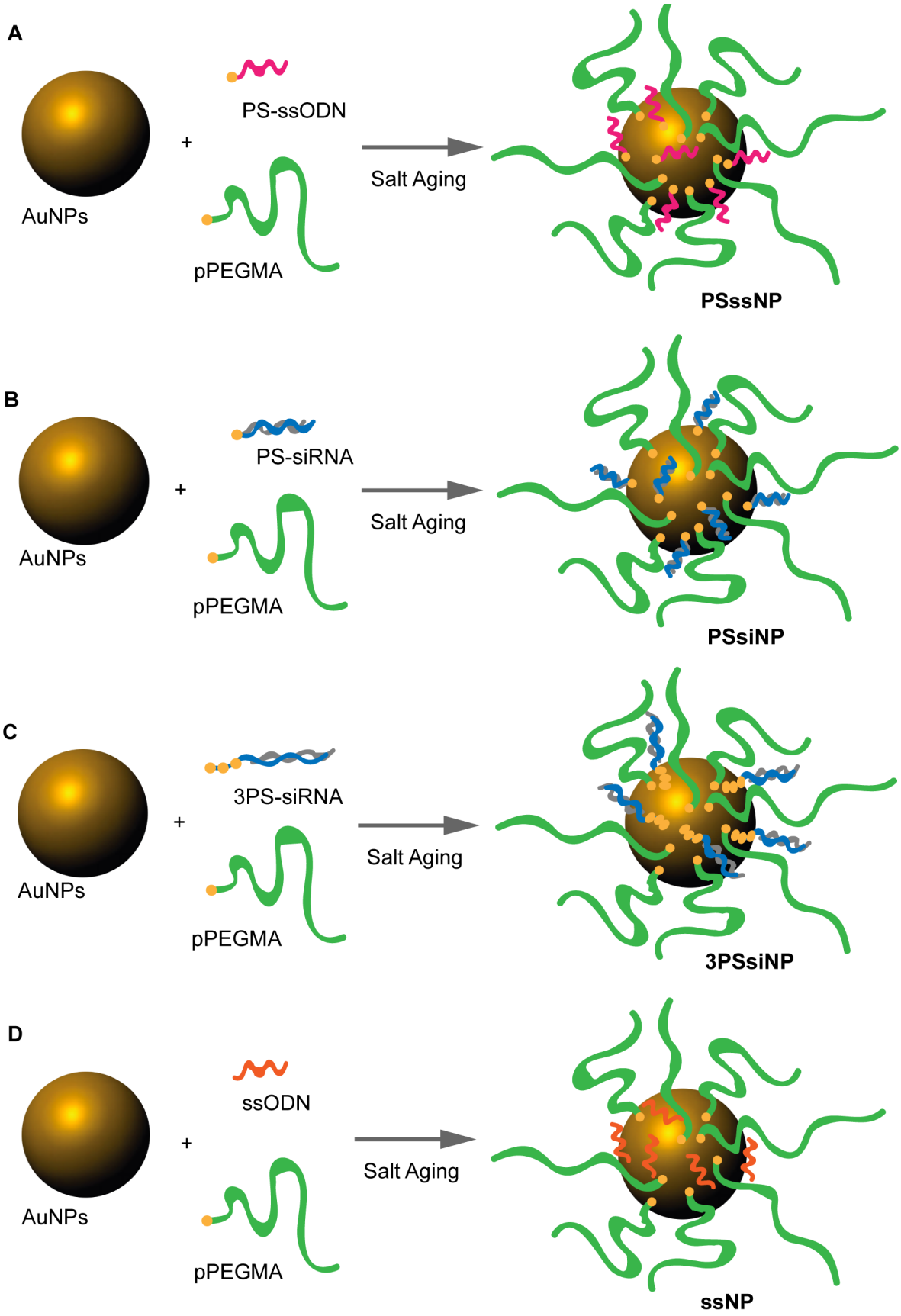

Figure 3.5: Nanoparticles prepared by coating AuNPs with pPEGMA (**P1** or **P2**) and (A) PS-ssODN, (B) PS-siRNA, (C) 3PS-siRNA and (D) non-modified ssODN. The salt aging is the method used to promote the conjugation of nucleic acids onto gold surfaces and is based on the slow titration of $NaCl_{(aq)}$.

3.2.1 Synthesis and characterisation of pPEGMA polymer prepared by RAFT polymerisation

RAFT polymerisation is a versatile technique that allows the controlled synthesis of homopolymers and block copolymers with very low polydispersity.[16] Thus, polymers produced by RAFT polymerisation are attractive building blocks for the functionalisation of AuNPs via the "grafting to" approach.[17] Polymer grafted gold nanoparticles can be obtained by the conjugation of AuNPs with thiol-functionalised polymers. This technique usually comprises the reduction of the terminal RAFT functionality to a thiol moiety by its reduction with nucleophiles such as primary amines.[18,19]

The polymers (**P1** and **P2**) were synthesised (Scheme 3.1) by RAFT polymerisation of poly(ethylene glycol) methyl ether methacrylate monomer **M1** ($PEGMA_{300}$ M_n: 300 g mol^{-1}) using 4-cyano-4-(thiobenzoylthio) pentanoic acid (CTPA) as chain transfer agent (CTA) and 2'-azobis(2-methylpropionitrile) (AIBN) as initiator. The polymerisation time was increased to obtain two pPEGMA polymers presenting different molecular weight. The use of CTPA as RAFT chain transfer agent produces polymers bearing a dithioester end group that can be chemisorbed onto gold without transformation to thiols.[20] Thus, the polymers obtained by RAFT polymerisation can be used for the functionalisation of gold nanoparticles via the "grafting to" approach without a subsequent synthetic step to reduce their end groups to thiols.

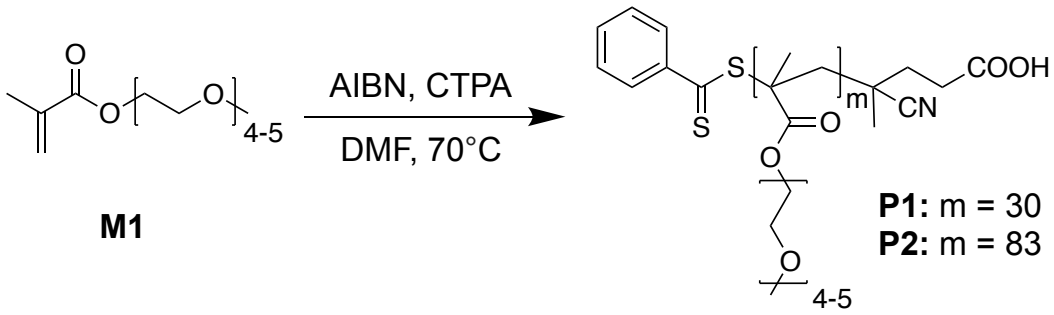

M1

Scheme 3.1: RAFT polymerisation of $PEGMA_{300}$ monomer **M1**. **P1** and **P2** polymers were obtained after 2 and 5 h of polymerisation, featuring 30 and 83 units of PEGMA, respectively.

The polymers were dialysed in water to remove unreacted monomers, freeze-dried to obtain pink oils and then characterised by ^1H NMR spectroscopy and gel permeation chromatography (GPC) (Table 3.1).

Table 3.1: Characterisation of **P1** and **P2**. [a] As determined by ^{1}H NMR spectroscopy (700 Hz, $CDCl_3$). [b] As determined by GPC in DMF (0.6 mL min^{-1} with 1g/L LiBr) calibrated against methyl methacrylate standards of very low polydispersity (PDI <1.08).

Polymer	M_n (g/mol)[a]	M_n (g/mol)[b]	M_w (g/mol)[b]	PDI[b]
P1	9,300	6,500	8,100	1.24
P2	25,200	19,200	23,200	1.21

The ^{1}H NMR spectra of **P1** and **P2** (Fig. 3.6 A and B, respectively) showed broadened signals, confirming the successful polymerisation of **M1**. The ^{1}H NMR spectrum of **P1** (Figure 3.6 A) showed well-defined signal at δ = 3.30 – 3.43, assigned to the terminal methoxyl groups (-OCH_3) of PEGMA side chains. The signal at δ = 3.57 – 3.77 corresponds to the protons of the ethylene glycol chains (-OCH_2CH_2) and the signals at δ = 0.64 – 1.14 and δ = 1.62 – 2.06 to the polymer backbone. The signals at δ = 7.30 – 7.40, δ = 7.45 – 7.54 and δ = 7.81 – 7. 89 ppm correspond to the aromatic protons of the polymer end group. These signals were used to determine the degree of polymerisation (DP) by comparing their integrals to those of the signal of the terminal methoxyl groups. For **P1**, the DP = 30 correspond to an average molecular weight (M_n) = 9 kDa. The ^{1}H NMR spectrum of **P2** (Figure 3.6 B) showed the characteristics signals for PEGMA as previously described for **P1**. End group analysis of **P2** indicated DP = 83 and M_n = 25 kDa. These results showed that by using RAFT polymerisation it is possible to obtain polymers of controlled chain lengths by merely changing the polymerisation times.

GPC analysis of **P1** and **P2** (Fig. 3.7 A and B) showed monomodal molecular weight distributions (PDI = 1.24 for **P1** and 1.21 for **P2**), indicating the polymerisations have proceeded with a good level of control. The shorter retention time for **P2** (23.91 min) (Fig. 3.7 B) when compared to **P1** (25.38 min) (Fig. 3.7 A), confirmed the difference in molecular weight determined by ^{1}H NMR spectroscopy. In addition, the M_n determined by GPC correlates reasonably well with M_n determined by ^{1}H NMR spectroscopy. The small differences observed could be attributed to the fact that the standards used for calibration (nearly monodisperse PMMA) are not pPEGMA standard polymers. Taken together, these results indicate the successful and controlled RAFT polymerisation of PEGMA to synthesise pPEGMA of distinctive sizes (**P1** and **P2**).

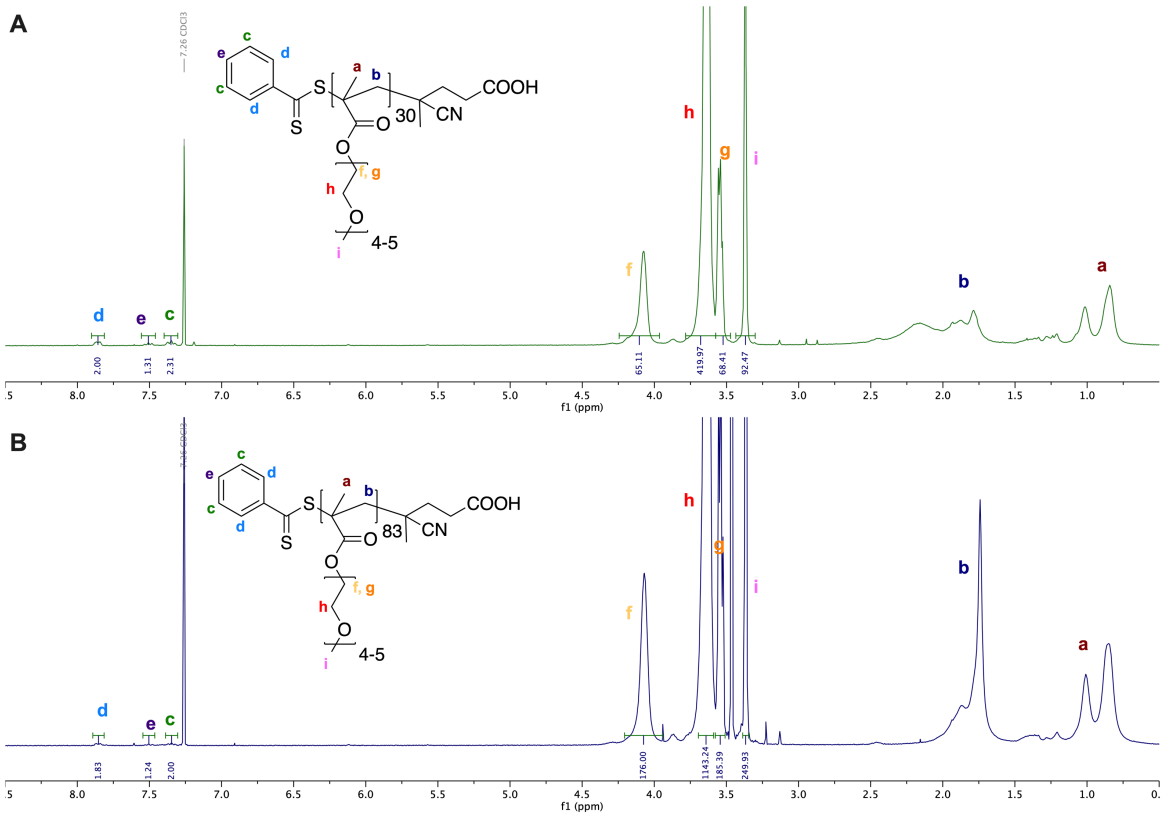

Figure 3.6: Characterisation of **P1** and **P2**. ^{1}H NMR spectrum (700 Hz, $CDCl_3$) of (A) **P1** and (C) **P2**. Protons signals are annotated with letters a-i corresponding to diagnostic protons on the polymer.

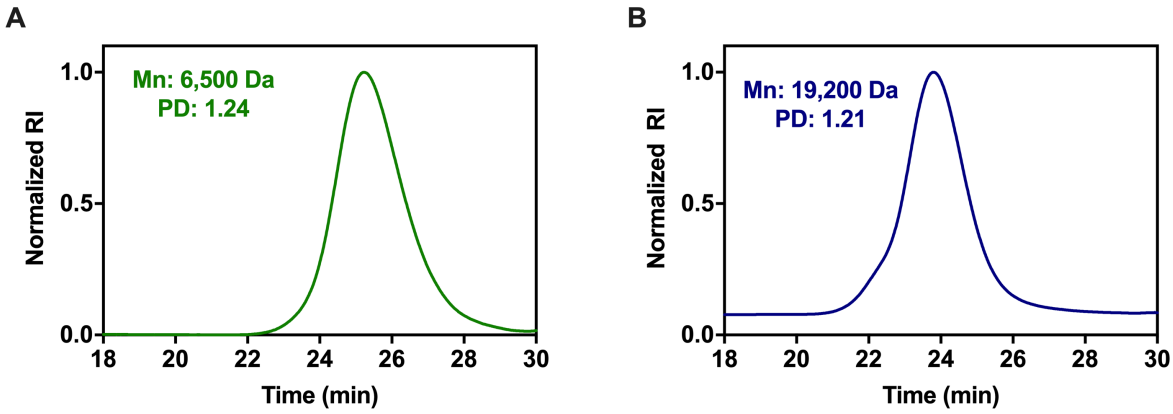

Figure 3.7: Normalised refractive index traces of (A) **P1** and (B) **P2** obtained by GPC analysis in DMF containing 1g/L of LiBr at 0.6 mL/min. Near monodisperse poly(methyl methacrylate) standards were used for calibration and the average molecular weight (M_n) determined as 6,500 Da for **P1** and 19,200 Da for **P2**.

3.2.2 Conjugation of pPEGMA to AuNPs

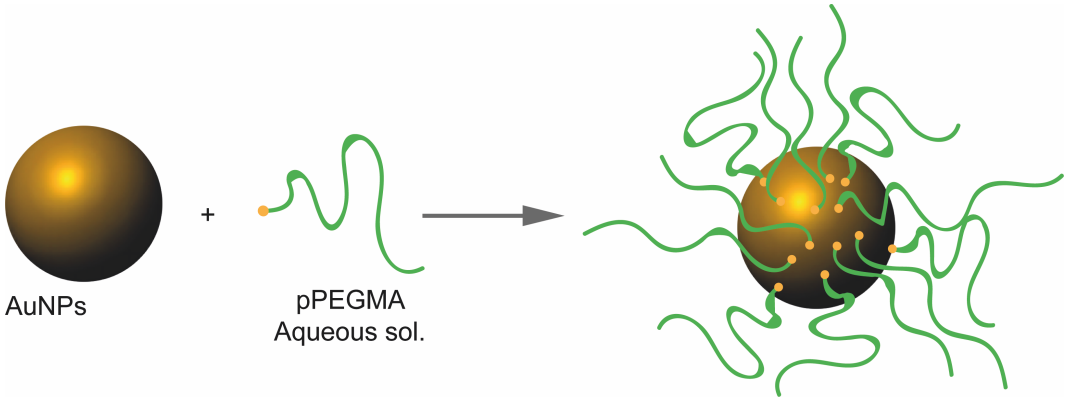

Figure 3.8: Preparation of AuNPs coated with pPEGMA. AuNPs were incubated with different ratios of aqueous solutions of **P1** or **P2** to obtained polymer grafted gold nanoparticles.

Citrate-stabilised gold nanoparticles of 20 nm size were functionalised with **P1** and **P2** by incubation of AuNPs with different molar ratios of polymer (Figure 3.8). To evaluate the amount of polymer needed to shield the gold core, 10 μL of $NaCl_{(aq)}$ (1.0 M) (final conc. 100 mM) was then added, and the UV-Vis spectrum recorded at 350-700 nm. In the presence of high concentration of salt, citrate-stabilised AuNPs tend to form permanent aggregates that may sediment out of solution as a precipitate. This process is known as salt-induced aggregation[21] and occurs on account of the electrostatic stabilisation of the negative charges of AuNPs by the salt ions. The surface plasmon band (λ_{SPR}) is a distinct absorption peak in the UV-Vis region due to the surface plasmon resonance (SPR) of gold nanoparticles.[22] The SPR of AuNPs is dependent upon their size and morphology, thus 20 nm citrate stabilised AuNPs present a SPR band at λ_{SPR} = 520 – 525 nm.[23] Large aggregates, as those formed by salt-induced aggregation, present a red-shift and broadening of the SPR band, resulting in a colour change of the solution from red to blue. Thus, the induced aggregation of polymer functionalised AuNPs after NaCl addition was evaluated by determining the aggregation factor calculated by the ratio $\lambda_{615}/\lambda_{524}$. The band at λ = 524 nm characterised the 20 nm AuNPs, while the absorbance increase at 615 nm is consistent with the red-shift of particle aggregation (Figure 3.9 A – inset c). Therefore, high values of aggregation factor imply gold nanoparticles aggregation. Figure 3.8 shows the salt-induced aggregation of nanoparticles coated with **P1** (Figure 3.9 A) and **P2** (Figure 3.9 B). Uncoated AuNPs were tested as a control, showing high aggregation factor values consistent with the expected salt-induced aggregation of citrate-stabilised AuNPs. For AuNPs coated with **P1**, 1,000 and 5,000-fold excess

molar ratios showed the lower values of aggregation factors after addition of $NaCl_{(aq)}$ (1M) (Figure 3.9 A).

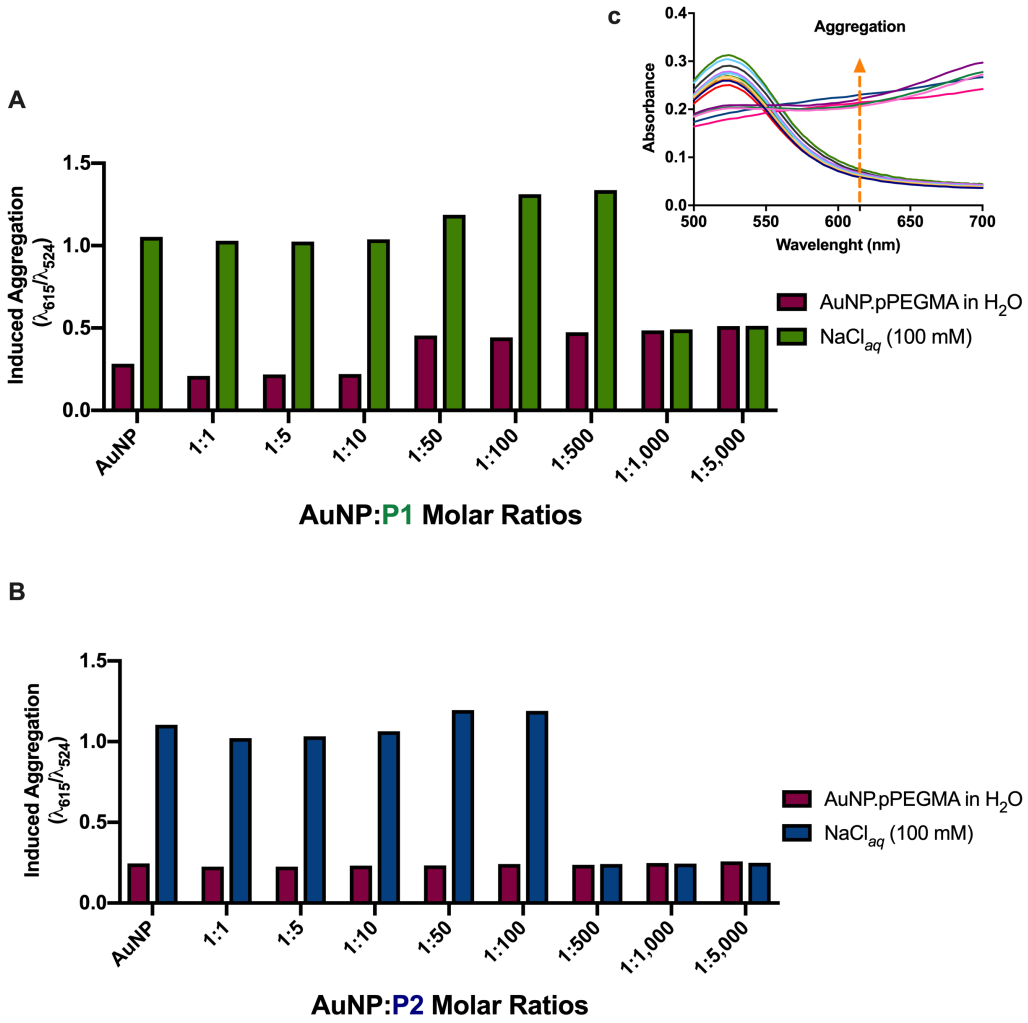

Figure 3.9: Stability of AuNPs coated with (A) **P1** and (B) **P2** at different polymer molar ratios in $NaCl_{(aq)}$ (1 M). Dark red bars show the aggregation factors obtained from UV-Vis experiments of polymer-functionalised AuNPs. Green (A) and blue (B) bars represent the aggregation factors after addition of $NaCl_{(aq)}$ (1 M). The inset (c) shows typical UV-Vis spectra of uncoated AuNPs after addition of 10 μL of $NaCl_{(aq)}$ (1 M), resulting in an absorbance increase at 615 nm.

Results with **P2** functionalised AuNPs indicated that only a 500-fold excess was necessary to maintain the low values of aggregation factor (Figure 3.9 B). The lower molar ratio of **P2** required to stabilize AuNPs can be attributed to the fact that **P2** has larger polymer chains than **P1**, and thus fewer polymer chains are required to shield the gold surface from NaCl. These results showed that the successful coating of AuNPs with polymers can be achieved by using RAFT polymers via the sulfur-Au chemistry, confirming that the dithioester end group chemisorbed onto Au.

3.2.3 Conjugation of Phosphorothioate-modified single strand oligonucleotide to AuNPs.

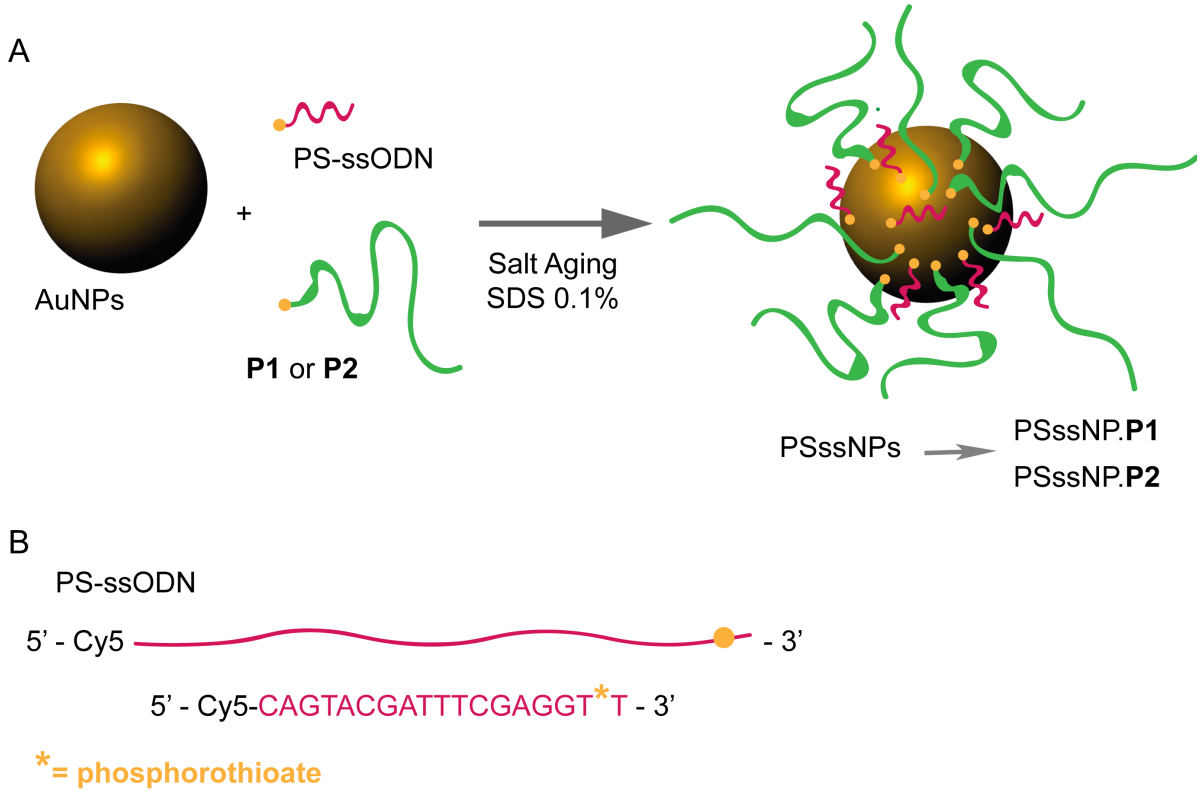

Figure 3.10: Preparation of AuNPs coated with pPEGMA and Cy5 labelled PS-ssODN. (A) Nanoparticles were prepared using the salt aging method SDS to obtain **PSssNPs.** (B) Phosphorothioate modified sequence of PS-ssODN.

PSssNPs were prepared using the "salt aging" approach.[5] This method is based on adding small concentrations of $NaCl_{(aq)}$ over a period of time. NaCl decreases the electrostatic repulsion between the negative charges of nucleic acids and citrate stabilised AuNPs and thus, promotes a better conjugation of nucleic acids to gold. However, the presence of salt can lead to unwanted aggregation that can be avoided by adding surfactant molecules to the salt aging process.[24] Herein, Cy5-labelled PS-modified single strand oligonucleotide (PS-ssODN) that features a single terminal PS-moiety was incubated with polymer (**P1** or **P2)** and 20 nm AuNPs in the presence of sodium dodecyl sulfate (SDS) to help optimize the conjugation of PS-ssODN (Figure 3.10). The particles were purified by centrifugation at 15,000 rpm for 10 min and washed three times with Hepes (10 mM). Table 3.2 summarizes the conditions to obtain **PSssNPs**.

Table 3.2: Preparation and characterisation of **PSssNPs**. AuNPs were coated with PS-ssODN and polymer (**P1** or **P2**) by salt aging method in the presence of SDS. [a]Determined by DLS measuments. [b]Determined by UV-Vis spectrum analysis.

PSssNPs	Molar ratios AuNP:PS-ssODN:pPEGMA	$[NaCl_{(aq)}]$	$[SDS_{(aq)}]$	NaCl titration time	Size (d.nm)[a]	PDI[a]	λ_{SP}[b] (nm)
PSssNP.P1	1:350:110	160 mM	0.1 %	3 h	35	0.2	527
PSssNP.P2	1:350:110	160 mM	0.1 %	3 h	31	0.2	526

DLS Measurements (Figure 3.11 A) of **PSssNPs** obtained showed a significant increase in size for particles prepared with **P1** (**PSssNP.P1** - green line) and **P2** (**PSssNP.P2** - blue line) and narrow unimodal distributions presenting polydispesity indices (PdI) of 0.2. The SPR band of 20 nm AuNPs determined by UV-Vis was λ_{SP} = 524 nm and is in accordance[23] with the expected value for spherical 20 nm citrate-stabilised AuNPs. In addition, **PSssNP.P1/P2** showed a small red-shift in the SPR band determined by UV-Vis (526 and 527 for **PSssNP.P1** and **PSssNP.P2**, respectively) (Figure 3.11 B). The red-shift of PSssNPs can be correlated with the increase in size by DLS, indicating the successful coating of AuNPs with PS-ssODN and pPEGMA (P1 or P2).

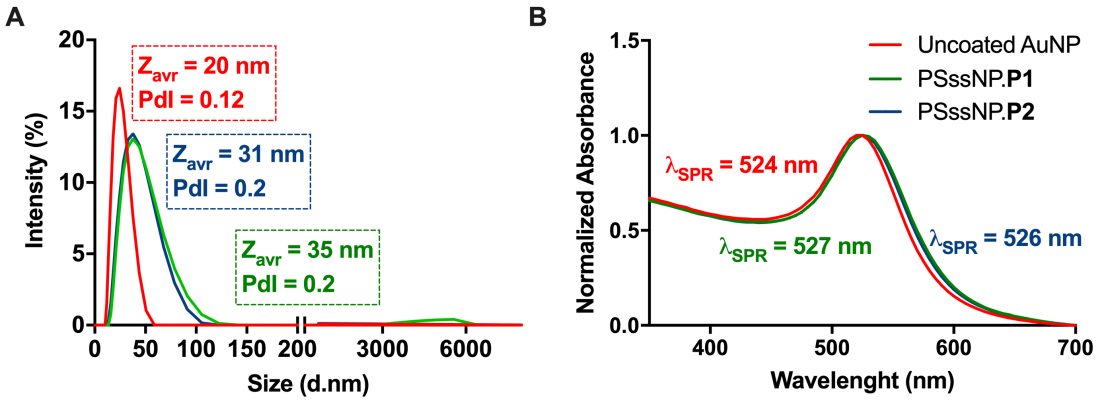

Figure 3.11: Characterisation by (A) DLS and (B) UV-Vis of AuNPs coated with PS-ssODN and pPEGMA. The green line shows the characterisation of particles prepared with **P1** (**PSssNP.P1**) and the blue line shows the characterisation of particles prepared with **P2** (**PSssNP.P2**).

The loading efficiency of PS-ssODN to AuNPs was evaluated by fluorescence spectroscopy using the indirect and the direct quantification methods (Chapter 2 – section 2.3.5). Indirect quantification is determined by the quantification of the amount of unloaded PS-ssODN (Figure 3.12 – black bars), from which the quantification of the loaded PS-ssODN can be inferred. To determine the amount of unloaded PS-ssODN,

the nanoparticles were isolated by centrifugation and the supernatant collected for quantification by fluorescence spectroscopy.

The direct quantification method, in which nucleic acids are cleaved from the AuNPs and then quantified, was used after the particles were purified by centrifugation in Hepes buffer (10 mM). The particles were then treated with DDT 100 mM to release the components from the AuNP surfaces. After particles were isolated by centrifugation, loaded PS-ssODN was quantified (Figure 3.12 – grey bars). When the indirect quantification is added to the direct quantification, the sum of the values should be very close to the initial concentration added, giving confidence in the measurements and indicating that the method is reliable to determine nucleic acid concentration in solution.

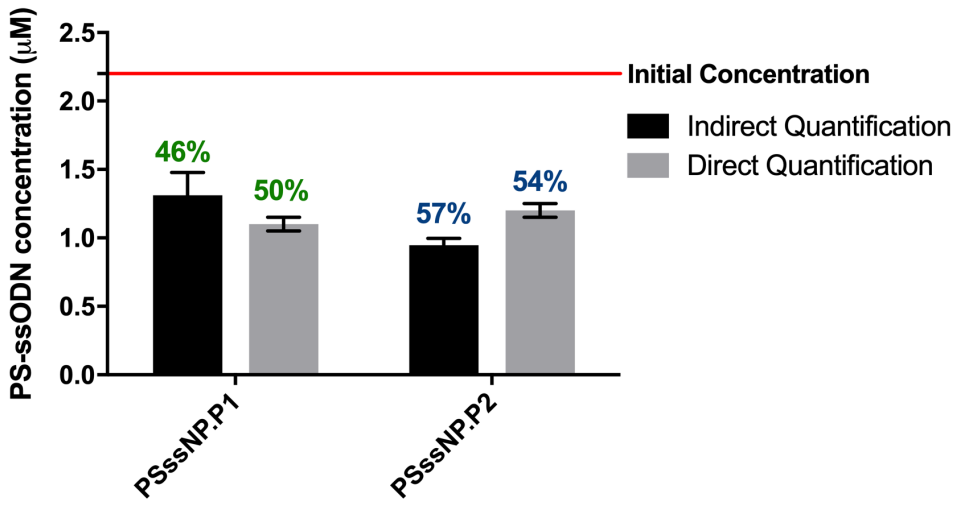

Figure 3.12: Quantification of loaded (grey bars) and unloaded (black bars) PS-ssODN by fluorescence spectroscopy. The indirect quantification was determined by measuring unloaded PS-ssODN in the supernatant of **PSssNPs**. The direct quantification was determined by measuring loaded PS-ssODN. The initial concentration (red line) was set to 100 % and the loading efficiency (%) calculated. The percentages above the quantification bars represent the calculated loading efficiency.

In both direct and indirect methods, the fluorescence values from samples were interpolated from previously prepared standard curves (Appendix A) to determine the concentration of PS-ssODN. Then, the loading efficiency was calculated by assuming the initial concentration added to the particles to be 100 % (Figure 3.12). Both **PSssNP.P1** and **PSssNP.P2** prepared showed similar loading efficiencies (≈ 50%). It is important to note that if the quantified concentration of unloaded PS-ssODN (Figure 3.12 – black bars) is added to the concentration of loaded PS-ssODN (Figure 3.12 – grey bars), their sums are close to the initial amounts added to the formulation. Furthermore, the loading efficiency (Figure 3.12) and the narrow unimodal size

distribution (Figure 3.11 A) presented by **PSssNPs** indicate that the salt aging process in the presence of a surfactant is effective in promoting the conjugation of PS-ssODN and polymer to AuNPs, and also prevents uncontrolled aggregation of nanoparticles.

For the safe delivery of nucleic acids into the cytosol of the target cell, nanocarriers must be stable for prolonged time in extracellular environment. The stability of **PSssNP.P2** was thus evaluated in tissue culture conditions, which are a reasonable mimic of extracellular conditions. **PSssNP.P2** were prepared and purified by centrifugation at 15,000 x g for 10 min. Then, **PSssNP.P2** were incubated at 37 °C in RPMI 1640 supplemented with 10% of fetal calf serum (FCS) at final concentration of 0.5 μM of PS-ssODN. At different time points, the samples were centrifuged and the supernatant collected to determine the concentration of PS-ssODN released from **PSssNP.P2**. As a control, naked PS-ssODN (in the absence of any AuNPs) at 0.5 μM was incubated with tissue culture medium in the same conditions. The concentration of PS-ssODN was determined by fluorescence spectroscopy and the values interpolated from a standard curve (Appendix A). Figure 3.13 A shows the quantification of PS-ssODN over time after incubation in tissue culture medium supplemented with FCS. The concentration of naked PS-ssODN decreased after 30 min of incubation with tissue cultured medium (Figure 3.13 A – blue bars) that can be attributed to unwanted degradation of naked PS-ssODN by nucleases in the FCS. Naked nucleic acids are known to present low stability due to fast degradation by DNAses and RNAses found in animal or human serum. Thus, the use of nanocarriers to protect nucleic acids against fast enzymatic degradation is essential to safely deliver the cargo to the cell cytosol. The stability of **PSssNP.P2** is shown in Figure 3.13 A (pink bars). The concentration of PS-ssODN was only detected after 4 h of incubation in tissue culture medium supplemented with FCS, and only 11% of PS-ssODN was released from **PSssNP.P2** (time point 24 h), indicating that PSssNP.P2 possess good stability in extracellular *in vitro* conditions.

The ability of PSssNP.P2 to release PS-ssODN upon exposure to GSH was also evaluated. GSH is a thiol reducing agent that is present in the cell cytoplasm in millimolar concentrations, whereas the extracellular concentrations values decrease by 1 – 3 orders of magnitude[25,26]. Thus, GSH is able to covalently bind onto AuNPs and displace loaded PS-ssODN.

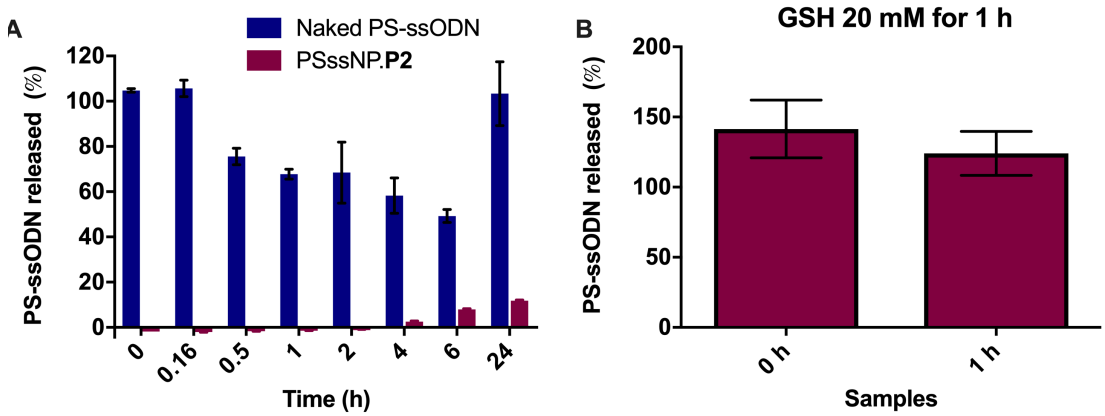

Figure 3.13: Stability of **PSssNP.P2** in different media. (A) Quantification over 24 h of Cy5 – labelled PS-ssODN in RPMI 1640 supplemented with 10% FCS. (B) Quantification of PS-ssODN released after addition of glutathione (20 mM).

To demonstrate the glutathione mediated response of **PSssNP.P2**, the samples at 0 h and 1 h from the stability assay showed in Figure 3.13 A were collected. These samples contain **PSssNP.P2** loaded with 0.5 μM of PS-ssODN in tissue culture medium supplemented with FCS. GSH at a final concentration of 20 mM was added and the samples were incubated for 1 h at 37 °C. After centrifugation, the supernatants were collected for quantification of PS-ssODN released from nanoparticles. Figure 3.13 B shows the GSH-response of **PSssNP.P2**. After 1 h treatment with GSH, PS-ssODN was recovered in the supernatant of both samples, indicating that the thiol reducing agent displaced PS-ssODN. The results shown in Figure 3.13 demonstrate the specific intracellular GSH-response of **PSssNP.P2**. In extracellular conditions the particles displayed good stability and did not release PS-ssODN (Figure 3.13 A). However, when in conditions that simulate the reducing environment of the cell cytosol, the nanoparticles were able to release the total concentration of PS-ssODN (Figure 3.13 B).

3.2.4 Conjugation of PS-siRNA to gold nanoparticles

The same salting aging procedure was used for the conjugation of phosphorothioate modified siRNA (PS-siRNA) to AuNPs to prepare **PSsiNPs**. The sequence of PS-siRNA used targets the *RUNX1/ETO* gene (PS-siRE). A second PS-siRNA sequence was used as a mismatch control (PS-siMM). Figure 3.14 shows the schematic representation of particles formed (A) and the PS-siRNA sequences (B and C). Table 3.3 shows the molar ratios used for **PSsiNP.P1** and **PSsiNP.P2** prepared with PS-siRNA.

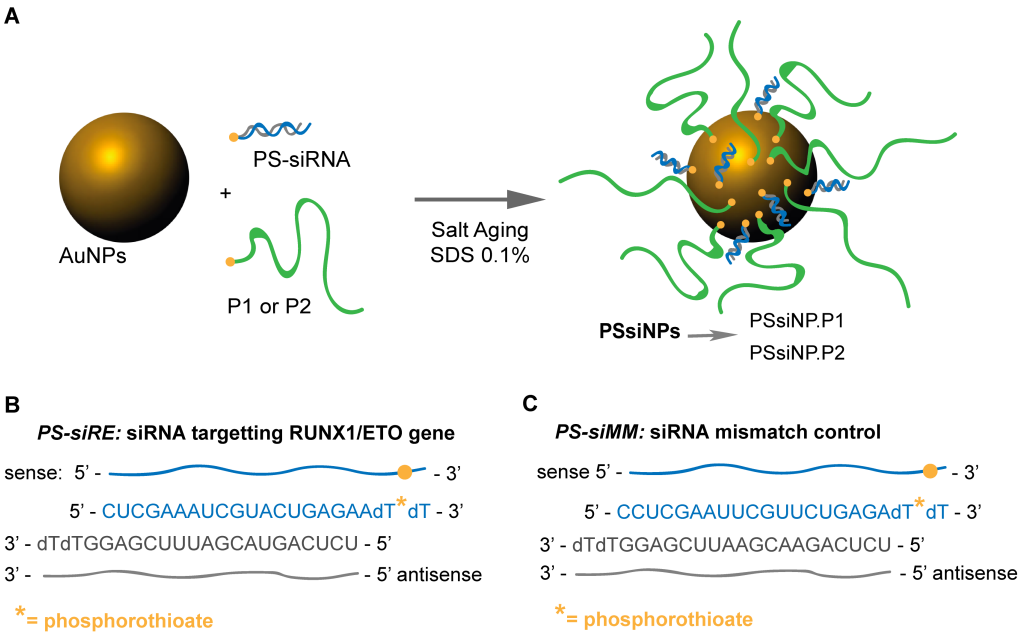

Figure 3.14: Preparation of AuNPs coated with PS-siRNA and pPEGMA. (A) Schematic representation of **PSsiNPs**. (B) Phosphorothioate modified siRNA sequence targeting *RUNX1/ETO* gene (PS-siRE). (C) Phosphorothioate modified siRNA sequence of mismatch control (PS-siMM).

Table 3.3: Preparation and characterisation of **PSsiNPs**. AuNPs were coated with PS-siRNA and polymer (**P1** or **P2**) by titration of NaCl over 3 h. The siRNA sequences used to prepare **PSsiNPs** were PS-siRE or PS-siMM. [a]Determined by DLS measuments. [b]Determined by UV-Vis spectrum analysis.

PSsiNPs	Molar ratios AuNP:PS-siRNA:pPEGMA	[$NaCl_{(aq)}$]	[$SDS_{(aq)}$]	NaCl titration time	Size (d.nm)[a]	PDI[a]	λ_{SP}[b] (nm)
PSsiNP.P1	1:350:110	160 mM	0.1 %	3 h	45	0.3	530
PSsiNP.P2	1:350:110	160 mM	0.1 %	3 h	48	0.34	530

The nanoparticles were purified and characterised by DLS and UV-Vis spectroscopy (Figure 3.15). The nanoparticles **PSsiNP.P1** (green line) and **PSsiNP.P2** (blue line) (Figure 3.15 A) showed a significant increase in size after coating. Their average hydrodynamic diameters were 45 nm and 48 nm, respectively. The size histograms showed unimodal distributions with a PdI ~ 0.3 (Figure 3.15 A). The UV-Vis spectra (Figure 3.15 B) showed a red-shift of the SPR band for **PSsiNP.P1** and **PSsiNP.P2**, supporting the increase in particle sizes and suggesting effective coating of AuNPs by polymer and siRNA.

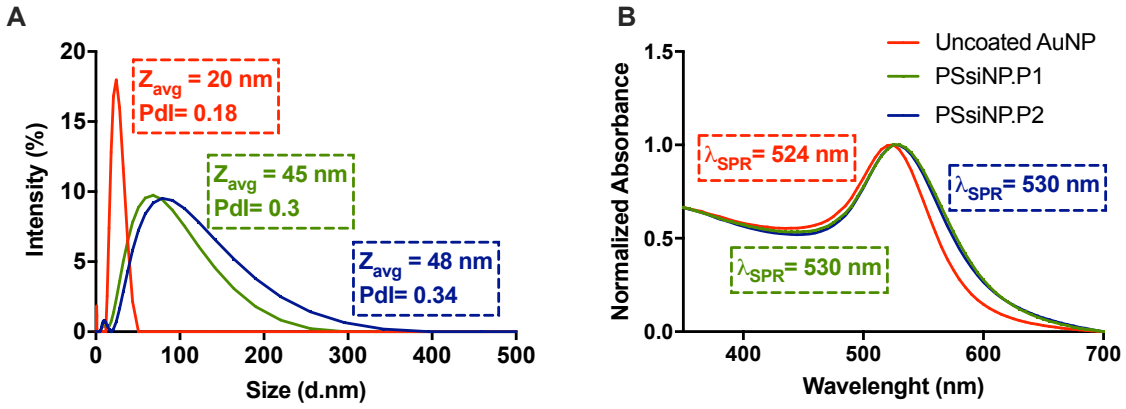

Figure 3.15. Characterisation of AuNPs coated with PS-siRNA and **P1** (green line) or **P2** (blue line). Size distribution histogram by intensity obtained by DLS measurements (A) and UV-Vis spectra of PSsiNPs (B).

The concentration of unloaded PS-siRNA was determined using the QubiT miRNA Assay Kit (Thermofisher). The Qubit microRNA Assay Kit allows easy and accurate quantification of microRNA (miRNA) using the Qubit 3.0 Fluorometer, even in the presence of common contaminants such as salts, free nucleotides, solvents, detergents, and protein. The kit uses a nucleic acid intercalator dye that exhibits green emission when bound to double stranded siRNAs and miRNAs. The nanoparticles were removed from the solution by centrifugation and the supernatants were collected. The concentration of unloaded PS-siRNA was measured, allowing an indirect quantification of the siRNA loading onto AuNPs. The total concentration of siRNA recovered in the supernatants was very similar to the concentration of siRNA used in the loading, indicating that PS-siRNA was not loaded to AuNPs (Figure 3.16).

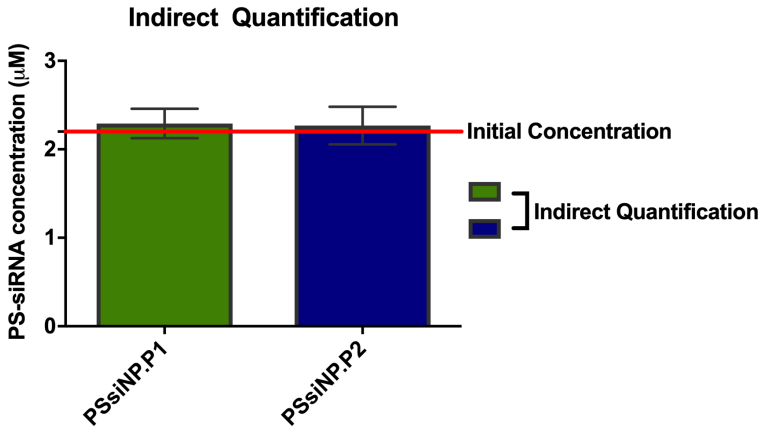

Figure 3.16: Quantification of unloaded PS-siRNA in the supernatants of **PSsiNP.P1** (green bar) and **PSsiNP.P2** (blue bar). Unloaded PS-siRNA was determined using a Qubit miRNA assay kit. The red line represents the initial concentration of PS-siRNA added to PSsiNPs.

To further confirm the low loading of PS-siRNA presented by **PSsiNPs**, gene silencing of *RUNX1/ETO* PS-siRNA (PS-siRE) was evaluated by real-time qPCR. **PSsiNP.P1** and **PSsiNP.P2** containing PS-siRE or PS-siMM were prepared as described in Table 3.3. The nanoparticles were characterised and purified by centrifugation at 15,000 x g for 10 min. PS-siMM was used as a mismatch control sequence for Kasumi-1 cell lines. These cells are a well-studied model for *RUNX1/ETO* translocation in AML,[27] and thus can be used to study the gene knockdown of nanocarriers containing PS-siRE. Kasumi-1 cells were transfected with PSsiNPs containing 100 nM of PS-siRE or PS-siMM and after 48 h gene knockdown was assessed. *RUNX1/ETO* transcript expression was normalised to GAPDH house-keeping gene and the gene silencing compared to non-treated cells (Fig 3.17). There was no significant difference in the gene knockdown of the cells treated with nanoparticles containing PS-siRE and the non-targeting control PS-siMM, indicating that the minor gene silencing observed (~ 10 %) was not related to the delivery of siRE. Moreover, to a nanocarrier be considered successful for the delivery of siRNA the gene knockdown efficiency is expected to be ~ 50 %.[28–30]

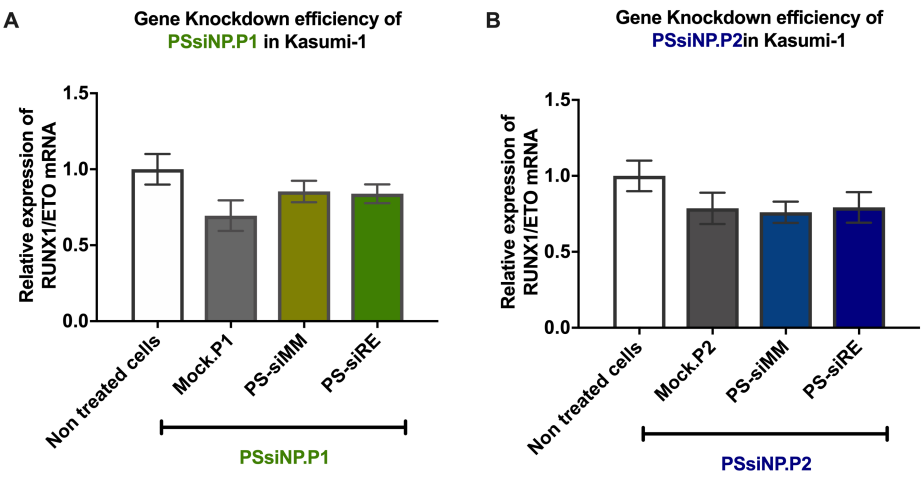

Figure 3.17: *RUNX1/ETO* knockdown in Kasumi-1 cells. Cells were treated with Mock (nanoparticles without siRNA), **PSsiNPs** containing PS-siRE (100 nM) and **PSsiNPs** containing PS-siMM as a mismatch control (100 nM). The graphs show the *RUNX1/ETO* mRNA expression levels after treatment with nanoparticles prepared with **P1** (A) and **P2** (B).

The absence of gene silencing suggests that there was no significant attachment of PS-siRNA to AuNPs, which is in agreement with the loading assay showed in Figure 3.15. The increase in size of AuNPs (Fig. 3.15) suggests the successful coating of AuNPs, however, the quantification of unloaded PS-siRNA and the lack gene silencing (Figure 3.16 and 3.17) indicate that the increase in size is associated only to the

adsorption of pPEGMA onto the AuNP surfaces. These results indicate that the conjugation of double stranded nucleic acids to AuNPs, such as siRNA, does not occur in a similar manner as single strand nucleic acids. The significant loading efficiency observed for PS-ssODN onto AuNPs suggests that the phosphorothioate modification is not the only factor to contribute to the conjugation of AuNPs with nucleic acids.

To attempt to nimprove the loading efficiency of particles prepared with PS-siRNA, the preparation method for **PSsiNP.P2** was modified and the concentration of unloaded PS-siRNA was determined. Table 3.4 shows the modifications on the preparation method regarding molar ratios of components, concentration of surfactant, salt aging concentration and titration time of NaCl. The particles formed are labelled as **PSsiNP.P2** and the letter (**T**) was added to the label followed by the protocol number.

Table 3.4: Modifications in the method for preparation of **PSsiNPs**. AuNPs were coated with PS-siRNA and **P2** varying the molar ratios of components, NaCl and SDS total concentration and time of salt aging method.

PSsiNPs	Molar ratios	$[NaCl_{(aq)}]$	$[SDS_{(aq)}]$	NaCl titration time
PSsiNP.P2-T1 AuNP:PS-siRNA:P2	1:350:110	160 mM	0.1%	12 h
PSsiNP.P2-T2 AuNP:PS-siRNA:P2	1:350:870	160 mM	-	3 h
PSsiNP.P2-T3 AuNP:PS-siRNA:P2	1:350:870	-	-	-

PSsiNP.P2-T1 was prepared using the same molar ratios of components used for the preparation of **PSssNPs** (particles prepared with PS-ssODN). However, the salt aging process was extended to 12 h. NaCl helps to decrease the charge repulsion between AuNPs and siRNA, nevertheless, it needs to be slowly titrated to prevent particle aggregation. After preparation of **PSsiNP.P2-T1**, particles were centrifuged and the supernatant collect for quantification of unloaded PS-siRNA. Figure 3.17 shows that the total concentration of PS-siRNA added to the formulation was recovered in the supernatant, indicating that the loading of PS-siRNA to AuNPs did not occur. Therefore, the prolonged salt aging process did not improve the loading of PS-siRNA.

During the salt aging process, SDS prevents AuNPs aggregation by forming a protective interdigitated bilayer around the gold core.[24,31] The PS-siRNA can penetrate the layer and be adsorbed onto Au, however, the reaction is quite slow.[31] To evaluate the influence of SDS in the loading efficiency of PS-siRNA, **PSsiNP.P2-T2** were

prepared in absence of SDS. In addition, the molar ratio of **P2** to AuNPs was increased to assist in displacing the citrated molecules from AuNPs, decreasing the charge repulsion and providing colloidal stability to the system. A different preparation protocol was also tested without NaCl and SDS (**PSsiNP.P2-T3**). For **PSsiNP.P2-T3**, the only factor contributing to the loading of PS-siRNA to gold is the presence of the polymer that helps displacing the citrate molecules from the AuNPs surface, decreasing the charge repulsion between siRNA and particle. All particles were isolated by centrifugation and the supernatant collected for quantification of unloaded PS-siRNA. Figure 3.18 demonstrate that the total concentration of PS-siRNA added (red bars) to the formulations were recovered in the supernatants (blue bars). These results provide an indirect measurement of the loading efficiency (percentages – Figure 3.18) and indicate that PS-siRNA was not loaded to AuNPs, confirming that the changes to the preparation protocols presented in Table 3.4 did not amend the loading efficiency of **PSsiNPs**.

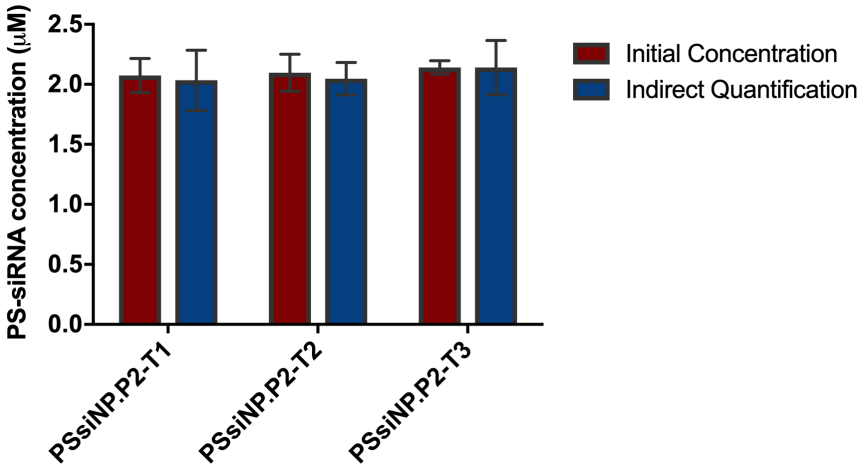

Figure 3.18: Quantification of unloaded PS-siRNA. **PSsiNP.P2** prepared according to the modified protocols presented in **Table 3.4**. Particles were centrifuged and the quantification of unloaded PS-siRNA (blue bars) was measured in the particles supernatant using the Qubit miRNA kit. Considering the initial concentration added (red bars) the loading efficiency (percentages displaced above the blue bars) was calculated.

Results so far indicated that phosphorothioate modification of the siRNA sequence does not result in their conjugation to AuNPs. The phosphorothioate modification, although able to conjugate to gold, presents a lower affinity towards gold. Zhou *et al*.[9] showed the adsorption of thiol, phosphorothioate and non-modified DNA oligonucleotides to 13 nm AuNPs. The DNA sequences used featured a polyA tale on the 5'-end. The PS-modified sequence contained 8 PS-modifications on the polyA block, and thiolated and non-modified sequences were used for comparison. The

conjugates prepared with the thiolated sequence showed higher DNA density on the AuNPs surface, followed by the PS-modified and non-modified sequences. Therefore, it might be possible to improve the loading of phosphorothioate into AuNPs by simply increasing the number of phosphorothioate modifications in the siRNA, which would result in a strong polyvalent interaction with Au. Thus, siRNA modified with 3 phosphorothioates (3PS-siRNA) on the 3' end of the sense strand (Figure 3.19) was conjugated to AuNPs and the loading efficiency was evaluated. The 3PS-siRNA sequence targets the luciferase reporter gene (3PS-siLUC) and is designated in Figure 3.19 B.

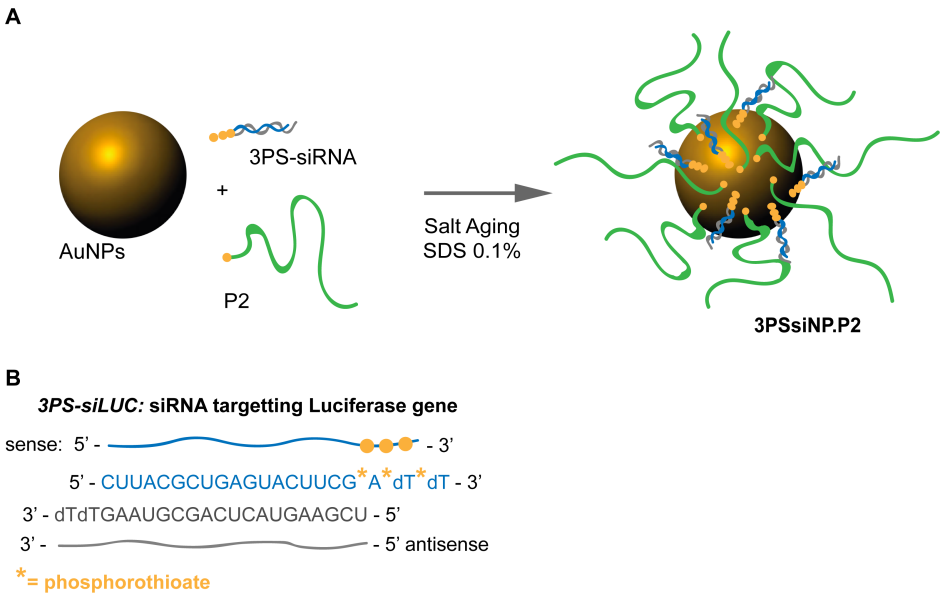

Figure 3.19: Schematic representation of **3PSsiNP.P2**. (A) AuNPs were coated with **P2** and 3PS-siRNA. (B) The 3PS-siRNA sequence used targets the Luciferase gene (3PS-siLUC) and features 3 phosphorothioate modifications on the 3' end of the sense strand.

The firefly luciferase reporter gene assay is commonly used as a tool to study gene expression at the transcriptional level. The assay is based on the enzymatic reaction of luciferin (substrate) by the firefly luciferase enzyme to yield oxyluciferin, generated in an electronically excited state which emits light upon transition to the ground state. Once the luciferase gene is silenced through RNAi therapy, it is possible to determine the gene silencing efficiency by quantifying the luminescence intensity. Consequently, the luciferase reporter assay is an ideal low-cost assay to test a variety of nanomaterials in a short period of time, remaining highly sensitive.[32]

Before conjugation onto AuNPs, it was important to confirm that the multiple phosphorothioate modifications on the siRNA did not lead to unwanted effects on the RNAi mechanism. Therefore, the gene silencing efficacy of 3PS-siLUC was evaluated.

Kasumi-1 cell lines were transduced with pSLIEW resulting in the expression of the firefly luciferase in an AML cell line. The cells were eletroporated with different concentration of 3PS-siLUC and luciferin (Britelite Plus™) was added as a substrate after 24 and 48 h treatment. Cell luminescence was measured to determine the gene knockdown mediated by 3PS-siLUC. As shown in Figure 3.20, modified siRNA promoted around 70 % of gene knockdown after 24 and 48 h for cells treated with 50 nM of 3PS-siLUC. A dose-response efficiency was observed, especially after 48 h treatment, when increasing the dose of 3PS-siLUC resulted in greater gene silencing. The luciferase reporter assay demonstrates that the modification of siLUC by adding three phosphorothioate moieties to the 3' end of the sense strand did not adversely affect the RNAi mechanism, as the modified siRNA was able to promote gene knockdown of luciferase reporter gene.

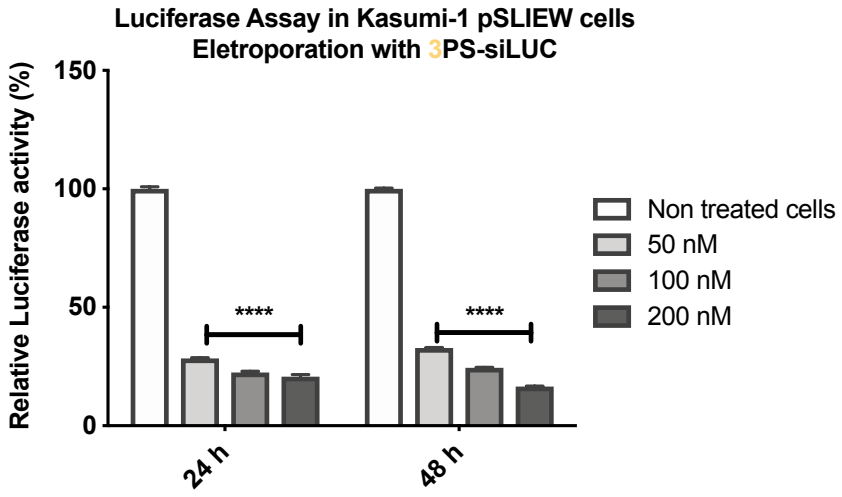

Figure 3.20: Luciferase reporter assay of Kasumi-1 pSLIEW cell line for evaluation of the effect of phosphorothioate sequence modifications in the RNAi mechanism. Cells were eletroporated with 3PS-siLUC at 50, 100 and 200 nM. Luminescence was measured after addition of luciferin and controls were set as 100 %. Results are expressed as mean and SEM (n = 3). ****$p < 0.0001$ when compared to controls.

To conjugate 3PS-siLUC to AuNPs, different protocols were explored (Table 3.5). **3PSsiNP.P2-T1** was prepared using the same conditions as nanoparticles prepared with PS-ssODN (PSssNPs). It is important to have an excess concentration of siRNA in order to promote maximum functionalisation of particles.[9] Thus, **3PSsiNP.P2-T2** was prepared with a larger excess (850 fold) of 3PS-siLUC. In addition, the salt aging final concentration was also increased to try to optimize the loading efficiency of 3PS-siLUC. Particles **3PSsiNP-T3**, **3PSsiNP-T4** and **3PSsiNP-T5** were prepared without pPEGMA. Because of the steric hindrance of **P2**, the

polymer can shield the AuNPs, preventing the siRNA to anchor to the gold surface. **3PSsiNP-T3** was prepared using the salt aging method as previously described. Briefly, the particles were formulated in the presence of SDS (final concentration 0.1 %) and $NaCl_{(aq)}$ (1.4 M) was slowly titrated over a period of 3 h, reaching a final concentration of 0.16 M. **3PSsiNP-T4** and **3PSsiNP-T5** were prepared by adding an excess amount of 3PS-siLUC to AuNPs and heating at 95 °C for 5 min to allow the dehybridisation of siRNA. The particles were allowed to cool to room temperature and the loading efficiency was then evaluated. For **3PSsiNP-T5**, $NaCl_{(aq)}$ (1.4 M) was slowly titrated during cooling. The dehybridisation of siRNA could improve the loading efficiency due to the decrease in the surface charge repulsion. Hybridised siRNA present negative charges due to the phosphate backbone, while dehybridised strands bares the ring nitrogens of the bases. These nitrogens can be protonated at neutral pH, resulting in a less negatively charged molecule. In addition, the exposed bases on the sequence can also conjugate to gold surfaces,[9,33] improving the loading of 3PS-siLUC.

Table 3.5: Methods for preparation of **3PSsiNPs**. AuNPs were coated with 3PS-siLUC and **P2** varying the molar ratios of components, the total salt concentration and surfactant, and the temperature.

3PSsiNPs	Molar ratios AuNP:3PS-siLUC:P2	$[NaCl_{(aq)}]$	$[SDS_{(aq)}]$	Heat
3PSsiNP.P2-T1 AuNP:3PS-siLUC:**P2**	1:350:110	160 mM	0.1 %	
3PSsiNP.P2-T2 AuNP:3PS-siLUC:**P2**	1:850:110	260 mM	0.1 %	
3PSsiNP-T3 AuNP:3PS-siLUC	1:350	160 mM	0.1 %	
3PSsiNP-T4 AuNP:3PS-siLUC	1:350			95 °C for 5 min
3PSsiNP-T5 AuNP:3PS-siLUC	1:350	160 mM	0.1%	95 °C for 5 min

Figure 3.21 shows the concentration of unloaded (indirect quantification) and loaded (direct quantification) 3PS-siLUC for the nanoparticles prepared. The loading efficiency was calculated considering the initial concentration of 3PS-siLUC as 100 % (Chapter 2 – section 2.3.5). For particles prepared with **P2** (**3PSsiNP.P2-T1** and **-T2)** and particles which features only AuNPs and 3PS-siRNA (**3PSsiNP-T3** and **-T4**), the loading of 3PS-siLUC was not observed. The total amount of 3PS-siLUC added to the particles formulation was recovered in the particles supernatants (**3PSsiNP.P2-T1** and **-T2**, **3PSsiNP-T3** and **-T4)** (dark grey bars). Furthermore, when these particles were

treated with DDT (100 mM) to trigger siRNA release, allowing the concentration of loaded 3PS-siLUC to be determined (light grey bars). The results showed only minor concentrations of loaded 3PS-siRNA, confirming the results from the indirect quantification. The loading efficiency calculated for **3PSsiNP.P2-T1**, **-T2** and **3PSsiNP-T3** and **-T4** was < 10 %, indicating that 3PS-siRNA was not successfully loaded to AuNPs (Figure 3.21). For **3PSsiNP-T5**, the concentration of unloaded 3PS-siLUC resulted in a loading efficiency of 29 %. Moreover, a similar loading efficiency was determined when the direct quantification was performed (concentration of loaded 3PS-siLUC) (Figure 3.21).

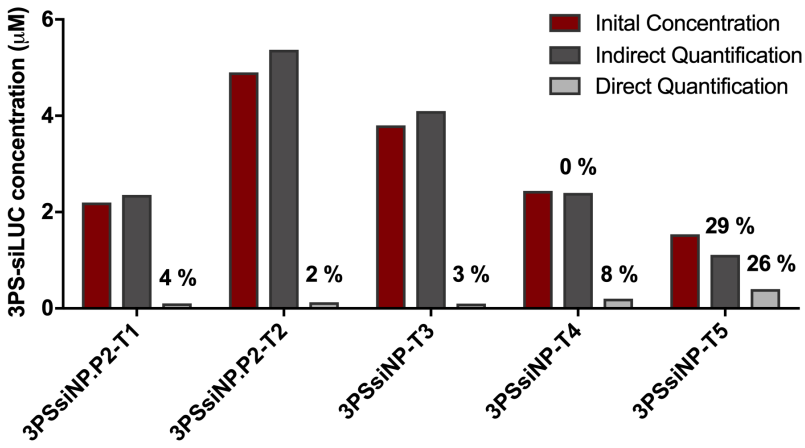

Figure 3.21: Loading efficiency of 3PS.siLUC onto AuNPs. Dark red bars represent the initial concentration added to AuNPs. Dark grey bars show the amount of unloaded 3PS-siLUC and light grey bars show the amount of loaded 3PS-siLUC, as determined after treatment with DDT (100 mM). The loading efficiency was calculate considering the initial amount of siRNA added as 100 % and is presented above the quantification bars.

Although the loading efficiency determined for 3PSsiNP**-T5** was low, the results suggest that dehybridised siRNA (in single strand form) is able to adsorb to AuNPs. The double strand of hybridised siRNAs holds hydrogen bonds between the adjacent bases of the sense and the antisense strand. However, when dehybridised, the single strand presents the ring nitrogens accessible, allowing the bases to participate on adsorption to Au. In addition, particles prepared with dehybridised siRNA without NaCl (**3PSsiNP-T4**) did not show the same loading efficiency, confirming that the salt aging method is necessary for loading nucleic acids to citrate stabilised AuNPs.

The results suggest that PS-siRNA did not conjugate to AuNPs. The modification with three phosphorothioate moieties on the siRNA (3PS-siRNA) did not improve its loading efficiency when compared to siRNA featuring one phosphorothioate modification (PS-siRNA). Nevertheless, when phosphorothioate modified single

strand oligonucleotide (PS-ssODN) was loaded to AuNPs via the salt aging method, a high loading efficiency was determined (**PSssNPs**). **PSssNP.P1** and **PSssNP.P2** were able to load 50 % of PS-ssODN (Figure 3.12). In addition, the prepared particles did not release PS-ssODN in extracellular conditions, however, when in an environment rich in GSH the release of PS-ssODN was observed (Figure 3.13). The significant loading efficiency of **PSssNPs** was initially attributed to the phosphorothioate modification. However, the findings of AuNPs prepared with PS-siRNA suggest that the phosphorothioate modification is not the key factor to contribute to the functionalisation of AuNPs. To further investigate the loading efficiency of PS-ssODN, AuNPs were incubated with **P2** and single strand ODN using the same salt aging method described in section 3.2.3. **PSssNP.P2** was prepared using PS-ssODN. Particles comprising non-modified ssODN (**ssNP.P2**) were also prepared to evaluate the effect, if any, of the phosphorothioate modification in adsorbing to Au surfaces (Figure 3.22).

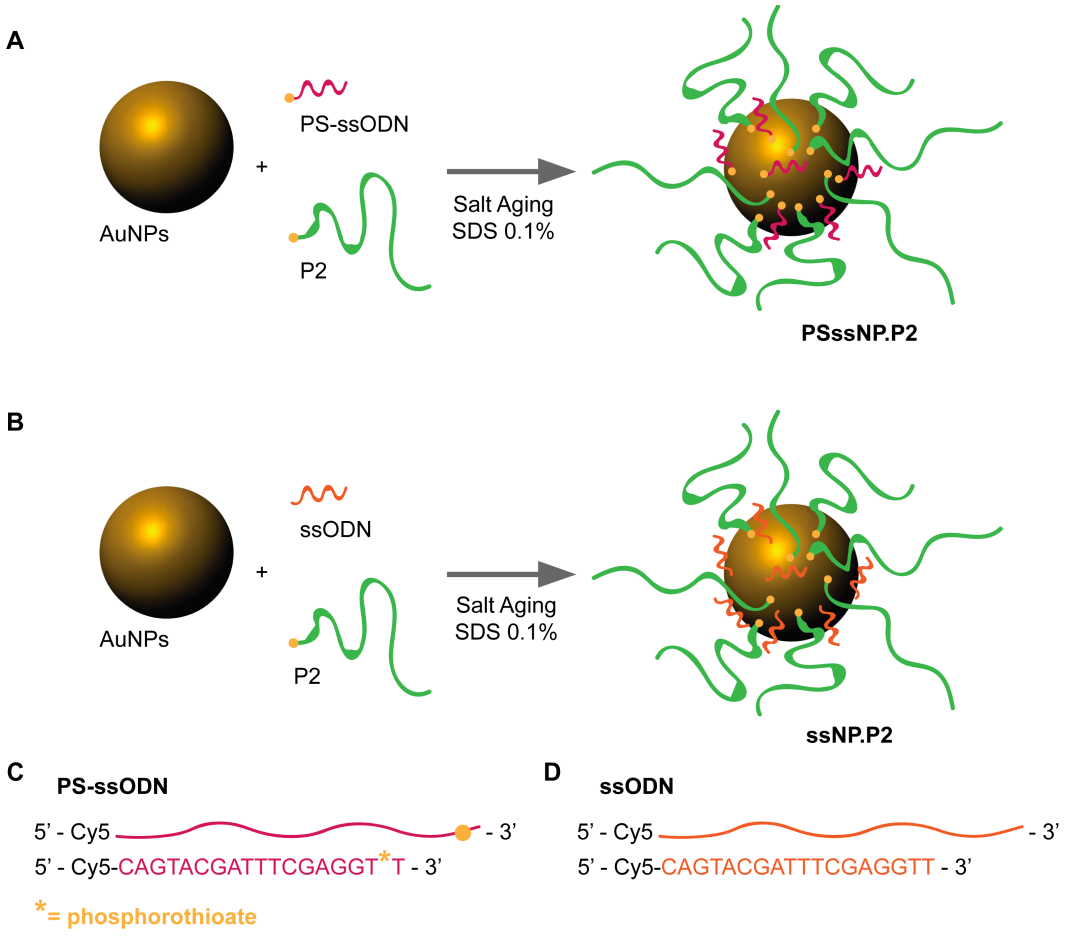

Figure 3.22: Schematic representation of **PSssNP.P2** and **ssNP.P2**. (A) AuNPs were coated with **P2** and PS-ssODN. (B) AuNPs were coated with **P2** and non-modified ssODN. (C) Phosphorothioate modified ssODN (PS-ssODN) and (D) non-modified ssODN (ssODN) sequences.

Particles were characterised and their loading efficiencies evaluated. DLS measurements (Figure 3.23 A) showed an increase in particle size, consisting with the previous findings shown in Figure 3.11 A. The UV-Vis spectrum showed no aggregation bands, with a slight shift in the SPR band (Figure 3.23 B), suggesting the successful coating of AuNPs by **P2** and PS-ssODN (**PSssNP.P2** – light blue line) or ssODN (**ssNP.P2** – orange line).

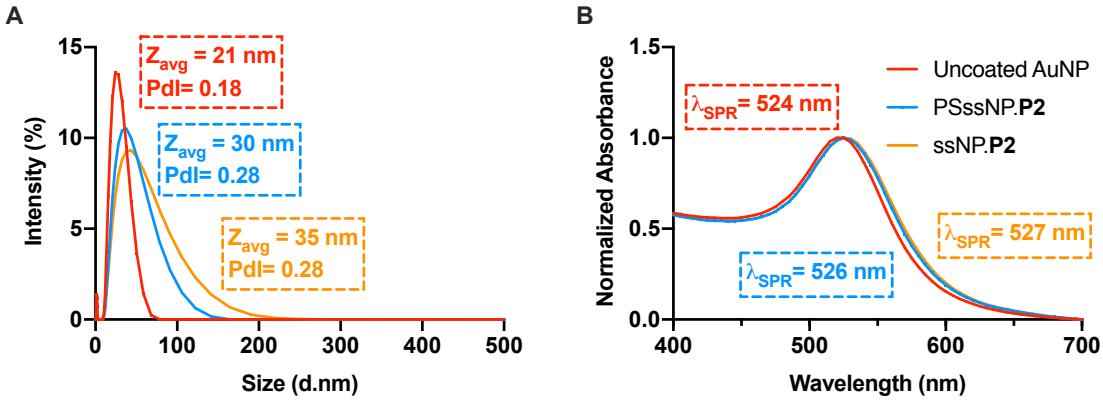

Figure 3.23: Characterisation of nanoparticles prepared with ssODN and PS-ssODN. Particles were prepared with **P2** and characterize by DLS to determine the size and PdI (A) and by UV-Vis (B).

Figure 3.24 shows the amount of unloaded (black bars) and loaded (grey bars) ssODN, allowing an indirect and direct quantification of the loading efficiencies of **PSssNP.P2** and **ssNP.P2**. Particles **PSssNP.P2** showed ~ 50 % of loading efficiency for PS-ssODN, which is in accordance with the previous results shown in Figure 3.11. This result indicates that **PSssNPs** prepared by the salt aging method are reproducible. Moreover, Figure 3.24 shows that there was no significant difference in the loading efficiency of **ssNP.P2** when comparing to **PSssNP.P2**. These results suggest that the phosphorothioate modification in the sense strand of a ssODN plays little role, if any, in conjugation onto AuNPs. The possible explanation could be that the attachment to AuNPs is occurring through the exposed nitrogens of the bases. Kimura-Suda *et al*.[34] demonstrated the chemisorption of single stranded DNA bases onto Au. By FTIR studies, they concluded that the adsorption affinity of each base to Au is A > C ≥ G > T. Thus, it is possible to conclude that the significant loading efficiency showed by PSssNPs is related to the chemisorption of the exposed bases on a single strand oligonucleotide.

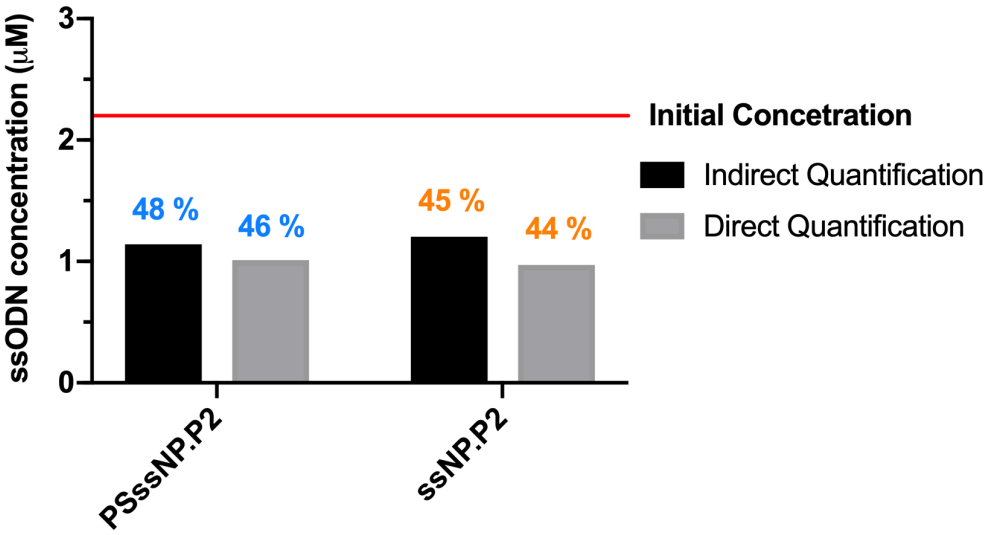

Figure 3.24: Quantification of non-modified ssODN and PS-ssODN in AuNPs coated with pPEGMA. Black bars show the unloaded ssODN and grey bars show the amount of ssODN loaded to AuNPs. Red line represents the ssODN concentration added to the formulations. The initial concentration was set to 100 % and the loading efficiency (%) calculated. The percentages above the quantification bars represent the calculated loading efficiency.

Although the results reported in this chapter suggest that the phosphorothioate modification was not the key anchor for conjugation onto 20 nm AuNPs, it has been used in the literature for functionalisation of Au surfaces. The phosphorothioate modification has been studied for the direct assembly of DNA oligonucleotides to gold surfaces. Through the phosphorothioate modification is possible to control the alignment of AuNPs to form one, two or three-dimensional structures. Jiang *et al.*[35] showed the functionalisation of 13 nm gold nanoparticles with two non-complementary DNA strands (sequence A and B). A third DNA sequence was then added (sequence C), this sequence was complementary to a portion of the grafted sequences, allowing the post-hybridisation of the DNA. By controlling the phosphorothioate modification position and length of sequences A and B, it was possible to control the alignment of AuNPs, forming different architectures that were confirmed by TEM.

Zhou *et al.*[9] showed the functionalisation of 13 nm AuNPs with tandem phosphorothioate modified DNA sequences. The sequences presented a polyA tail where the multiple phosphorothioate modification was introduced. The stability in salt of the conjugates prepared with 1, 2, 4, 6 or 8 phosphorothioate modifications was evaluated. The conjugates that featured 8 PS-modifications showed the higher stability in salt, indicating that the increase in PS-modifications resulted in stronger attachment onto the gold surface. In addition, they also showed the DNA direct assembly of the conjugates. Conjugates were prepared with two different non-

complementary sequences. After addition of the linker sequence, DNA was hybridised, resulting in particle aggregation. The particle aggregation was reversible by heating the conjugates at 75 °C.

These findings show the successful binding of phosphorothioate modified single strand oligonucleotides to AuNPs. It could be possible to improve the conjugation of PS-siRNA onto AuNPs by introducing a polyA tail modified with multiple phosphorothioates in one of the strands of the siRNA. In the RNAi mechanism the guide strand (antisense strand) of the siRNA contains two overhang nucleotides at the 3'-terminus, which is essential for the recognition and binding into the PAZ domain of the AGO2 protein.[36,37] In addition, the 5'-phosphorylated end of the guide sense is also important for the recognition between the MID and PIWI domains onto the AGO2.[38] Therefore, modifications on the guide strand (antisense) of the siRNA might interfere in the RNAi mechanism. The addition of a polyA tail on the passenger strand (sense) of the siRNA could only be possible at the 3'-end, since modifications on the 5'-end would bind to the overhang oligonucleotides on the 3'-end of the guide strand, and interfere in the recognition site by the PAZ domain. A polyA tail modified with phosphorothioate on the 3'-end of the passenger strand could be a promising strategy to improve the loading of siRNA onto AuNPs. However, siRNAs longer than 30 bp are associated with immunological response via the protein kinase R (PKR) pathway, increasing the cytotoxicity of long siRNA strands.[39]

3.3 Conclusions

In this chapter pPEGMA featuring different chain lengths was successfully obtained by RAFT polymerisation. The polymerisation using RAFT chain transfer agent resulted in polymers bearing a dithioester end group that served as an anchor for chemisorption of pPEGMA onto AuNPs. The use of the RAFT chain transfer agent did not require the prior transformation to thiol moieties, as the successful polymer grafting of citrate-stabilised 20 nm AuNPs was achieved by simply incubating AuNPs with pPEGMA aqueous solutions.

Phosphorothioate modified ssODN was successfully loaded to AuNPs, resulting in 50 % of loading efficiency. In addition, particles prepared with PS-ssODN and pPEGMA presented high stability in extracellular *in vitro* conditions. However, when GSH was added to mimic the intracellular environment, the complete displacement and release of PS-ssODN was observed, showing the controlled GSH-response of the nanocarriers.

The phosphorothioate-modified siRNA sequences were not loaded onto AuNPs. The increase in the number of phosphorothioate modifications did not improve the loading efficiency, as the increase in salt concentration or siRNA molar ratios. Nevertheless, PS-ssODN was successfully loaded to AuNPs. When the loading of non-modified ssODN was evaluated, the particles also presented high loading efficiency (~ 50 %), confirming that non-modified ssODN are able to adsorb onto Au surfaces. It was clear that the successful loading of single stranded oligonucleotides is not dependent of the phosphorothioate modification, but mainly, it occurs through the exposed DNA bases that can be adsorbed onto Au. The lack of loading efficiency for PS-siRNA is because in double stranded sequences the bases are forming hydrogen bonds between the complimentary bases and thus, are not exposed for chemisorption onto Au. These observations discourage the use of phosphorothioate modification as anchors for siRNA conjugation onto AuNPs for siRNA delivery platforms.

A possible strategy to load siRNA onto AuNPs is the addition of a polyA tail modified with phosphorothioates on the 3'-end of the passenger strand. However, the addition of a polyA tail could interfere in the recognition of the 5'-end of the guide strand by the AGO2 protein during the RNAi mechanism. Moreover, long strand siRNAs are associated with cytotoxicity mediated by activation of the PKR pathway. Therefore, it would be important to evaluate the RNAi efficiency and cytotoxicity of long strand siRNAs.

3.4 References

1 A. Fire, A. Fire, S. Xu, S. Xu, M. K. Montgomery, M. K. Montgomery, S. A. Kostas, S. A. Kostas, S. E. Driver, S. E. Driver, C. C. Mello and C. C. Mello, *Nature*, 1998, **391**, 806–811.

2 K. A. Whitehead, R. Langer and D. G. Anderson, *Nat. Rev. Drug Discov.*, 2009, **8**, 129–138.

3 R. Kanasty, J. R. Dorkin, A. Vegas and D. Anderson, *Nat. Mater.*, 2013, **12**, 967–977.

4 H. Hinterwirth, S. Kappel, T. Waitz, T. Prohaska, W. Lindner and M. Lämmerhofer, *ACS Nano*, 2013, **7**, 1129–1136.

5 D. S. Seferos, A. E. Prigodich, D. A. Giljohann, P. C. Patel and C. A. Mirkin, *Nano Lett.*, 2009, **9**, 308–311.

6 Y. Ding, Z. Jiang, K. Saha, C. S. Kim, S. T. Kim, R. F. Landis, V. M. Rotello, C. Soo Kim, S. Tae Kim, R. F. Landis and V. M. Rotello, *Mol. Ther.*, 2014, **22**, 1075–1083.

7 C. A. Mirkin, R. L. Letsinger, R. C. Mucic and J. J. Storhoff, *Nature*, 1996, **382**, 607.

8 L. Li, Z. Jin, R. Mirkin C, A. Letsinger R, *Nucleic Acids Res.*, 2002, **30**, 1558–1562.

9 W. Zhou, F. Wang, J. Ding and J. Liu, 2014, **6**, 14795–14800.

10 K. L. Jiménez-Monroy, A. Kick, K. Eersels, B. Van Grinsven, P. Wagner and M. Mertig, *Phys. Status Solidi Appl. Mater. Sci.*, 2013, **210**, 918–925.

11 G. F. Deleavey and M. J. Damha, *Chem. Biol.*, 2012, **19**, 937–954.

12 S. S. Agasti, C. C. You, P. Arumugam and V. M. Rotello, *J. Mater. Chem.*, 2008, **18**, 70–73.

13 X. Xu, J. Wu, S. Liu, P. E. Saw, W. Tao, Y. Li, L. Krygsman, S. Yegnasubramanian, A. M. De Marzo, J. Shi, C. J. Bieberich and O. C. Farokhzad, *Small*, , DOI:10.1002/smll.201802565.

14 J. Suh, K.-L. Choy, S. K. Lai, J. S. Suk, B. C. Tang, S. Prabhu and J. Hanes, *Int. J. Nanomedicine*, 2007, **2**, 735–41.

15 C. Monfardini and F. M. Veronese, *Bioconjug. Chem.*, 1998, 9, 418–450.

16 G. Moad, E. Rizzardo and S. H. Thang, in *Australian Journal of Chemistry*, 2005, vol. 58, pp. 379–410.

17 M. Mazloomi-Rezvani, M. Salami-Kalajahi and H. Roghani-Mamaqani, *J. Phys.*

Chem. Solids, 2018, **123**, 183–190.

18 H. Willcock and R. K. O'Reilly, *Polym. Chem.*, 2010, **1**, 149–157.

19 X. P. Qiu and F. M. Winnik, *Macromol. Rapid Commun.*, 2006, **27**, 1648–1653.

20 A.-S. Duwez, P. Guillet, C. Colard, J.-F. Gohy and C.-A. Fustin, *Macromolecules*, 2006, **39**, 2729–2731.

21 S. Christau, T. Moeller, J. Genzer, R. Koehler and R. Von Klitzing, *Macromolecules*, 2017, **50**, 7333–7343.

22 V. Amendola, R. Pilot, M. Frasconi, O. M. Maragò and M. A. Iatì, *J. Phys. Condens. Matter*, , DOI:10.1088/1361-648X/aa60f3.

23 N. G. Khlebtsov, *Anal. Chem.*, 2008, **80**, 6620–6625.

24 S. J. Hurst, A. K. R. Lytton-Jean and C. A. Mirkin, *Anal. Chem.*, 2006, **78**, 8313–8318.

25 E. T. Land, *Int. J. Radiat. Biol.*, 1990, **58**, 725–725.

26 D. Montero, C. Tachibana, J. Rahr Winther and C. Appenzeller-Herzog, *Redox Biol.*, 2013, **1**, 508–513.

27 A. Ptasinska, S. A. Assi, D. Mannari, S. R. James, D. Williamson, J. Dunne, M. Hoogenkamp, M. Wu, M. Care, H. McNeill, P. Cauchy, M. Cullen, R. M. Tooze, D. G. Tenen, B. D. Young, P. N. Cockerill, D. R. Westhead, O. Heidenreich and C. Bonifer, *Depletion of RUNX1/ETO in t(8;21) AML cells leads to genome-wide changes in chromatin structure and transcription factor binding*, Nature Publishing Group, 2012, vol. 26.

28 F. Pittella, K. Miyata, Y. Maeda, T. Suma, S. Watanabe, Q. Chen, R. J. Christie, K. Osada, N. Nishiyama and K. Kataoka, *J. Control. Release*, 2012, **161**, 868–874.

29 F. Pittella, H. Cabral, Y. Maeda, P. Mi, S. Watanabe, H. Takemoto, H. J. Kim, N. Nishiyama, K. Miyata and K. Kataoka, *J. Control. Release*, 2014, **178**, 18–24.

30 M. Dalmina, F. Pittella, J. A. Sierra, G. R. R. Souza, A. H. Silva, A. A. Pasa and T. B. Creczynski-Pasa, *Mater. Sci. Eng. C*, 2019, **99**, 1182–1190.

31 B. Liu and J. Liu, *Anal. Methods*, 2017, **9**, 2633–2643.

32 M. Ding, L. Bowman and V. Castranova, *Methods Mol. Biol.*, 2012, **906**, 403–414.

33 K. M. Koo, A. A. I. Sina, L. G. Carrascosa, M. J. A. Shiddiky and M. Trau, *Anal. Methods*, 2015, **7**, 7042–7054.

34 H. Kimura-Suda, D. Y. Petrovykh, M. J. Tarlov and L. J. Whitman, *J. Am. Chem.*

Soc., 2003, **125**, 9014–9015.

35 L. Jiang, H. Zhang, J. Zhuang, B. Yang, W. Yang, T. Li and C. Sun, *Adv. Mater.*, 2005, **17**, 2066–2070.

36 A. Alagia, A. F. Jorge, A. Aviñó, T. F. G. G. Cova, R. Crehuet, S. Grijalvo, A. A. C. C. Pais and R. Eritja, *Chem. Sci.*, 2018, **9**, 2074–2086.

37 J. J. Song, J. Liu, N. H. Tolia, J. Schneiderman, S. K. Smith, R. A. Martienssen, G. J. Hannon and L. Joshua-Tor, *Nat. Struct. Biol.*, 2003, **10**, 1026–1032.

38 L. Lisitskaya, A. A. Aravin and A. Kulbachinskiy, *Nat. Commun.*, 2018, **9**, 1–12.

39 R. J. Fish and E. K. O. Kruithof, *BMC Mol. Biol.*, 2004, **5**, 1–15.

Chapter 4
Towards a new pH-responsive siRNA delivery platform

4.1 Introduction

The development of an optimal siRNA delivery platform is essential for the *in vivo* success of RNAi therapy. The ideal nanocarrier must be able to successfully load siRNA, present long blood circulation time without associated toxicity, be able to effectively cross through biological barriers and show controlled and fast release of siRNA.[1] In particular, once the nanocarriers have reached the target cells/tissues and become internalised by cellular uptake, the fast release and endosomal escape of the siRNA into the cytoplasm is necessary to prevent its degradation in the late endosome/lysosome.[2]

There are several approaches to promote fast endosomal escape and siRNA release, including the use of stimuli-responsive nanocarriers, such as pH-responsive nanoparticles. Different approaches have been employed to develop pH-responsive nanocarriers, with one being the incorporation of acid-labile features between the siRNA and the nanocarrier.[3] Acid-labile bonds, for example, can be tuned to display stability at physiological pH yet fast dissociation in the acidic environment of the endosome.[4]

Hydrazones and imines are examples of covalent bonds that can in principal be used for biomedical applications. These bonds can be easily obtained through the reaction of aldehydes with hydrazides or amines, resulting in an equilibrium between the starting materials and their respective products.[5] The equilibrium can be shifted towards the products or in favour of the starting materials by e.g. adding water or changing the pH of the medium (Scheme 4.1). It is also, in principle, possible to control the pH at which hydrolysis occurs by tuning the electronics of the reaction partners.[6]

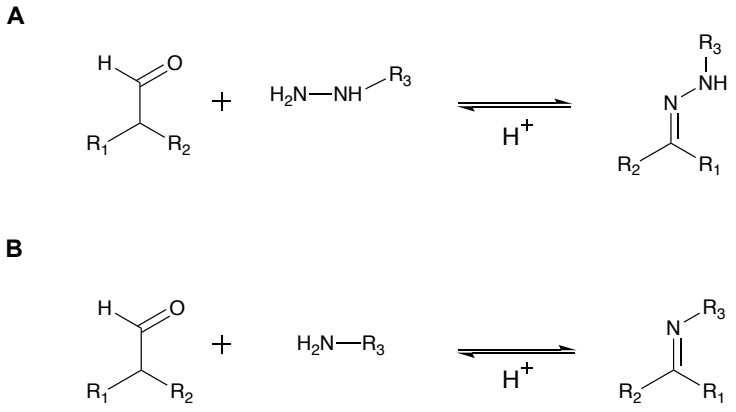

Scheme 4.1: Formation and hydrolysis of (**A**) hydrazones and (**B**) imines in the presence of an acid catalyst.

Hydrazones are compounds with the general formula $R_1R_2C{=}NNHR_3$. They are usually more stable than imines in aqueous conditions because of the mesomeric effect which decreases the electrophilicity of the C=N bond (Scheme 4.2).[7] However, they can undergo hydrolysis in the presence of an acid catalyst, and therefore, is a potentially attractive acid-labile candidate for endosomal escape in a siRNA delivery platform.

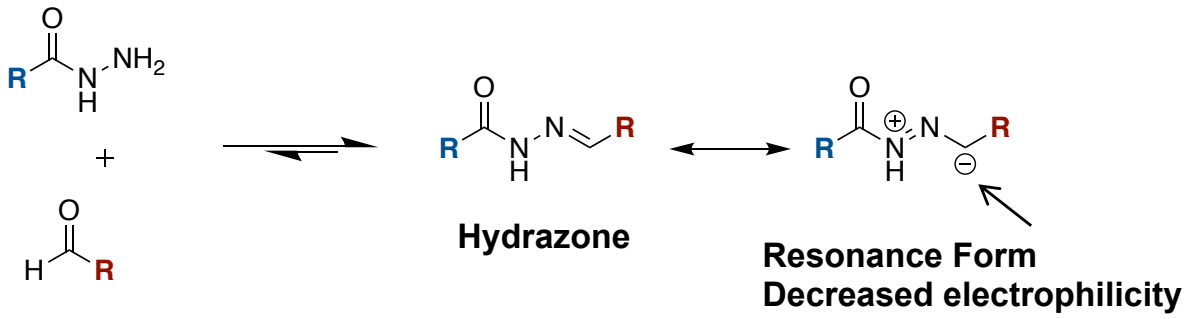

Scheme 4.2: Formation and resonance of hydrazones. Delocalisation of electrons results in the decrease of electrophilicity of the carbon atom of the C=N bond.

Hydrazones have been utilised in drug and siRNA delivery platforms.[8–12] Bae *et al*.[8] reported nanosised polymeric micelles featuring pH-sensitive hydrazone bonds for the intracellular release of doxorubicin, an anticancer drug (Figure 4.1). The micelles were formed by the self-assembly of the amphiphilic block copolymer poly(ethylene glycol)-poly(aspartate hydrazone doxorubicin) (**PEG-p(AspHyd-DOX**)), in which doxorubicin (hydrophobic feature) was appended onto a single block of the polymer through acid-labile hydrazone bonds. The micelles showed controlled pH-sensitivity, as it remained stable at pH 7.0 and released the drug at the intracellular pH (~ 5 – 6). The pH-response was time dependent as the concentration of doxorubicin in the buffer solution was shown to increase over time at acidic pH. The *in vitro* studies showed that micelles were able to cross the cellular membrane and internalise into the cytosol of tumour cells, releasing the loaded cargo. The *in vivo* experiments showed the prolonged blood circulation of the micelles and specific accumulation on the tumour sites. This study showed the potential of hydrazone bonds as pH-sensitive candidates for delivery systems in biomedical applications.

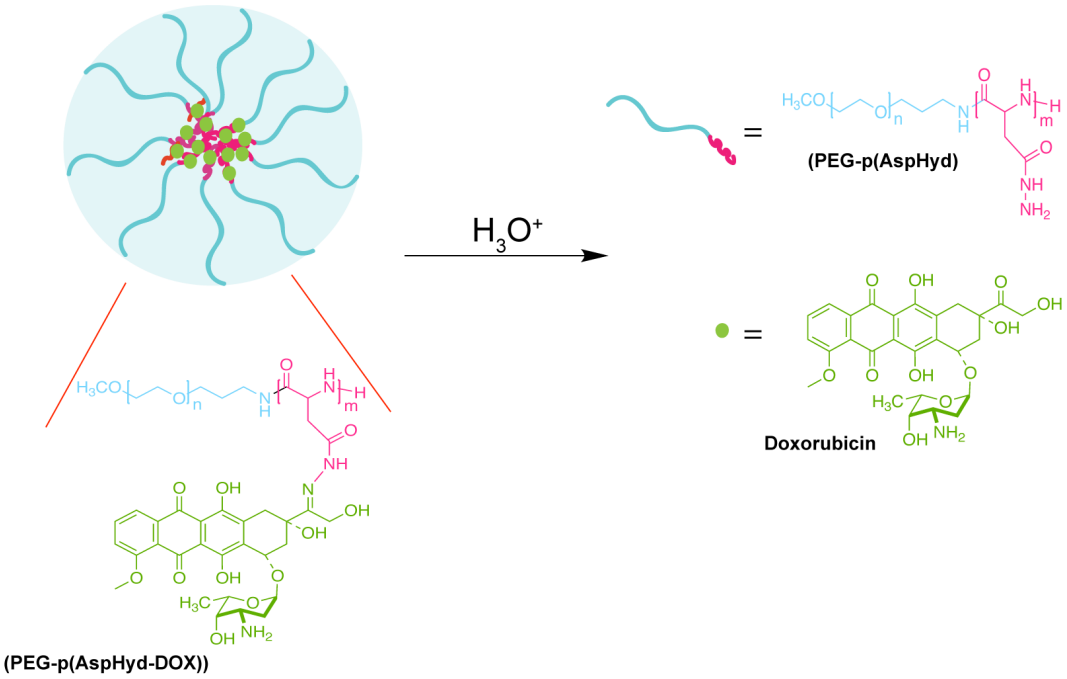

Figure 4.1: Micelles with pH-responsive linkers for the delivery of doxorubicin.[8] Micelles were prepared by the self-assembly of the amphiphilic block copolymer **(PEG-p(AspHyd-DOX))**.

The work from Bouillon *et al*.[4] reported the synthesis of biocompatible acid-labile polymers for siRNA delivery. The group used modified positively charged aminoacids that were condensed with synthetic bisaldehydes (**EG-Ald**) (Figure 4.2). The resulting hydrazone polymer showed effective loading of long strand DNA and siRNA facilitated by the protonation of the nitrogens of the amino acid side chains. The complexes loaded with siRNA showed effective delivery into the cells, resulting in gene knockdown of the luciferase gene, indicating the successful application of this system in siRNA delivery.

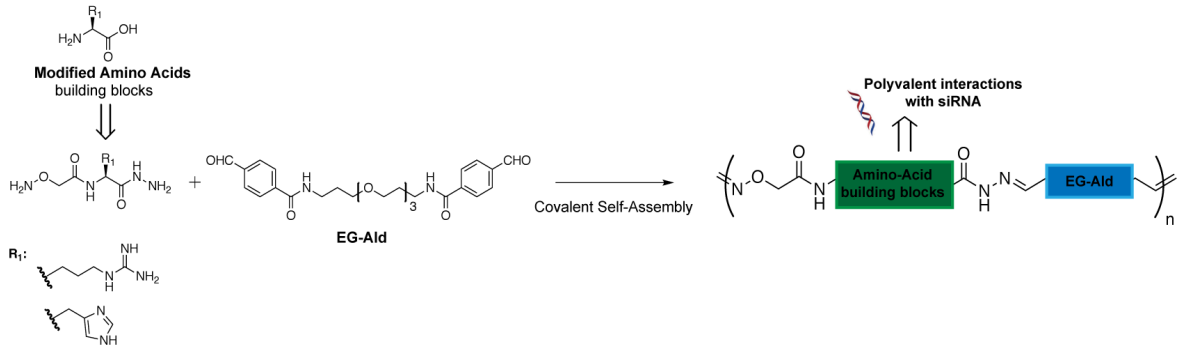

Figure 4.2: Synthesis of acid-labile polymers by condensation of modified amino-acids with synthetic bisaldehydes for siRNA delivery.[4]

Imines have been widely used in chemistry and biological applications since their discovery by Hugo Schiff in 1864,[13] presenting the general formula $R_1R_2C{=}NR_3$. The

equilibrium of the condensation reaction (Figure 4.1 B) can be influenced by external factors, such as temperature, pH and concentration of the reaction partners (aldehyde and amines).[5] Although much is known about imine bonds, it was surprisingly only very recently that work was done to better understand the pH-sensitivity of imine bonds. Godoy-Alcántar, *et al.*[14] reported in their landmark study in 2005 the structure-stability correlation of imines formed by 25 aldehydes and 13 amines in aqueous conditions. The group evaluated the equilibrium constants and correlated the differences in imine structure with their formation and stability in buffers at different pH. The understanding of the structure-stability correlation provides knowledge for chemical modifications on the reaction partners to form imine bonds with specific pH-sensitivity and thus, the pH-sensitivity can be tuned according to the desired application. The group showed that the pH-sensitivity of the C=N bond depends mostly on the basicity of the amine reaction partner and the difference between the HOMO and LUMO levels of the amine and aldehyde, respectively. They evaluated the condensation of different amines with a single aldehyde and determined the equilibrium constants for each imine product. The experiment demonstrated that when more basic amines were used for condensation, higher values of the equilibrium constants were determined. In addition, they also determined the HOMO energy levels for each amine and discovered that higher HOMO energies resulted in higher constants. However, the correlation between the pK_a and the HOMO energy level was rather poor as weakly basic amines usually presented high HOMO energy values. These results indicate that the correlation between imine formation is not exclusively dependent on a single factor, but that both pK_a and the HOMO energy levels of amines contribute to imine formation. The group also evaluated the correlation between the LUMO energy levels of the aldehydes and the equilibrium constants. The condensation of 13 aldehydes was performed with one amine and the equilibrium constants were determined. The results showed that when aldehydes presenting lower LUMO energies were used for condensation, higher equilibrium constants were observed. The correlation between the equilibrium constants and the LUMO energy level showed a good level of confidence, and therefore indicated that the aldehyde reaction partner showed an important effect on the formation of imine bonds. In general, this study demonstrates that high values of HOMO energy for amines and low values of LUMO energy for aldehydes favour the covalent contribution to imine formation. Considering that the same factors will influence the pH range over which

imine hydrolysis occurs, this study provides insightful knowledge for modelling the pH-sensitivity of imine bonds.

In biological applications, Wang, *et al.*[15] described the development of tooth-brush type superamphiphiles (Figure 4.3). The superamphiphiles were formed by the condensation reaction of the hydrophilic block copolymer **PEG-*b*-PLKC**, which contains primary amine groups from the **PLKC** block, and **DBA**, a hydrophobic molecule displaying an alkyl chain and a benzaldehyde end group. The polymers assembled into spherical micelles of 70 nm in size at pH 7.4. The group loaded the hydrophobic molecule Nile Red and showed that the micelles disassembled at pH 6.5, a value that is near the extracellular pH of tumour cells, and released the cargo within 20 min. Moreover, when the pH of the medium was again increased to 7.4, a sufficient amount of imine bonds was formed, increasing the amphiphilic property of the system that resulted in micelle formation. The work from Godoy-Alcántar, *et al.*[14] shows that imines hydrolyse over a relatively broad pH range of ~ three units. The relatively sharp nature of the pH response of this system can be explained that although only a fraction of imines were hydrolysed at pH 6.5, there is an increase of the hydrophilicity of the block polymer, and thus, the system lost the required hydrophobicity to remain within the micellar design. This narrow pH-response demonstrates the reversibility of imine bonds and their application as potential candidates for drug delivery.

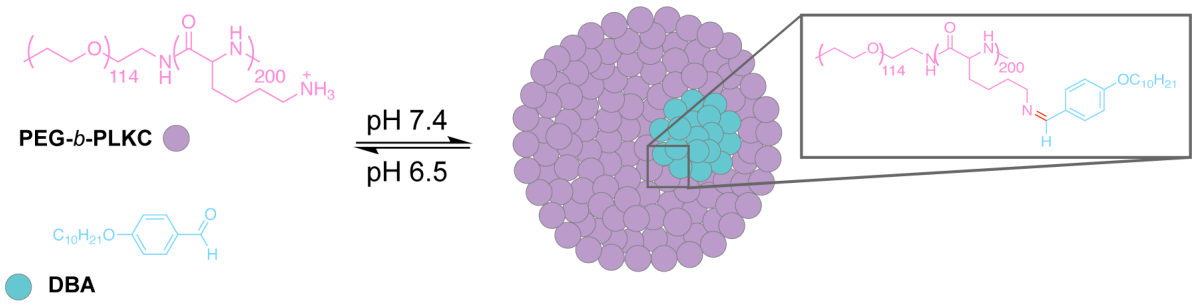

Figure 4.3: Micelle assembly by condensation of hydrophobic aldehyde **DBA** and the hydrophilic block copolymer **PEG-*b*-PLKC**. The resulting amphiphilic block copolymer is able to self-assemble into micelles.[15]

Marin, *et al.*[16] reported the design and characterisation of dendritic dynameric frameworks (Figure 4.4). These systems are composed of reversible covalent bonds used to link a hydrophilic and cationic head with a hydrophobic network building block, forming hydrophobic/hydrophilic dendritic architectures. The hydrophobic **aldehyde JD** is cross-linked via imine bonds with an amine-terminated PEG (**PEG-NH_2**) and **branched-PEI**. Complexation with DNA by the dynameric frameworks showed

particles with a hydrodynamic diameter of 100 nm and high DNA loading capability. The group also evaluated the capability of the frameworks in loading DNA at pH 7.4 by changing the ratios of **PEG-NH_2** and **PEI**. On account of the increased positive charges density, frameworks prepared in the absence of **PEG-NH_2** resulted in higher loading of DNA. The successful loading of DNA at pH 7.4 confirms the presence of cationic charges, and therefore, indicated that the condensation of **PEI** with **JD** to form an imine bond was achieved at pH 7.4. Moreover, the frameworks showed low toxicity and superior transfection efficiency in HEK 293T cells when compared to commercial transfection vectors.

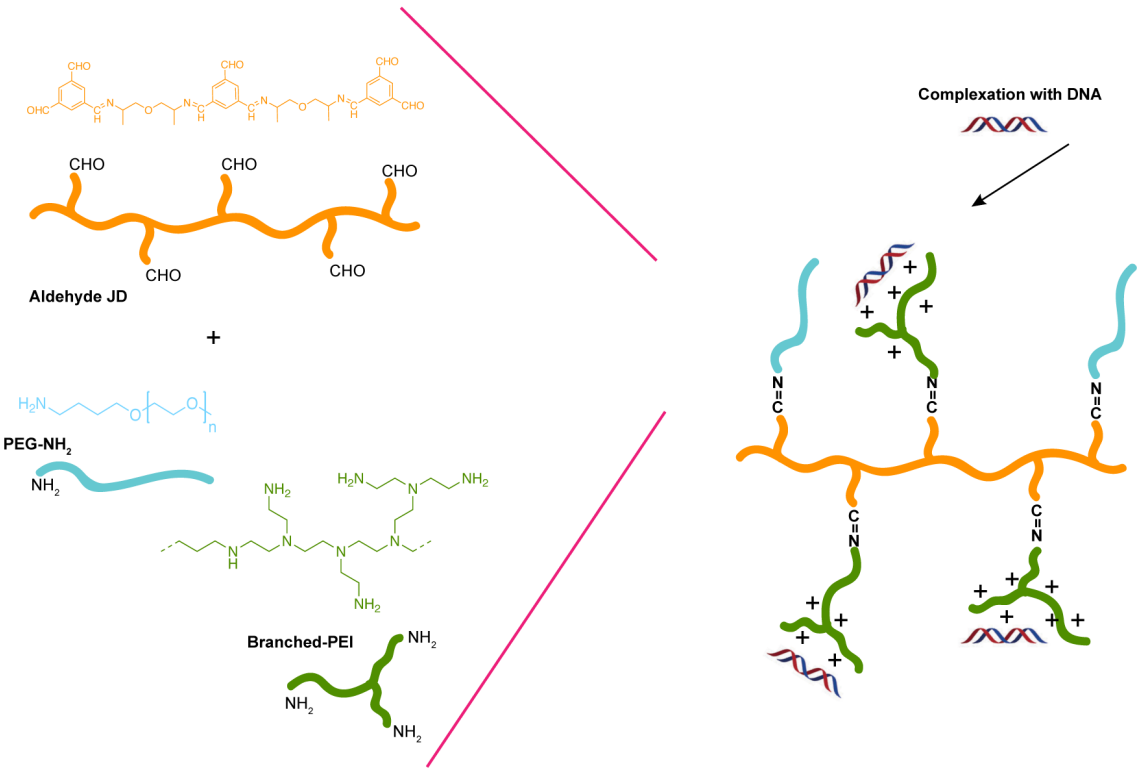

Figure 4.4: Dynameric framework formation by condensation of the hydrophobic **aldehyde JD**, **NH_2-PEG** and **branched PEI**. DNA loading was facilitated by electrostatic interactions of the positive charges of the amino groups of the PEI block with the negative charges of the phosphate groups of the DNA.[16]

The examples described here demonstrate the potential of acid-labile C=N bonds as components within “smart” delivery platforms for the successful development of gene and RNAi therapy. However, the successful *in vivo* delivery of siRNA requires a platform that is capable of performing multiple functions, each at the appropriate step during the delivery process. In this regard, the use of block-copolymers presents a great advantage as components of the delivery platform. By using synthetic block-

copolymers, it is possible to introduce different structures into the nanocarriers, each one being capable to perform a specific function.

In this chapter, the use of a diblock copolymer featuring acid-labile C=N bonds as a new siRNA delivery platform is explored. The ideal delivery platform should present long blood-circulating time after systemic administration, but once internalised into the endosome vesicle, the fast dissociation of the platform and release of siRNA should occur. Therefore, the optimal acid-labile bond should present high stability at pH 7.4 and fast cleavage of the bond at pH ~ 5.0 (pH of the endosome environment). To obtain the appropriate pH-response, different hydrazones and imines were synthesised and their pH hydrolysis was evaluated. The acid-labile bonds presenting appropriate pH-sensitivity for siRNA delivery (stable at pH 7.0 and labile at pH 5.0) were appended on a diblock copolymer. The diblock copolymer is composed of a block of pPEGMA and a cationic block featuring the pH-sensitive bond (imine or hydrazone) (Figure 4.5).

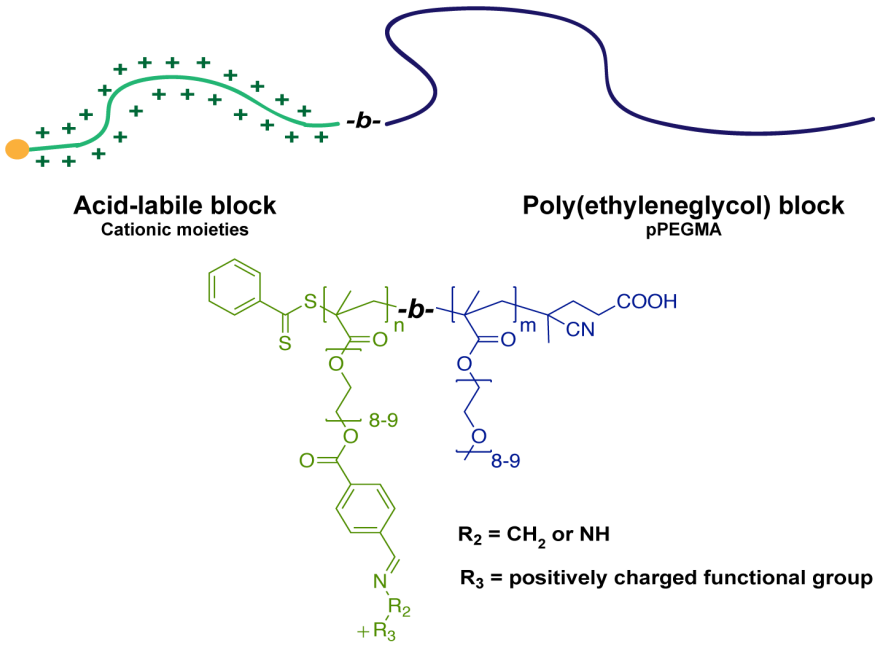

Figure 4.5: Schematic representation of diblock-copolymers for siRNA delivery. The copolymers are composed of a cationic block featuring the acid-labile bonds imine or hydrazones and an ethyleneglycol block.

The pPEGMA block provides colloidal stability and long circulation time in blood vessels. Moreover, pPEGMA can decrease RES uptake due to its hydrophilicity and steric repulsion effects that reduce phagocyte interactions and complement activation.[17] Through the positive charges of the cationic block, siRNA can be loaded via ionic interactions with the negative charges of the phosphate groups in the siRNA

sequence. In addition, the cationic moieties are appended onto the polymer through the condensation of an aldehyde-functionalised scaffold with an amine or hydrazide, resulting in a polymer block featuring acid-labile bonds (Figure 4.5). In this way, the block copolymers can effectively load siRNA and show pH-responsiveness through the imine/hydrazone bonds. Once in the acidic environment of the endosome, the imines or hydrazones would hydrolyse, resulting in endosomal escape and siRNA release. Inspired by the work of Wang, *et al.*,[15] only a fraction of the C=N bonds need to hydrolyse to promote siRNA release. As the hydrolysis occurs, the cationic density of the block copolymer becomes too low for effective complexation of siRNA. Thus, it might be expected that siRNA release can be triggered when not all of the C=N bond are hydrolysed, i.e. a value close to pH ~ 6, avoiding any degradation of siRNA in the late endosome. To obtain a more robust delivery platform, the acid-labile copolymer can be functionalised onto AuNPs through the sulfur-Au chemistry as previously described in Chapter 3. The new multifunctional delivery platform presents a range of properties that results in long blood circulation time, stability at physiological pH, high loading of siRNA and effective endosomal escape and siRNA release (Figure 4.6).

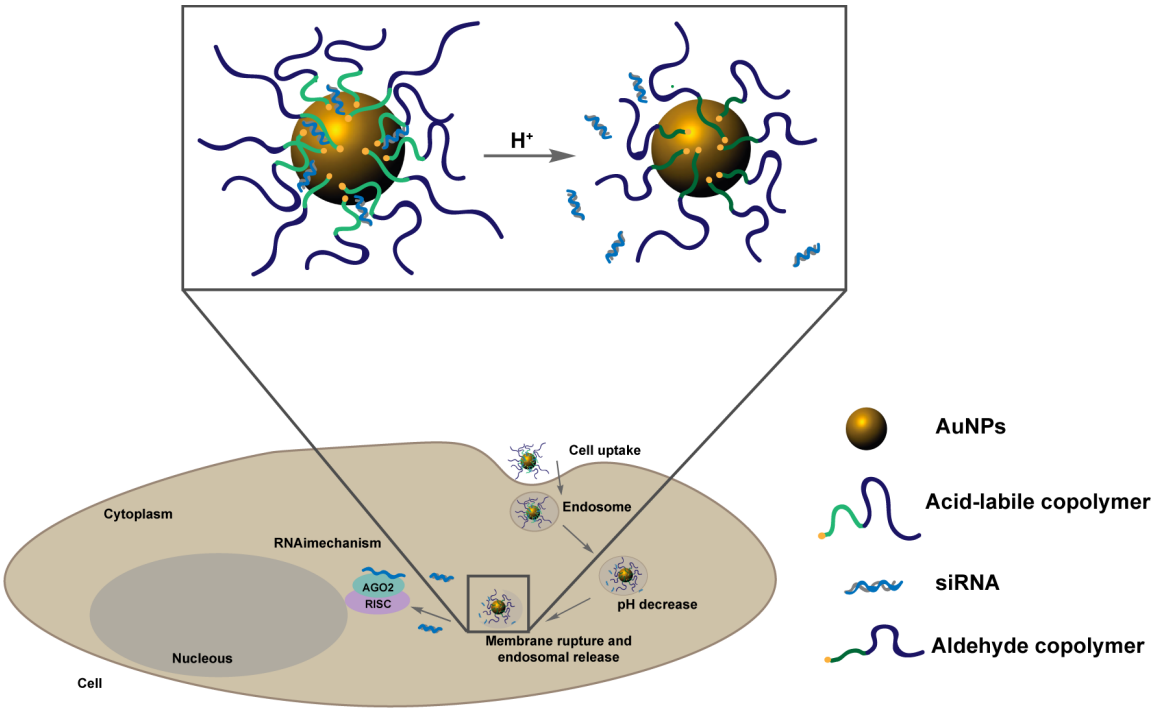

Figure 4.6: pH-response of the nanocarriers constituted of AuNPs and pH-responsive copolymer. The copolymers present a pPEGMA block and a cationic block. The cationic block features hydrazone or imine bonds, that once in acidic conditions is hydrolysed, resulting in the release of siRNA and the conversion to the aldehyde polymer.

4.2 Results and Discussion

In this section, the formation of model hydrazone and imine bonds and their stabilities at different pHs were explored. Aldehyde **A1** (Scheme 4.3 A and B) was synthesised and its condensation with different hydrazides and amines was evaluated. Commercially available aldehydes (Scheme 4.3 C, 4.4. B and C) were also tested. The hydrolysis of each hydrazone/imine was evaluated by ^{1}H NMR spectroscopy and equilibrium positions determined. Considering the biological applications of this work, three molecules were then selected to be appended onto diblock copolymer scaffolds. The copolymer synthesis was conducted by RAFT polymerisation and the polymers were characterised by ^{1}H NMR spectroscopy and GPC. The polymers were then functionalised onto AuNPs and the loading efficiency of siRNA and pH response were evaluated.

4.2.1 Attempts to modify the pH-sensitivity of hydrazone bonds

As outlined in section 4.1, hydrazones are a class of compounds that present higher stability in water compared to imines. Thus, for the purposes of this work, the destabilisation of the hydrazone bond is necessary to obtain appropriate pH-sensitive bonds for siRNA delivery. Three different hydrazones were synthesised (Scheme 4.3) and their stability at different pHs evaluated. Hydrazones **H1** and **H2** (Scheme 4.3 A and B) were prepared from aldehyde **A1** and different hydrazides to explore the effect of different substituents on the hydrazide compounds. Both hydrazones feature positively charged moieties that are essential for eventual complexation with siRNA. Aldehyde **A1** was synthesised by a three-step reaction (Chapter 2 – section 2.5.1) and purified by precipitation as its hexafluorophosphate salt to obtain a white powder. Characterisation by ^{1}H and ^{13}C NMR spectroscopy confirmed that **A1** was successfully obtained (Appendix B). To destabilize the hydrazone bonds, a commercially available aldehyde displaying an electron donating group (EDG) (–OCH_2) was condensed with **HZ1** to form hydrazone **H3** (Scheme 4.3 C). EDGs in proximity to the carbonyl group are anticipated to result in an increase of the aldehyde LUMO level, and therefore reduced strength of the C=N bond.

All hydrazones were synthesised by dissolving the reaction partners (aldehyde and respective hydrazides) in D_2O in a 1:1 molar ratio (20 mM of each compound). The pH was increased to pH = 12.0 with small aliquots of $NaOH_{(aq)}$ (1 M) to favour the formation of hydrazones **H1**, **H2** and **H3** (Scheme 4.3). Then, the pH was slowly decreased by titrating $H_3PO_{4(aq)}$ (1 M) and aliquots were taken to evaluate the position

of the equilibrium by ^{1}H NMR spectroscopy. The yield of hydrazone was determined by the integration of the CH signal of the hydrazone bond at $\delta \sim 8.3$ ppm and compared to the aldehyde signal at $\delta \sim 10.0$ ppm.

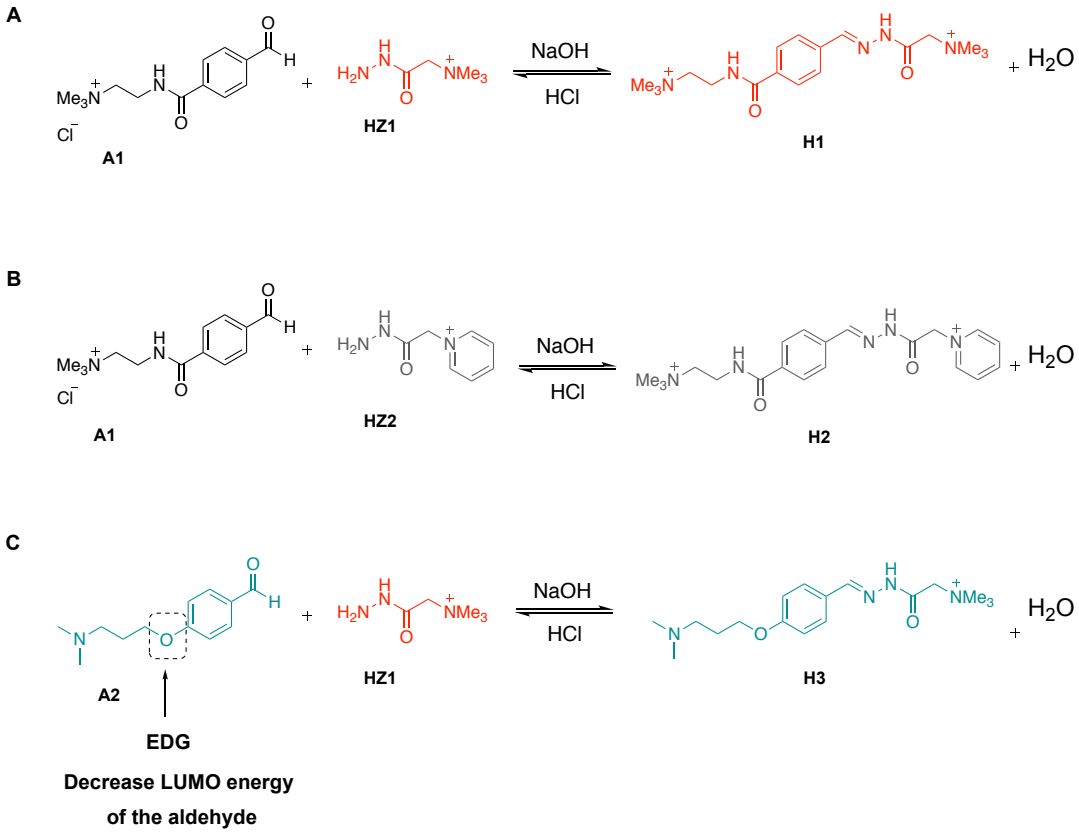

Scheme 4.3: Hydrazone formation by the reaction of aldehyde **A1** with (A) **HZ1** to form hydrazones **H1**, (B) with **HZ2** to form hydrazone **H2**, and (B) aldehyde **A2** to form hydrazone **H3**. The reactions are equilibrium processes and are pH-dependent.

Figure 4.7 shows an example of the ^{1}H NMR spectra of hydrazone **H1** at different pHs. At pH 11, the complete formation of hydrazone was achieved (Figure 4.7 A). At pH 7 and below, the appearance of a second upfield signal at $\delta \sim 8.1$ ppm was observed that is associated with the isomerisation of the C-N bond. At pH 4.0 (Figure 4.7 D) a small signal associated with the aldehyde was observed that became more significant at pH 1.0 (Figure 4.7 E), indicating partial hydrolysis of **H1**. However, even in acidic pH the hydrolysis did not reach completion as the hydrazone signals were still present.

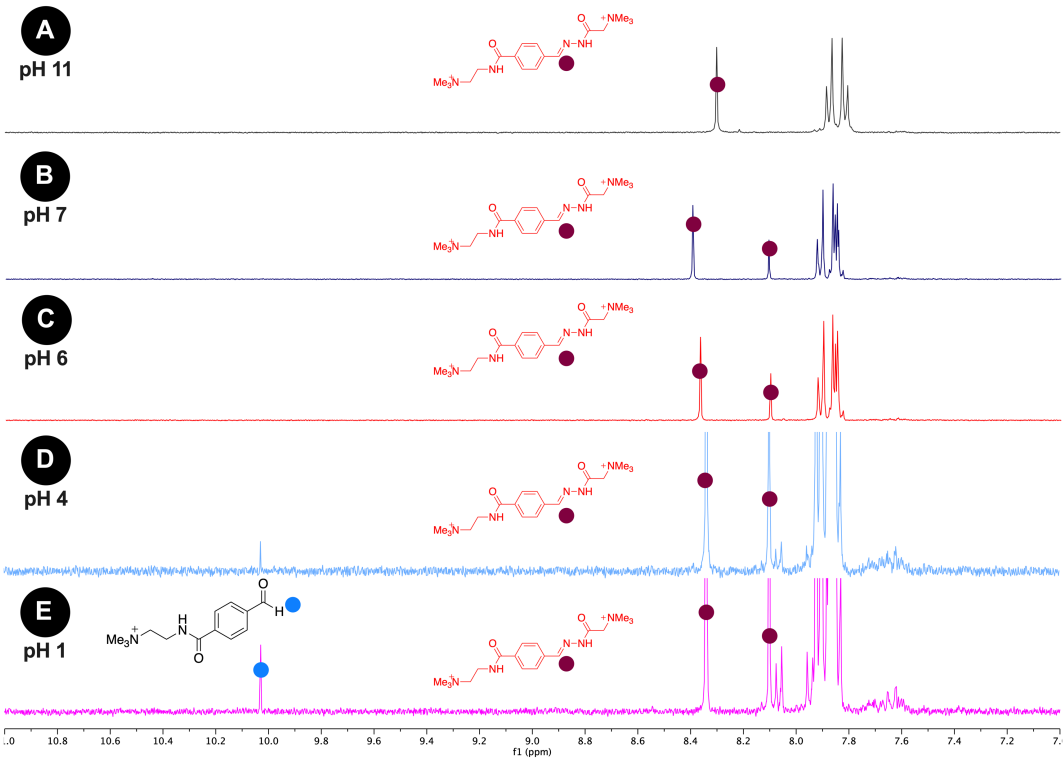

Figure 4.7: Partial ^{1}H NMR spectra (300 MHz, D_2O) of hydrazone **H1** at pH 1.0 – 12.0. **H1** was formed by condensation of aldehyde **A1** with hydrazide **HZ1** at pH 12.0.

The hydrazone yield at different pHs for all hydrazones is shown in Figure 4.8. More than 90 % of hydrazones **H1**, **H2** and **H3** were still present in solution even at pH 1.0, indicating that the EDG modification on the structure of the hydrazone did not make the hydrazone bond more labile at low pH.

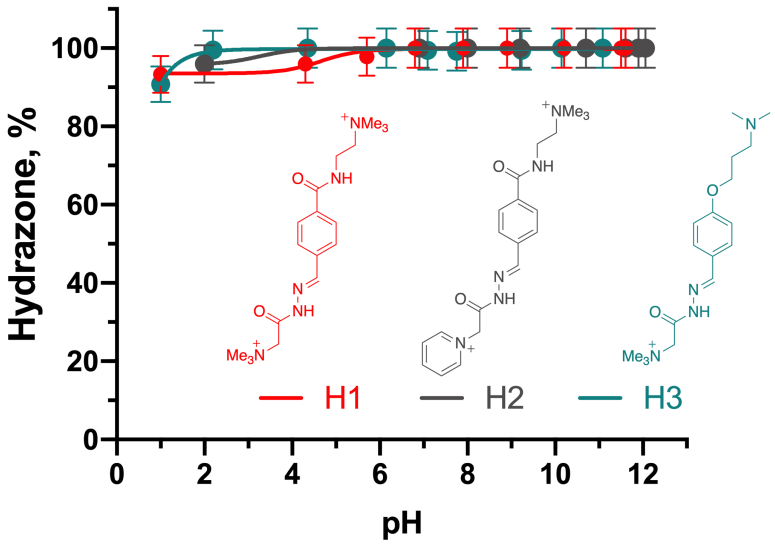

Figure 4.8: Hydrolysis of hydrazones **H1** (red), **H2** (grey) and **H3** (green). Aldehydes were mixed with their respective hydrazide and the pH increased to pH = 12.0. After titration with $H_3PO_{4(aq)}$ (1M), ^{1}H NMR spectra were analysed to determine the yield of hydrazone at different pH values.

It is worthwhile comparing this observation with a literature example. He and co-workers[12] (Figure 4.9) reported the condensation of a hydrophilic polymer (**PEG-NHNH$_2$**) with a aldehyde modified styrene polymer (**PS-CHO**) to form an amphiphilic hydrazone copolymer (Figure 4.9 A). The copolymer self-assembled into spherical nanoparticles of ~ 385 nm in size. The authors claimed that the electron-rich nature of the aromatic aldehyde of **PS-CHO** destabilised the hydrazone bond, allowing its hydrolysis at pH 4.0. This results in disassociation of the hydrophilic corona and decrease of the particle size (Figure 4.9 B). After the pH was again increased to 7.0, the particles were reformed, presenting size and morphology similar to the initial particles. The pH-responsive copolymer reported by He and co-workers contain the same EDG presented in hydrazone **H3**. However, the addition of an EDG on **H3** did not result in destabilisation of the hydrazone bond. The pH-sensitivity demonstrated by He and co-workers could not be reproduced in this work. A possibility explanation could be amphiphilic nature of the polymers synthesized. The pH-sensitivity of the system could be attribute to a partial hydrolysis of the hydrazones, decreasing the hydrophilicity of the system to maintain the micellar form, and therefore, the dissemble of the particles occurred. After the pH is increased, the hydrazone are formed and the system regain its hydrophobicity/hydrophilicity to form spherical micelles.

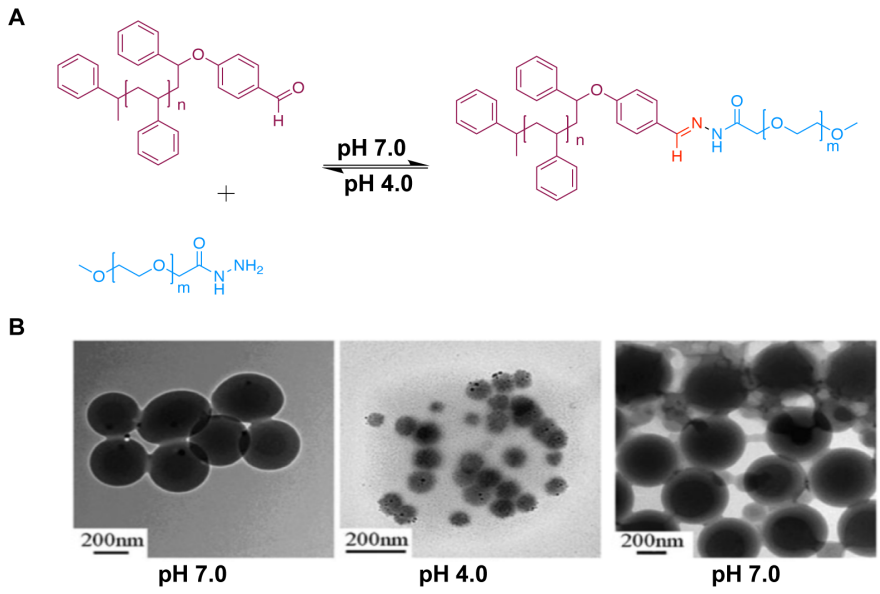

Figure 4.9: Spherical nanoparticles by conjugation of electron-rich aldehyde with hydrophilic modified PEG. The pH-sensitivity was confirmed by the disassemble of the nanoparticles in different pHs by TEM imaging.[12]

The lack of pH-sensitivity of hydrazones **H1**, **H2** and **H3** can be associated with the aromatic structure of the aldehydes. Nguyen, *et al.*[6] evaluated hydrazone

formation and equilibrium constants from an aliphatic and an aromatic aldehyde. They further evaluated the reversibility of these bonds by measuring hydrolysis at pH 6.0. The equilibrium constants determined for aromatic hydrazones were significantly higher when compared to the aliphatic hydrazones, and therefore, aromatic hydrazones showed higher stability at pH 6.0. The electron density of the aromatic ring raises the stability of hydrazones by conjugation with the C=N bond, decreasing its eletrophilicity. The hydrazone bond must present appropriate pH-sensitivity for endosomal release to be considered as a potential candidate for siRNA delivery platforms. Aliphatic hydrazones can be considered as potential candidates for endosomal release, however, on account of its lack of reactivity it is harder to modify its chemical structure. Therefore, it is more challenging to tune the pH-sensitivity of aliphatic hydrazones. Hydrazones **H1**, **H2** and **H3** did not show the desired pH response, and therefore, the evaluation of imine bonds as potential pH-sensitive candidates was assessed.

4.2.2 Attempts to modify the pH-sensitivity of imine

The low stability of imine bonds in water, especially in acidic pH, make this class of covalent bond unfeasible for delivery applications. Thus, enhancing the stability of imine bonds is required to improve its pH-sensitivity, especially towards the acidic environment of the endosome. Godoy-Alcatar and co-workers[14] demonstrated that the pH-sensitivity of imines can be correlated with the pK_a and the HOMO energy levels of the amine reaction partners. Thus, the evaluation of imines formed by the condensation of aldehyde **A1** with amines presenting different basicity was performed (Scheme 4.4 A). Imines **I1-I4** were formed from amines **AM1-AM4**. These amines present different pK_a values and also, after protonation at neutral pH, are able to potentially complex with siRNA due to electrostatic interactions with the negative charges of the siRNA sequence. Amine **AM5** is an arginine-modified compound and was chosen on account of reports describing high complexation and transfection efficiency of siRNA by arginine conjugates.[18,19] Lastly, **AM6** was selected because its methacrylate group presents the possibility to facilitate polymer synthesis by RAFT polymerisation, offering a straightforward route to a pH-sensitive polymer block. The pH-sensitivity of imine bonds can also be tuned by decreasing the LUMO energy levels on the aldehyde reaction partner.[14] The LUMO energy can be decreased by addition of electron withdrawing groups (EWGs) and thus, the effect of different EWGs on the

aldehyde (Scheme 4.4 B and C) was also evaluated using the commercially available **A3** and **A4**.

Imines **I1-I8** were prepared (Scheme 4.4) by the condensation of aldehydes (**A1**, **A3** or **A4**) with amines (**AM1-AM6**) and their stabilities were evaluated at different pH values by ^{1}H NMR spectroscopy. The imines were formed by mixing 1:10 molar equivalence of aldehyde (20 mM in D_2O) and amine (200 mM in D_2O). The pH was then increased to 12.0 by adding small aliquots of $NaOH_{(aq)}$ (1 M) and the ^{1}H NMR spectra evaluated to confirm the complete formation of the imine product (**I1 – I8**). Then, the pH was slowly decreased by titrating $H_3PO_{4(aq)}$ (1 M) and aliquots were collected for evaluation of their imine yields. Tetramethylsilane was used as an internal standard and the diagnostic CH signals from the imine and the aldehyde were used to calculate the imine yield. To illustrate, the ^{1}H NMR spectra obtained for the hydrolysis of imine **I1** are shown in Figure 4.10.

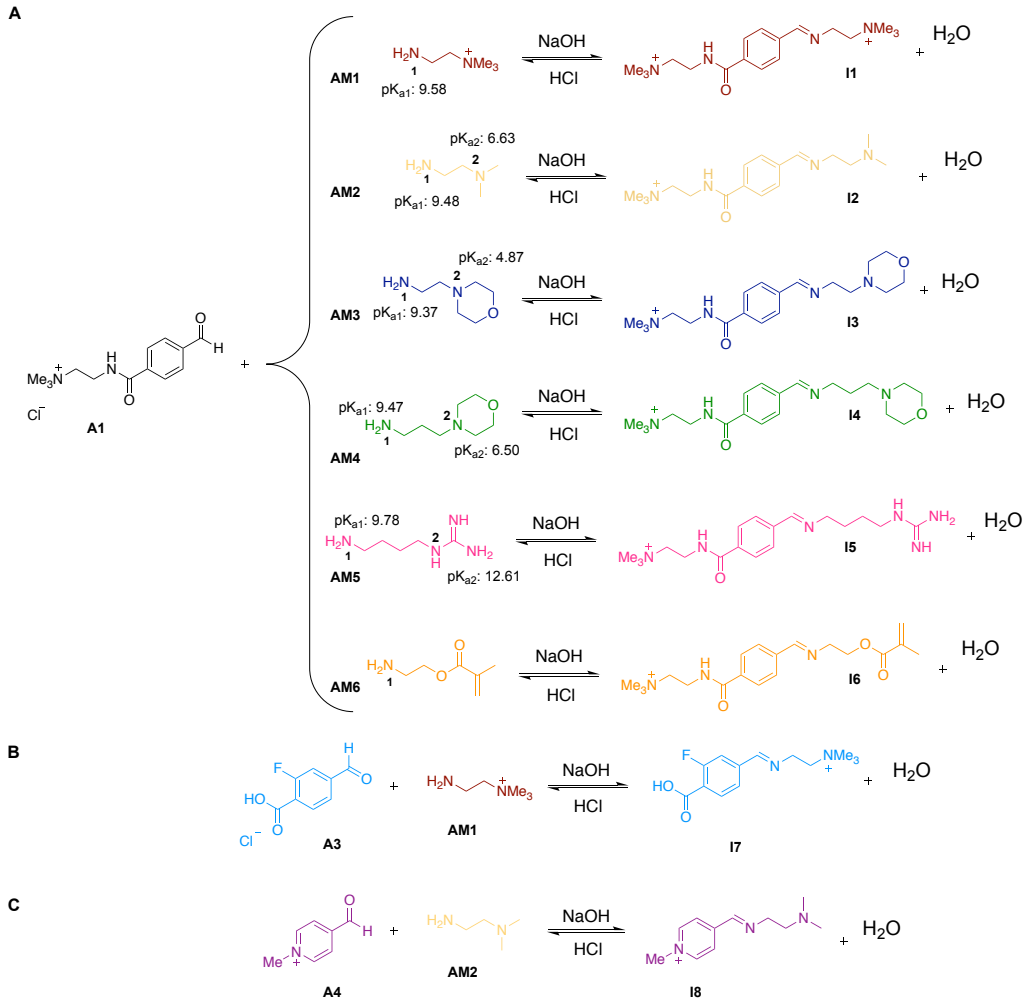

Scheme 4.4: Imine formation by the reaction of (A) aldehyde **A1** to form imines **I1-I6**, (B) aldehyde **A3** to form imine **I7**, and (C) aldehyde **A4** to form imine **I8**. The reaction is a pH-dependent equilibrium process.

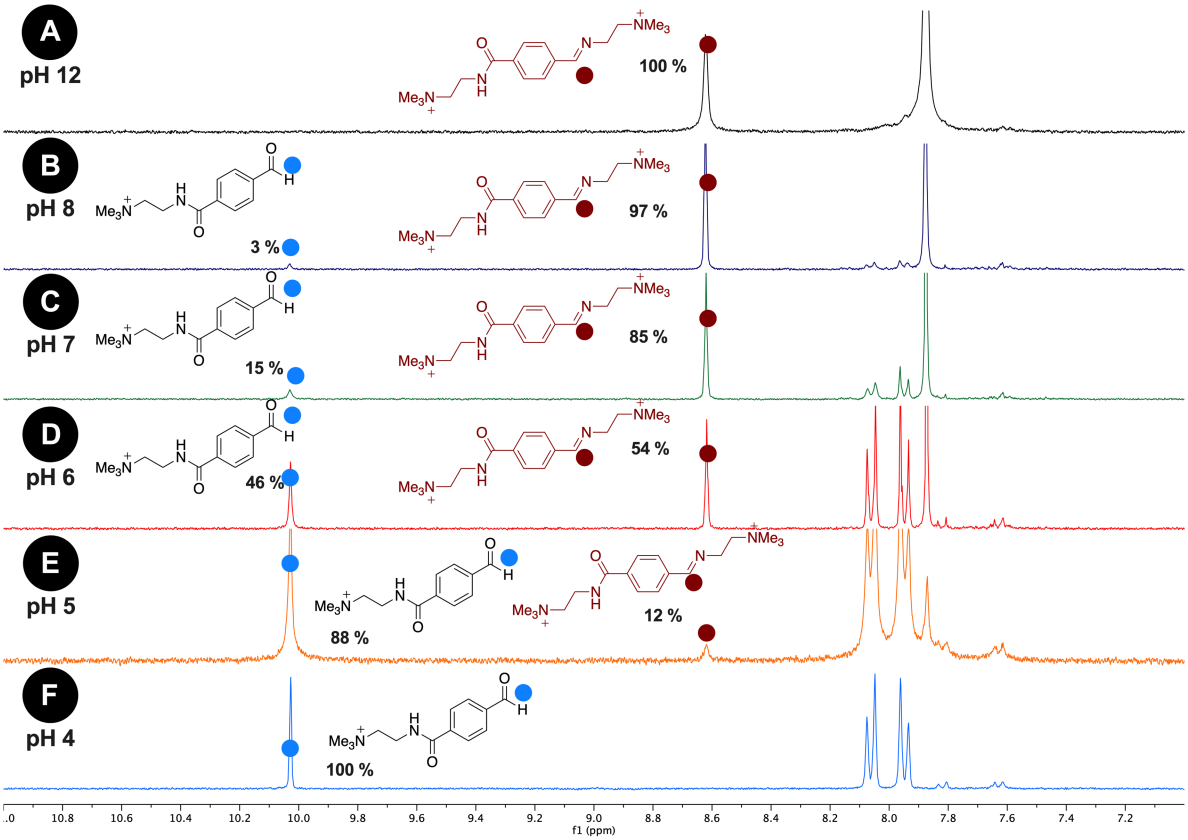

Figure 4.10: Partial ^{1}H NMR spectra (300 MHz, D_2O) of imine **I1** at different pHs. In A to E is shown the hydrolysis of **I1** according to the pH of the medium. (A) Complete formation of **I1** and (F) Complete hydrolysis of **I1**.

The ^{1}H NMR spectrum showed the complete formation of imine **I1** at pH 12 (Figure 4.10 A). Once the pH was ≤ 8.0 the CH signal from the aldehyde **A1** appeared at δ ~ 10.0 ppm, indicating the hydrolysis of **I1**. However, the hydrolysis was only significant bellow pH < 7.0 (Figure 4.10 C). At pH 4.0, no traces of imine **I1** were observed (Figure 4.10 F), confirming 100 % hydrolysis of **I1** in acidic pH.

The pH-sensitivity of all imines (Figure 4.11) was observed by plotting the % imine yield obtained from the ^{1}H NMR spectra against pH value. The “S”-shaped curves obtained demonstrated the expected behaviour of imine hydrolysis, where the position of the equilibrium can be shifted from almost complete imine to reaction partners over about three pH units. The pH value at which significant hydrolysis occurs can be defined as the mid-point of the S-shaped curves.

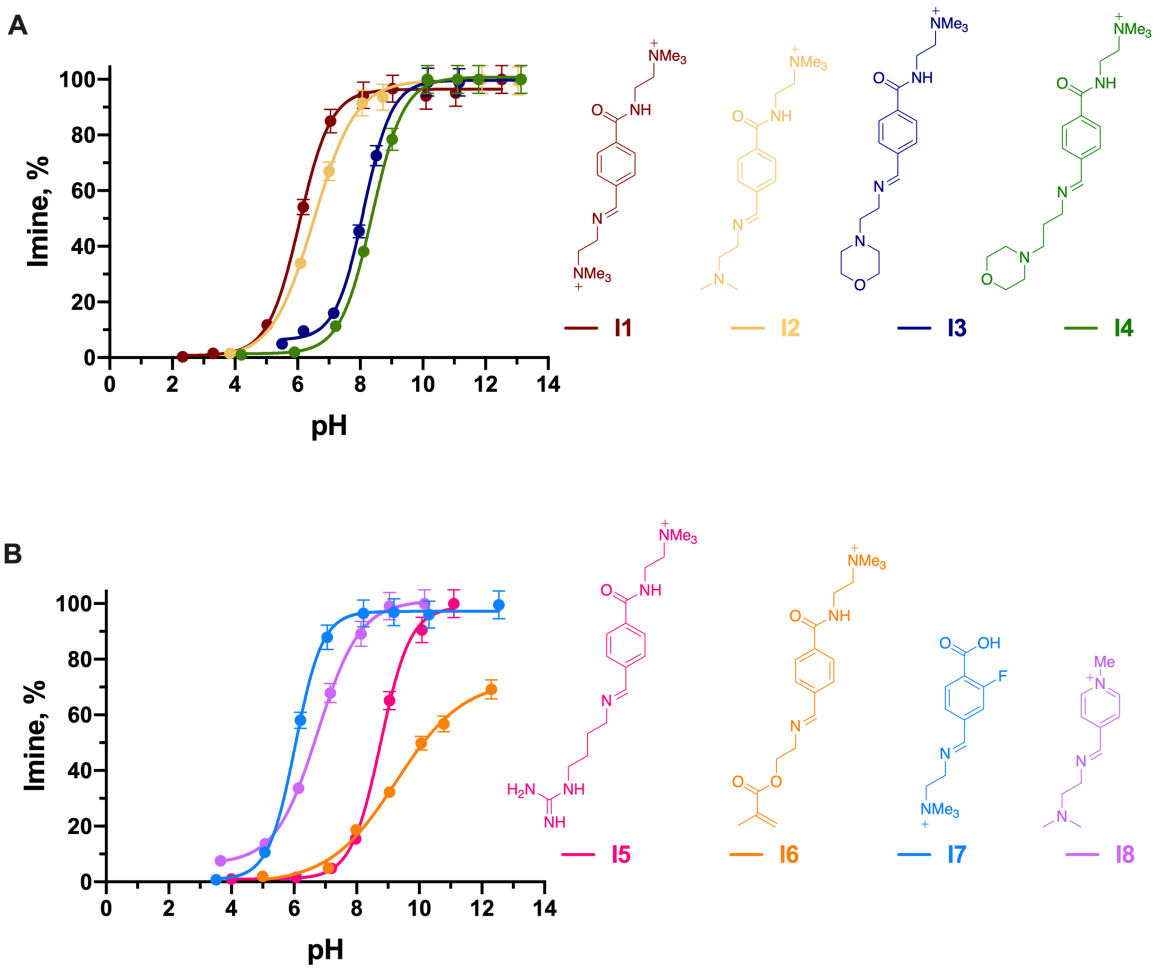

Figure 4.11: Aldehydes were mixed with their respective amines in the molar ratios of 1:10 and the pH increased to pH = 12.0. After titration with $H_3PO_{4(aq)}$ (1M), ^1H NMR spectra were analysed to determine the yield of imines in different pHs. The error bars were determined by considering 5 % of error for the integral values.

The pH sensitivity of imines **I1-I4** is shown in Figure 4.11 A and can be observed that the order of stability is **I1** > **I2** > **I3** > **I4**. Imine **I1** thus showed the higher hydrolytic stability at lower pH values when compared to **I2-I4** (Figure 4.11 A). When analysing the structure-stability relationship of imines **I1-I4**, the only structural difference is the amine reaction partners. Imine **I1** presents an ammonium group (**AM1**) which bears a fixed positive charge. When analysing the difference in the structure of the other amine reaction partners, the order of the pK_a decreased for **I2-I3** (pK_{aAM2} > pK_{aAM3})(Scheme 4.4 A).[20] Although the stability of the imine bonds does not fully correlates with the basicity of the amine reaction partners,[14] Figure 4.11 A showed a correlation between the stability of the C=N bond and the basicity of the amine, where amines presenting higher pK_a showed higher stability in acidic pH. Imine **I4** showed lower stability when compared to imine **I3**. The difference in the structure of these compounds is the distance of the morpholine ring from the imine bond. The morpholine ring in imine **I4**

is further from the C=N bond when compared to imine **I3**, and therefore, presents lesser effect over the stabilisation of the C=N bond. The same effect was observed with imine **I5** (Figure 4.11 B), where the arginine functional group is far too distant from the C=N bond.

Imines **I7** and **I8** showed good stability at pH 7.0 (≥ 50 % imine). **I7** features an electron withdrawing fluoro-substitution on the aromatic ring of the aldehyde that decreases the energy level of the LUMO.[14] The lower LUMO energies contribute towards the strength of the covalent imine bond, resulting in higher stability. Although **I8** showed suitable pH sensitivity for endosomal release (pH 7 > 50 % of imine bonds and pH 5 < 20 % imine bonds) (Figure 4.11 B), the fixed positive charge in the aldehyde is not ideal. When appended onto amine-functionalised polymers and subsequent hydrolysis occurs, the positively charged small molecule will be released from the polymer system. Consequently, the amine functions appended onto the polymer will protonate at low pH, leading to complexation with siRNA and interfere in the siRNA release from the nanocarriers. The same would likely occur with **I6**. In addition, **I6** presented the lowest stability for all imines tested, disregarding its use as pH-sensitive components with a siRNA delivery platform. The screening of pH-sensitivity for different imines identified the imine bonds that can potentially be used as candidates for siRNA delivery applications, and imines **I1** and **I7** were selected as potential candidates and further studies were performed as they display the highest stability at neutral pH.

The pH-sensitivity of C=N bonds is also dependent on the stoichiometry of the reaction partners. In the previous experiments, the hydrolysis was evaluated using 1 equivalent of aldehyde and 10 equivalents of amine. **I1** and **I7** showed ideal pH-sensitivity (stable at pH 7 and hydrolysed at pH 5) in these conditions for siRNA delivery applications. However, when a high excess of one of the reaction partners is used, the position of the equilibrium shifts towards the imine formation. Therefore, the effect of the stoichiometry of the reaction partners in the pH-sensitive hydrolysis was evaluated. **I1** and **I7** were prepared using equimolar equivalents of aldehyde and amine (20 mM). The pH-dependence on the imine yield was calculated and compared with the pH-dependence when using a 10 fold excess of amine (Figure 4.12).

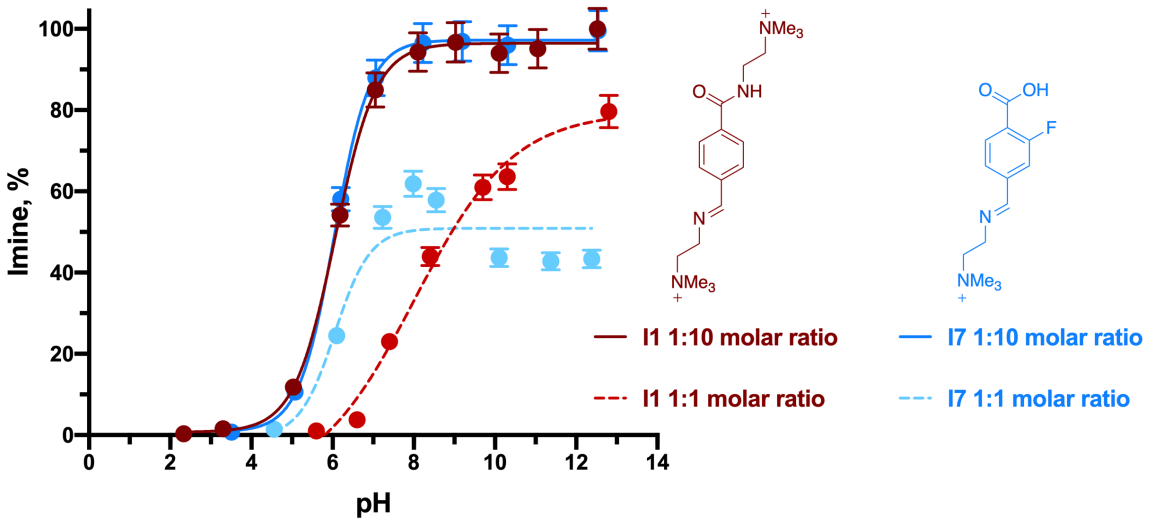

Figure 4.12: Hydrolysis of **I1** (red line) and **I7** (blue line). Aldehydes were mixed with their respective amines in the molar ratios of 1:10 (filled lines) and 1:1 (dashed lines). The pH was increased to pH = 12.0 with $NaOH_{(aq)}$ (1 M) and after titration with $H_3PO_{4(aq)}$ (1 M), ^1H NMR spectra were analysed to determine the yield of imines in different pHs.

With equal stoichiometries of the reaction partners, as anticipated the pH-sensitivity decreased for both **I1** and **I7** (Figure 4.12 – dashed lines). However, even with equimolar ratios of the reaction partners, **I7** showed advantageous pH-sensitivity as at pH 7.0, the imine yield was > 40 %, while at pH < 5.0 was completely hydrolysed (Figure 4.12). These observations demonstrate the ideal pH-sensitivity for systemic administration of siRNA (stable at pH 7.0) and enhanced endosomal release (pH < 6.0).

The pH-sensitivity of model imines was evaluated and the results showed that when an EWG is incorporated to the aldehyde, the resulted imine (**I7)** showed appropriate pH-sensitivity for siRNA delivery applications. Considering that the goal of this project is to append the ideal pH-sensitive imine bond onto copolymer scaffolds, the polymer system might present different pH-sensitivity to the model imine compounds. Thus, the pH-sensitivity of a copolymer scaffold bearing **I1** as an acid-labile bond was evaluated. **I1** was chosen to be appended onto a copolymer scaffold due to the simple and low-cost synthesis, and the aldehyde random copolymer **P3** (M_n: 8 kDa) (Scheme 4.5) was provided by Patrick Higgs who completed its synthesis within a separate project. Copolymer **P3** featured ~ 9 units of aldehyde polymer and ~ 42 units of poly(ethylene glycol) acrylate (PEGA). The copolymer was condensed using equimolar equivalents of aldehyde functions with **AM1** in D_2O to obtain copolymer **P4** (Scheme 4.5). Its pH-sensitivity was then assessed by slowly titrating

$H_3PO_{4(aq)}$ (1 M) and aliquots were collected to allow the evaluation of the imine yield by ^1H NMR spectroscopy.

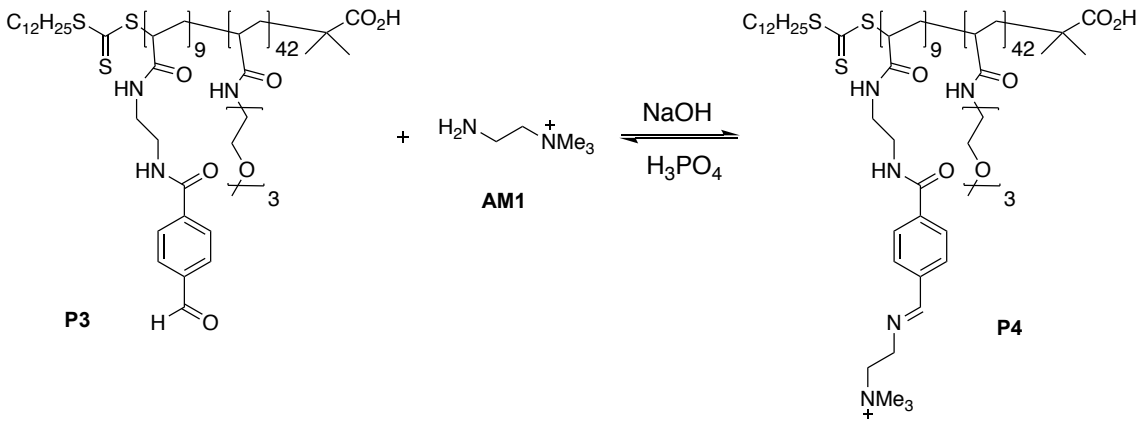

Scheme 4.5:Condensation of aldehyde random copolymer **P3** with **AM1** to obtain imine random copolymer P3.

The pH-sensitivity was compared with the model imine **I1**, showing that in a polymer system the imine yield was higher at pH 7.0 (physiological pH) (~ 30 %) than in the model **I1** (< 10%) (Figure 4.13). This result indicates that in a polymer system the acid-labile bonds might be more stable, and therefore, if **I1** and **I7** are appended onto polymer scaffolds, the resulted copolymer would present excellent pH-sensitivity for siRNA delivery applications, showing high stability at pH 7.0 and hydrolysis at pH 5.0. The higher stability for copolymers could be explained due to the higher density of acid-labile bonds in the system. Moreover, the condensation of the amine **AM1** with the aldehyde copolymer resulted in a lower imine yield when compared to the model compound at basic pH (~ 40 % for **P3** and ~ 80 % for **I1**) (Figure 4.13). The random copolymer features ~ 42 units of PEGA, and only ~ 9 units of the aldehyde polymer. Thus, the hydrophilicity and steric hindrance of PEGA might result in steric impediment of the aldehyde, obstructing **AM1** to attack the carbonyl of the aldehyde. Hence, the synthesis of a copolymer featuring a different architecture of the blocks is necessary to enhance acid-labile bonds formation. In a diblock copolymer architecture it is possible to concentrate the positive charges within one of the blocks. The high density of positive charges allows stronger electrostatic interaction with the multiple negative charges of the siRNA, resulting in higher loading efficiency. For that reason, to obtain polymers able to successfully load siRNA and present acid-labile moieties, the synthesis of diblock copolymer architectures is necessary for the success of the delivery platform.

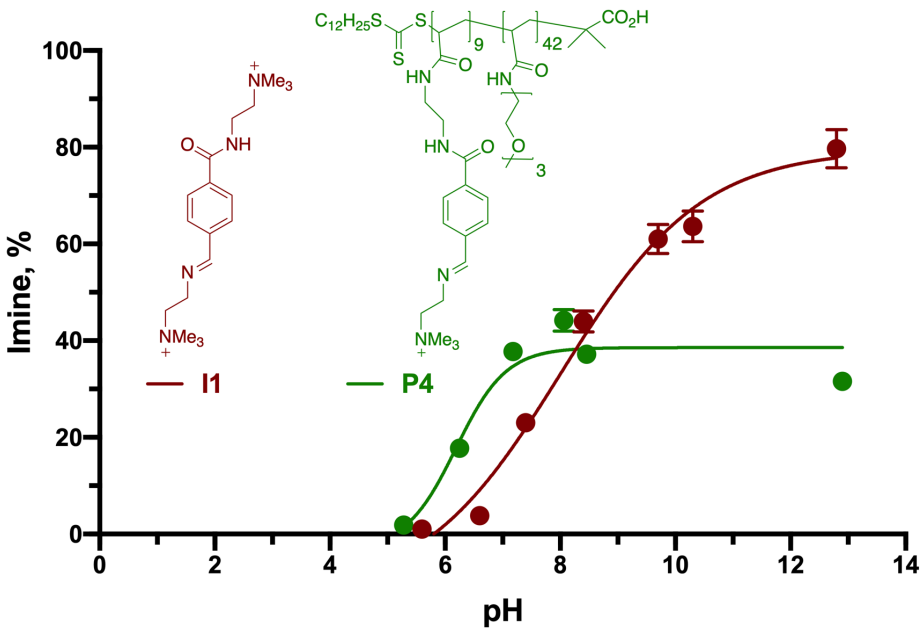

Figure 4.13*:* pH-sensitivity of **I1** (red line) and random copolymer **P4** (green line) in molar ratios of aldehyde:imine 1:1. Aldehyde copolymer **P3** was mixed with **AM1** (20 mM) and the pH was increased to pH = 12.0 with $NaOH_{(aq)}$ (1 M). The pH was slowly decreased by titration with $H_3PO_{4(aq)}$ (1 M) and ^1H NMR spectra were analysed to determine the yield of imines in different pHs.

4.2.3 Synthesis and characterisation of pH-responsive block copolymers by RAFT polymerisation

Polyethylene glycol (PEG) is a highly hydrophilic polymer with very low toxicity that provides colloidal stability and biocompatibility to nanocarriers.[21] PEG chains are often used to prolong the blood circulation of nanocarriers, improving their pharmacokinetics and accumulation into the target tissue. Hence, the use of PEG polymers in this project was deemed essential for the successful delivery of siRNA. The poly(ethylene glycol) methyl ether methacrylate monomer **M2** ($PEGMA_{500}$ M_n: 500 $g.mol^{-1}$) was used for the synthesis of the pH-responsive copolymers (Scheme 4.6). To prepare the pH-responsive diblock, pPEGMA macroCTA **P5** was synthesised by RAFT polymerisation of **M2** using CTPA as chain transfer agent and AIBN as initiator (Scheme 4.6). Then, **P5** was purified by dialysis in MeOH and evaporated to dryness to obtain a pink oil.

Chain extension of macroCTA **P5** (Scheme 4.6) with 2-hydroxyethyl methacrylate monomer **M3** (HEMA M_w: 130.14 $g.mol^{-1}$) was performed in 1,4-dioxane using AIBN as initiator. The polymer pHEMA-*b*-pPEGMA **P6** was dialysed in water and freeze-dried to obtain a pink oil. Block copolymer **P6** was then decorated with aldehydes upon its pHEMA block by its reaction with excess of the acid chloride **1** and then purified by dialysis in MeOH. The decorated copolymer was evaporated to

dryness to obtain **P7** as a pale pink oil. All polymers were characterised by ^{1}H NMR spectroscopy and GPC (Table 4.1).

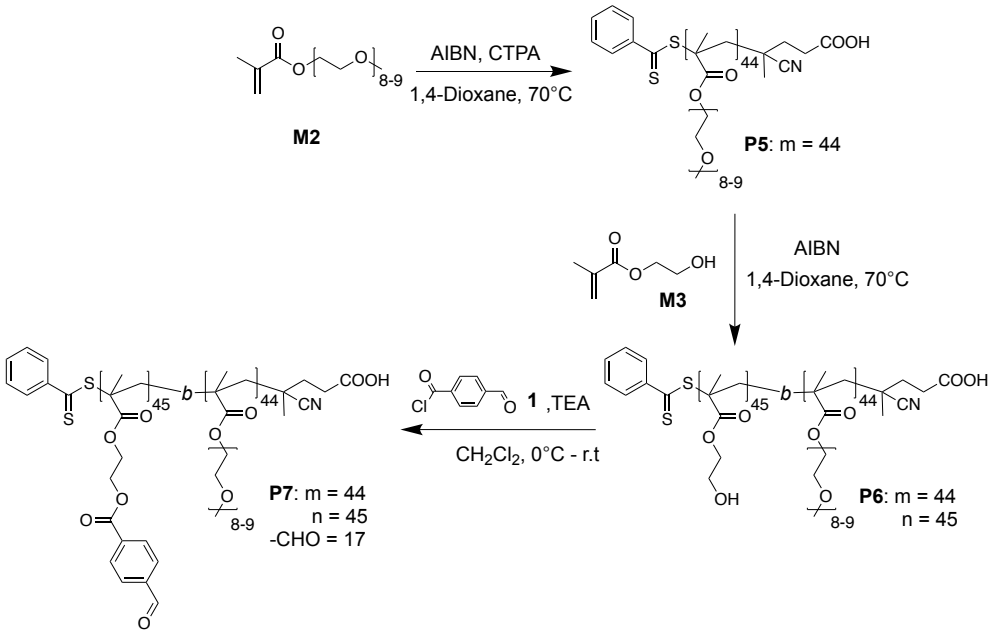

Scheme 4.6: Synthesis of pHEMA$_{(45)}$-b-pPEGMA$_{(44)}$ **(P6)** and its post-functionalisation to obtain an aldehyde copolymer **P7**. PEGMA$_{500}$ monomer **M2** was polymerised to obtain the macroCTA **P5** featuring 44 units of PEGMA. The macroCTA **P5** was extended by reaction with **M3** and the result copolymer **P6** features 44 units of PEGMA and 45 units of HEMA. Reaction with **1** afforded **P6** featuring 17 units of aldehyde.

Table 4.1: Characterisation of **P5, P6** and **P7**. [a] As determined by ^{1}H NMR spectroscopy (300 Hz, $CDCl_3$). [b] As determined by GPC in DMF (0.6 mL min^{-1} with 1g/L LiBr) calibrated against methyl methacrylate standards of very low polydispersity (PDI <1.08).

Polymer	M_n (g/mol)[a]	M_n (g/mol)[b]	M_w (g/mol)[b]	DP	PDI[b]
P5	22,300	8,800	10,600	44	1.21
P6	28,200	13,300	16,500	45	1.24
P7	30,400	-	-		-

The ^{1}H NMR spectra for **P5** (Figure 4.14 A) showed broadened signals, confirming the successful polymerisation of **M2**. The distinctive well-defined signal of the terminal methoxy groups (-OCH_3) of PEGMA side chains was assigned at δ = 3.37 – 3.44 ppm. The signals at δ = 4.05 – 4.30 and at δ = 3.56 – 3.88 correspond to the first methylene protons (-OCH_2) and the remaining methylene (-OCH_2CH_2) of the ethylene glycol side chains, respectively. The signals at δ = 0.69 – 1.21 and δ = 1.64 – 2.15 correspond to the polymer backbone. The signals at δ = 7.52 – 7.85 and δ = 7.91 – 8.08 ppm correspond to the aromatic protons of the polymer end group. These signals were used to estimate the degree of polymerisation (DP) by comparing their

integrals to those of the signals of the terminal methoxy groups and the first methylene of the ethylene glycol chain. For **P5**, the estimated DP = 44 corresponds to M_n ~ 22 kDa. The GPC analysis of **P5** (Figure 4.15 – orange line) showed a monomodal molecular distribution (PDI = 1.21), confirming that pPEGMA can be obtained with good level of control by RAFT polymerisation.

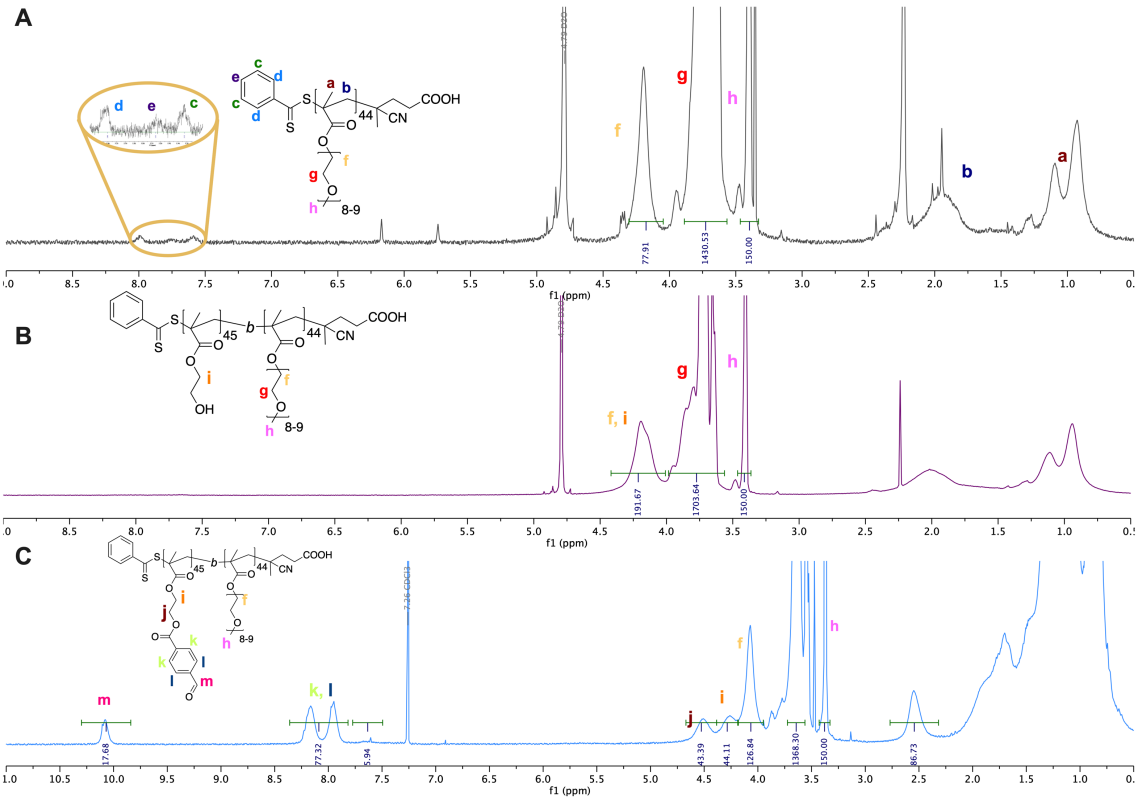

Figure 4.14: Characterisation of **P5**, **P6** and **P7**. ^{1}H NMR spectrum (300 Hz, D_2O or $CDCl_3$) of (A) **P5**, (B) **P6** and (C) **P7**. Diagnostic proton signals are annotated.

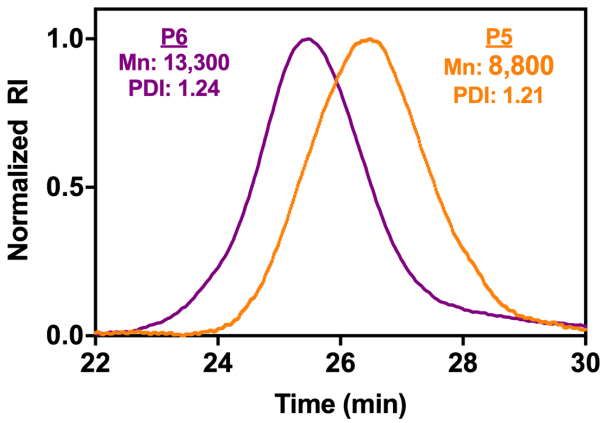

Figure 4.15: Normalised refractive index traces of **P5** (orange line) and **P6** (purple line) obtained by GPC analysis in DMF containing 1g/L of LiBr at 0.6 mL/min. Near monodisperse poly(methyl methacrylate) standards were used for calibration and the average molecular weight (M_n) determined as 8,800 Da for **P5** and 13,300 Da for **P6**.

The ^{1}H NMR spectrum of **P6** (Figure 4.14 B) showed the diagnostic signals previously described for **P5**. The broadening of the signal assigned as **f**, **i** at δ = 4.02 – 4.42 correspond to the overlapped signals of the first methylene within the glycol side chains of **M2** and **M3** (-OCH_2). This signal was used to determine the DP of **M3** by comparing its integral to that of the signal of the terminal methoxy groups of **M2**. The diblock copolymer **P6** presented M_n ~ 28 kDa, featuring an estimated 45 units of HEMA and 44 units of PEGMA. The GPC analysis of **P6** (Figure 4.15 – purple line) showed a shorter retention time when compared to **P5**, confirming an increase in molecular weight. Moreover, **P6** showed monomodal molecular weight distribution, resulting in a very similar PDI when compared to **P5** (PDI = 1.21 and 1.24 for **P5** and **P6**, respectively), indicating the successful and outstanding control of the chain extension of **P5** by RAFT polymerisation.

The ^{1}H NMR spectrum of **P7** (Figure 4.14 C) showed the well-defined signals of the pPEGMA block. The signals of the pHEMA block (**i** and **j**) shifted downfield in the spectrum and were assigned at δ = 3.93 – 4.17 and δ = 4.39 – 4.66. The successful conjugation of aldehyde moieties to the copolymer was confirmed by the broadened signals at δ = 7.81 – 8.35 and δ = 9.82 – 10.28, corresponding to the diagnostic protons of the aromatic ring and the CH proton of the aldehyde, respectively. The aldehyde copolymer **P7** featured an estimated ~ 17 units of aldehyde and final M_n ~ 30 kDa. It was estimated that 38 % of the hydroxyl groups pf **P6** reacted with acid chloride **1** to afford the aldehyde appendages. These results showed the successful synthesis of a diblock copolymer by RAFT polymerisation with an excellent level of control. In addition, the post-functionalisation of pHEMA was possible through one step reaction by a fast and efficient method to obtain diblock copolymers where one of the blocks features aldehyde moieties.

The condensation of **P7** with **HZ1** to obtain a cationic block featuring hydrazone moieties was attempted, however the reaction yield was very low (data not shown). The long side chains of pPEGMA may have sterically shielded the aldehyde groups, impeding their reaction with **HZ1**. Furthermore, short side chains of ethylene glycol such as HEMA display lower critical solution temperatures (LCST).[22] HEMA Polymers presented LCST < 25 °C,[23] resulting in their transition from hydrophilic to hydrophobic with concomitant precipitation when working in temperatures above the LCST. This thermo-response is well-known[24,25] in short chain ethylene glycol based-polymers. Longer polymer side chains of ethylene glycol present much higher LCSTs (e.g > 65 °C)[26] and are thus better suited for application within a delivery platform. Hence, the

synthesis of a diblock copolymer featuring similar lengths of the ethylene glycol side chains within each of the blocks is needed to overcome the LCST challenges and the possible steric hindrance of the aldehyde moieties.

The methacrylate monomer PHEMA **M4** (M_n: 500 g.mol^{-1}) was chosen for chain extension of the macroCTA **P5** (Figure 4.16). PHEMA displays a hydroxyl group at the end of a longer ethylene glycol chain (8-9 ethylene oxide units), and therefore, can evade the steric hindrance of the long PEGMA block. Moreover, PHEMA shows higher LCST (~ 90 °C) when compared to HEMA.[26] To obtain pPHEMA-*b*-pPEGMA (Figure 4.16), **P5** was chain extend with **M4** in 1,4-dioxane using AIBN as initiator (Figure 4.16 A), resulting in 34 % of monomer conversion (Table 4.2). The diblock copolymer **P8** showed shorter retention time by GPC analysis when compared to the macroCTA **P5** (Figure 4.16 A). However, a bimodal molecular weight distribution was observed (PDI = 1.5), indicating a significant degree of uncontrolled polymerisation (optimal PDI for diblock copolymers < 1.2). To improve the molecular weight distribution of pPHEMA-*b*-pPEGMA, the chain extension was performed whilst increasing the molar ratio of AIBN, maintaining 1,4-dioxane as polymerisation solvent to obtain **P9** (Table 4.2).

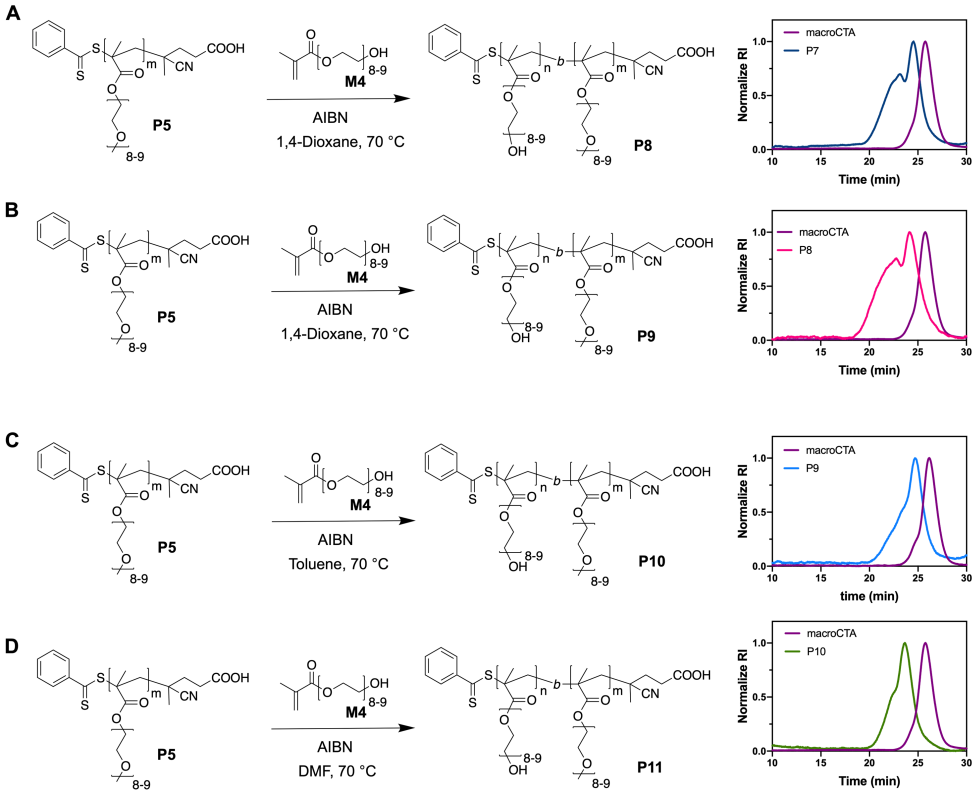

Figure 4.16: Optimisation of the RAFT polymerisation to afford pPHEMA-b-pPEGMA and respective normalised refractive index traces obtained by GPC analysis in DMF containing 1g/L of LiBr at 0.6 mL/min. Near monodisperse poly(methyl methacrylate) standards were used for calibration (PDI <1.08).

Table 4.2: Conditions and characterisation of pPHEMA-*b*-pPEGMA block copolymers prepared by RAFT polymerisation. [a] As determined by ^{1}H NMR spectroscopy (300 Hz, D_2O). [b] As determined by GPC in DMF (0.6 mL min^{-1} with 1g/L LiBr) calibrated against methyl methacrylate standards of very low polydispersity (PDI <1.08).

	P4 macroCTA M_n[b]	M: macroCTA:I	Solvent	Time	Monomer Conversion[a]	M_n[b]	PDI[b]
P8	44,100	100:1:0.3	1,4 - Dioxane	3 h	34 %	97,800	1.50
P9	44,100	100:1:0.5	1,4 - Dioxane	3 h	52 %	110,000	1.74
P10	41,300	100:1:0.5	Toluene	24 h	33 %	81,400	1.36
P11	44,100	100:1:0.5	DMF	3 h	54 %	130,000	1.14

The diblock copolymer **P9** showed higher monomer conversion (52 %) when compared to **P8** (Table 4.2). However, the GPC traces (Figure 4.16 B) revealed a bimodal distribution and increased PDI, showing that the increase in AIBN added did not improve the control of the polymerisation. Therefore, the chain extension was attempted using toluene as polymerisation solvent to obtain **P10** (Figure 4.16 C). The resulting copolymer showed improved GPC traces and PDI when compared to **P8** and **P9** (Table 4.2), however, the monomer conversion was very low (33 %) even after 24h of polymerisation. Thus, the chain extension was performed in DMF, a common solvent for RAFT polymerisation. **P11** (Figure 4.16 D) was obtained after 3 h, resulting in 54 % of monomer conversion and improved PDI = 1.14 (Table 4.2). The GPC traces (Figure 4.16 D) display a small shoulder after chain extension. However, considering the low PDI obtained (< 1.2), it is possible to conclude that the chain extension of the macroCTA **P5** with **M4** in DMF occurred with a reasonable level of control, resulting in a relatively monodisperse diblock copolymer (**P11**) that its adequate for use in the target application.

Copolymer **P11** was characterised by ^{1}H NMR spectroscopy to determine the M_n and DP by integrating the signals of the ethylene glycol side chain of PHEMA and the signal of the terminal methoxy group of PEGMA. The macroCTA **P5** presented M_n ~ 47 kDa, featuring ~ 90 units of PEGMA. The diblock copolymer **P11** presented M_n ~ 72 kDa, suggesting the addition of ~ 50 units of PHEMA.

Copolymer **P11** was then functionalised by its reaction with aldehyde **2** (Scheme 4.7) to obtain the aldehyde copolymer **P12**. The conversion to an aldehyde-functionalised block polymer was confirmed by ^{1}H NMR spectroscopy.

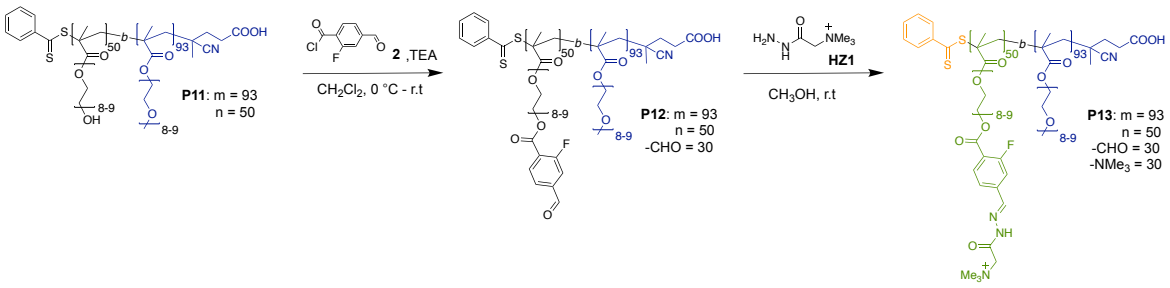

Scheme 4.7: Post-functionalisation of **P11** to obtain pH responsive polymer **P13**. P11 was reacted with the acid chloride **2** to obtain **P12** featuring 30 units of aldehyde. Hydrazide **HZ1** was appended onto the copolymer by condensation to obtain the cationic diblock copolymer **P13**.

The signals at δ = 7.51 – 7.87 and δ = 7.93 – 8.30 (corresponding to the three protons of the aromatic ring) and δ = 9.91 – 10.19 (corresponding to the aldehyde) (Figure 4.17 A) were broadened, suggesting that the aromatic aldehyde was successfully appended onto the copolymer. It was estimated that **P12** presented ~ 30 units of aldehyde, resulting in M_n ~ 76 kDa (Table 4.3).

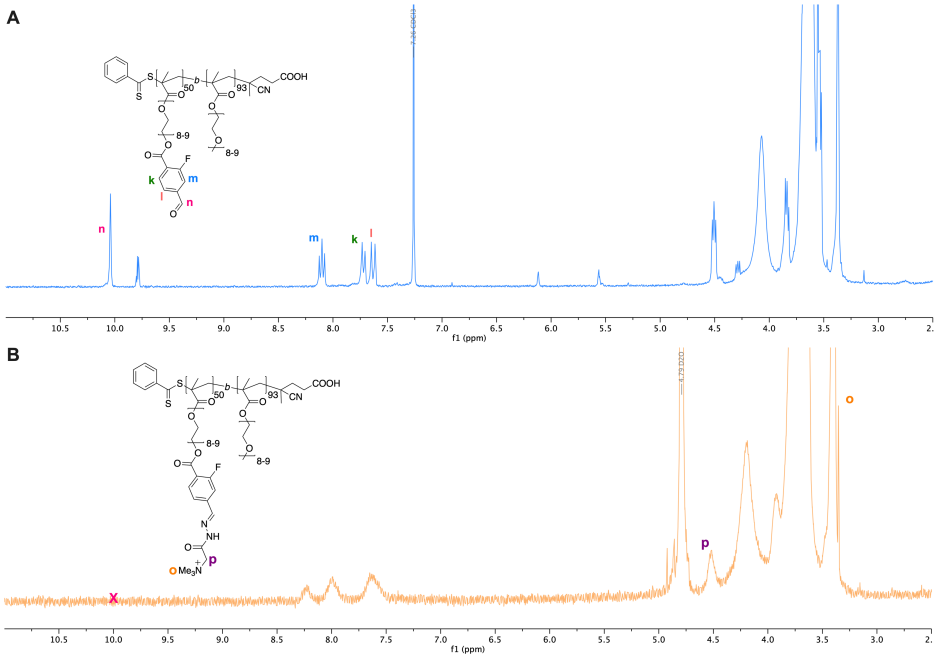

Figure 4.17: ^{1}H NMR spectrum (300 Hz, $CDCl_3$ or D_2O) of (A) P11 and (B) P12. Protons signals are annotated corresponding to diagnostic protons on the polymer. Normalised refractive index traces of (B) P4 and (D) P5 obtained b

P13 was then obtained (Scheme 4.7) after condensation of **P12** with **HZ1** in MeOH. The ^{1}H NMR spectrum pf **P13** (Figure 4.17 B) showed the complete disappearance of the aldehyde signals. The broadening of the signals at the aromatic region arise on account of the overlapping of the CH and the NH signals of the hydrazone bond with the aromatic protons of the aldehyde. The appearance of a signal

at δ = 4.43 – 4.61, corresponding to the -CH_2 protons of the hydrazone (labelled as "p" in Figure 4.17 B) was also observed. Together, these results indicate that **P13** was obtained successfully by a two-step synthesis on pre-formed diblock polymers scaffolds synthesised by RAFT polymerisation.

Table 4.3: Characterisation of macroCTA **P5** and diblock copolymer **P11** and its post-functionalisation to obtain aldehyde functionalised copolymers **P12** and **P14** cationic copolymers **P13** and **P15**. [a] As determined by ^{1}H NMR spectroscopy (300 Hz, D_2O or $CDCl_3$). [b] As determined by GPC in DMF (0.6 mL min^{-1} with 1g/L LiBr) calibrated against methyl methacrylate standards of very low polydispersity (PDI <1.08).

Polymer	M_n (g/mol)[a]	M_n (g/mol)[b]	M_w (g/mol)[b]	PDI[b]
P5	46,800	44,100	49,200	1.12
P11	71,900	130,000	147,600	1.14
P12	76,400	-	-	-
P13	79,800	-	-	-
P14	74,000	-	-	-
P15	75,900	-	-	-

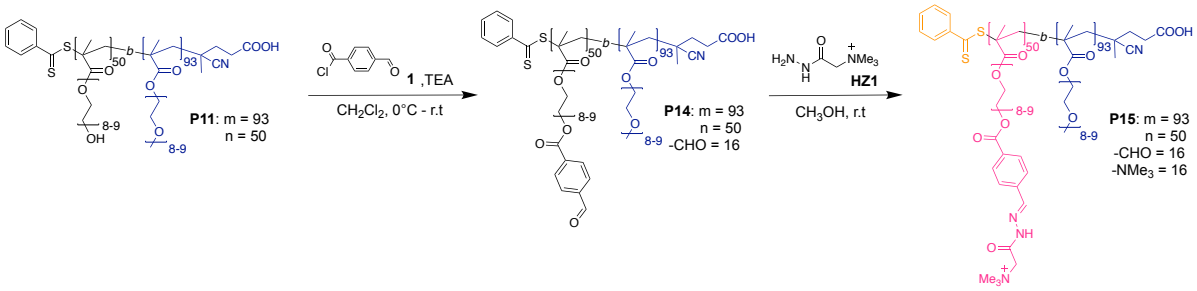

Scheme 4.8: Post-funtionalisation of **P14** and **P15**. **P11** was post-functionalised by its reaction with excess of acid chloride **1** to obtain polymer **P13** featuring ~ 16 aldehyde units. Hydrazide **HZ1** was then appended onto **P13** the polymer to obtain the polycation **P15**.

The same post-functionalisation approach was repeated to obtain copolymers **P14** and **P15** (Scheme 4.8). The aldehyde function in these polymers does not feature the F-substitution on the aromatic ring to allow the evaluation of the effect of the F-substituent on the pH-responsiveness of these polymers. The copolymers were characterised as described previously. The analysis of the ^{1}H NMR spectrum of **P14** (Appendix B) indicates a copolymer featuring an estimated 16 aldehyde units and M_n ~ 74 kDa (Table 4.3). The aldehyde units were fully then functionalised through reaction with **HZ1** to obtain the hydrazone cationic polymer **P15** (Table 4.3). The

cationic copolymers **P13** and **P15** were then used for complexation with siRNA to evaluate the capability of these polymers as delivery platforms.

4.2.4 Preparation and characterisation of polyplexes: Complexation of siRNA with cationic copolymers

Polyplexes between **P13**/**P15** and siRNA were formed based on the electrostatic interactions between two polyelectrolytes of opposite charge (Figure 4.18). The ratio of positive charge (ammonium groups within the polymer) to the negative charge (phosphate groups within siRNA), the so called N/P ratio, determines the loading and stability of the polyplexes formed, and is highly dependent on the composition and the molecular weight of the polymers.[27] In a typical example, a 10 μM solution of siRNA in RNase-free water was mixed with a previously prepared solution of **P13** or **P15** to form **P13siPP** (Figure 4.18 A) and **P15siPP** (Figure 4.18 B).

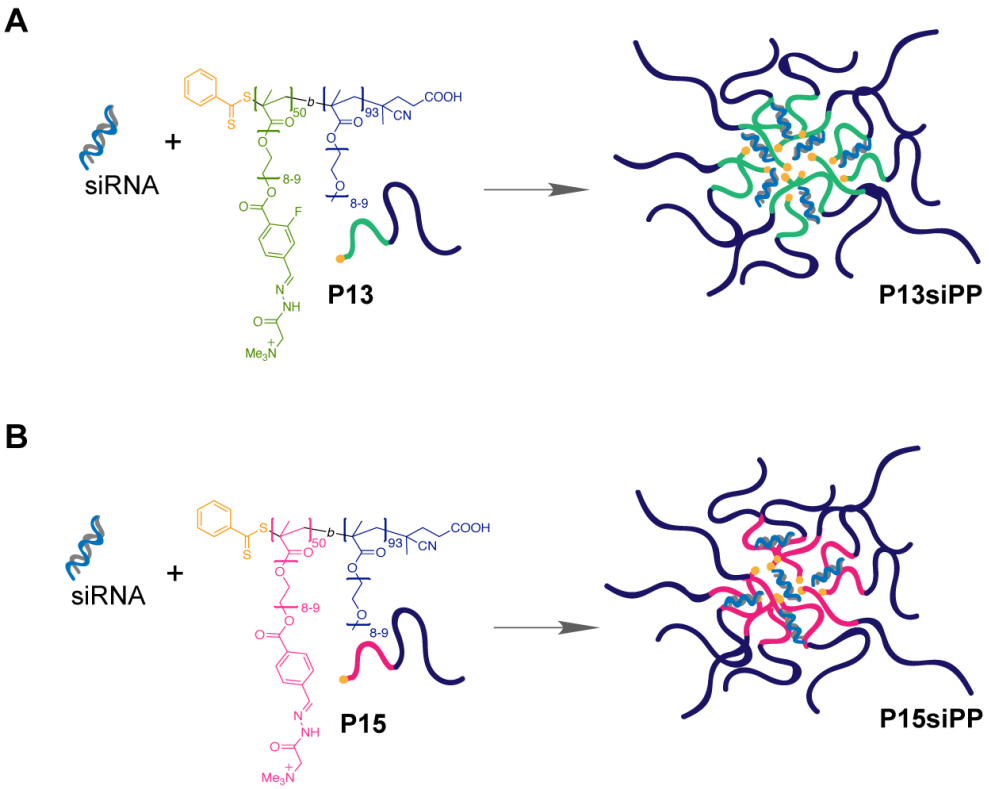

Figure 4.18: Preparation of polyplexes loading siRNA. Polymers (A) **P13** and (B) **P15** were mixed with siRNA at different N/P ratios to obtain polyplexes **P13siPP** and **P15siPP**.

The concentration of the cationic polymers was varied to form polyplexes with N/P ratios of 0.5 to 20. The solutions were allowed to equilibrate at room temperature to promote the self-assembly of the polyplexes. Because of the electrostatic interactions between the positive charges of the cationic polymers and the negative charges of the

siRNA, the loading capacity of the polyplexes can be evaluated by a gel retardation assay. In this assay, agarose gel electrophoresis of the polyplexes was performed to evaluate the migration rate of nucleic acids in the presence of polycations **P13**/**P15**. Naked siRNA is used as a control and its migration rate on the gel is compared with the migration rate of the polyplexes. Polyplexes presenting high loading of siRNA show lesser mobility in the gel on account of the neutralisation of the negative charge and the larger size, and therefore, display retarded migration rates when compared with naked siRNA.[28] Polyplex **P13siPP** showed loading of siRNA at N/P ratios above 2 (Figure 4.19 A). At N/P ratio = 2 unloaded siRNA was still observed, however, when higher N/P ratios were used, the complete loading of siRNA was achieved (N/P ratios: 5, 10 and 20. Figure 4.19 A). **P15siPP** did not achieved loading of siRNA at any N/P ratios tested (Figure 4.19 B). Polymer **P15** displays only 16 units of the positive charge from its ammonium functional groups, whilst polymer **P13** displays 30 units of the positive charges of its ammonium functional groups. These observations suggest that at low densities of cations, siRNA complexation is not possible.

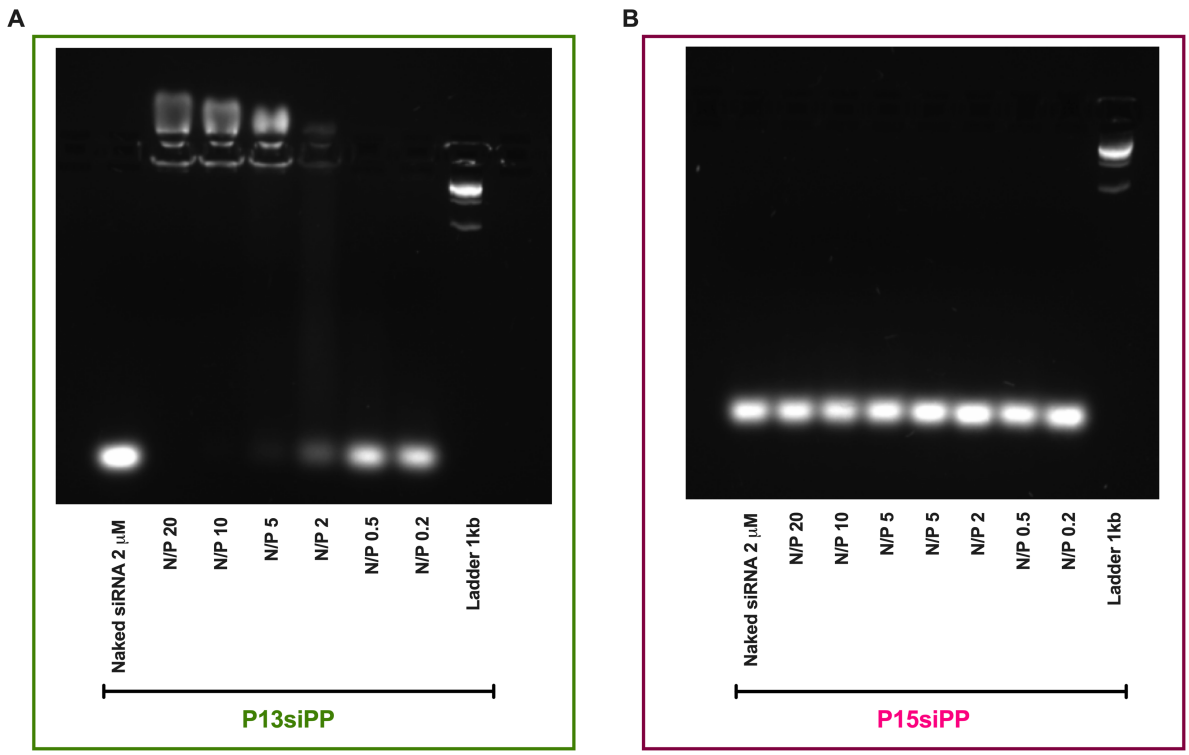

Figure 4.19: Gel retardation assay of (A) **P13siPP** and (B) **P15siPP**. Polyplexes were prepared by simply mixing aqueous solutions of **P13** or **P15** and siRNA. Agarose gel 3 % was prepared in TBE buffer 0.5 X and the samples were loaded onto the gel using DNA loading buffer. The electrophoresis was perfomer in TBE buffer 0.5 X at 80 V for 1 h.

Polyplexes using **P13** were characterised by DLS to determine the hydrodynamic diameters of the particles formed (Figure 4.20). All particles presented size ~ 30 nm with PdI > 0.5. The high polydispersity of the particles indicates that the complexation with siRNA, although successful, resulted in particles of a wide range of sizes, a feature that is not desirable for siRNA delivery.

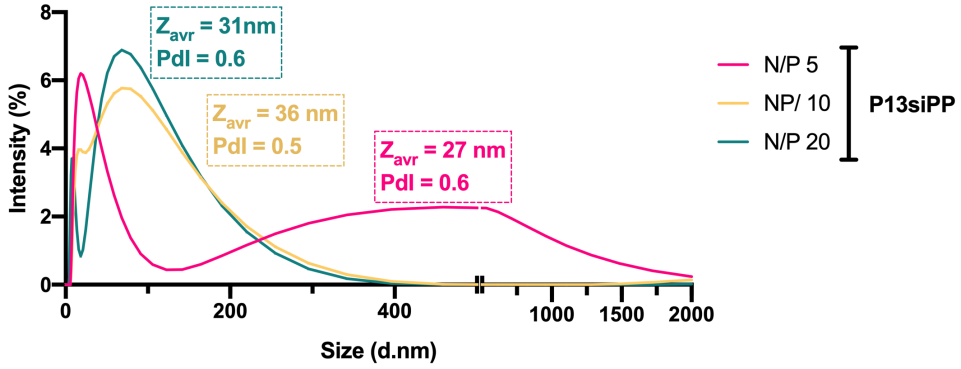

Figure 4.20: DLS Measurements of **P13siPP** (hydrodynamic diameter and PdI). The polyplexes were prepared by the self-assembly of **P13** and siRNA at N/P ratios of 5 (pink line), 10 (yellow line) and 20 (green line).

Polyplex formation is driven by two main factors: the electrostatic interactions between the positive charges of the cationic polymer and negative charges of the nucleic acids, and the entropy of the system.[29,30] The mode of addition of the components to spontaneously form polyplexes might influence the physicochemical properties of the formed particles. Subtle changes on the order of mixing (e.g. siRNA to polymer solution or polymer to siRNA solution)[29] or on the mode of addition (e.g. pipetting, vortex or dropwise addition)[31] may change particle size and improve polydisperse distribution. However, the process of polyplexes formation is not well understood[29,32] and further investigation is needed to elucidate the effect of the mode of adding the reagents on the physicochemical properties of polyplexes.

4.2.5 Conjugation of cationic/hydrazone polymers P3/P15 onto AuNPs and subsequent complexation with siRNA

Hydrazone polymers **P13** and **P15** were incubated with AuNPs of 20 nm size (Figure 4.21) to obtain **P13NPs** and **P15NPs**, respectively. The molar ratio of polymer to AuNPs was varied to determine the concentration of polymer needed to effectively shield the Au core. Salt-induced aggregation of AuNP-polymer conjugates was evaluated by addition of $NaCl_{(aq)}$ (1 M) followed by analysis of the UV-Vis spectrum. The aggregation factor was calculated by the ratio of the absorbance for aggregate

particles to the absorbance of bare 20 nm AuNPs ($\lambda_{615}/\lambda_{524}$). Thus, high values of aggregation factor imply significant levels of particle aggregation and insufficient polymer coating.

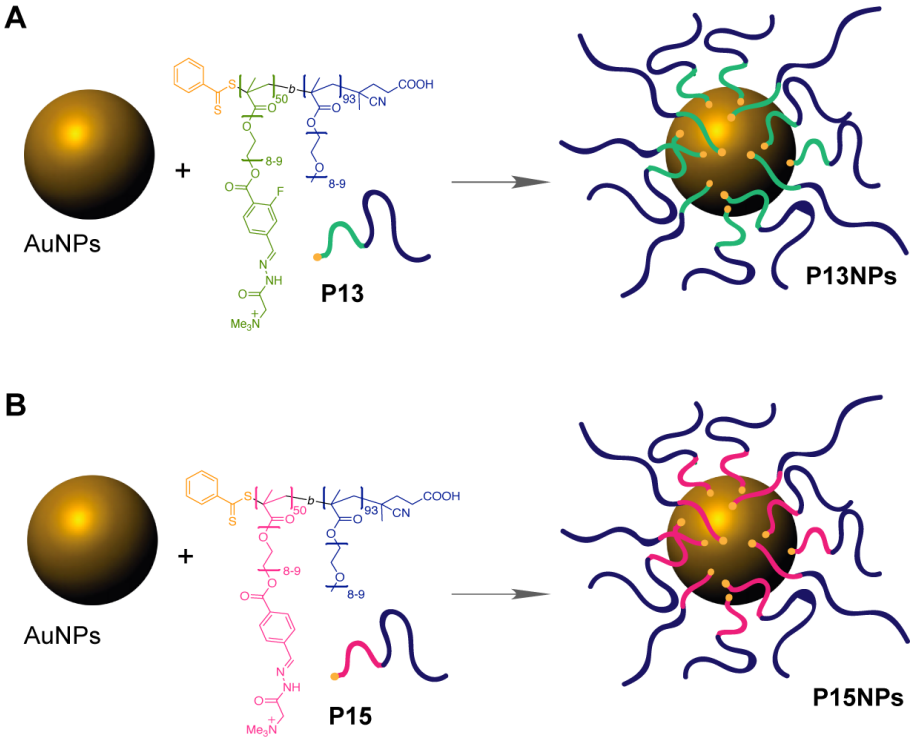

Figure 4.21: Preparation of AuNPs coated with hydrazone polymers **P13**/**P15**. Nanoparticles were first incubated with (A) **P13** or (B) **P15** and the concentration of polymer needed to successfully coat 20 nm AuNPs was determined (**P13NPs** and **P15NPs**).

Uncoated AuNPs were tested as a control, showing high aggregation factor values consistent with the expected salt-induced aggregation of citrate-stabilised AuNPs (Figure 4.22). For conjugates **P13NPs** (Figure 4.22 A) and **P15NPs** (Figure 4.22 B) molar ratios above 50 fold-excess showed lower values of aggregation factors after addition of $NaCl_{(aq)}$ (final conc. 100 mM), suggesting sufficient polymer coating of the Au nanoparticle core. The similar aggregation behaviour for particles coated with **P13** and **P15** was expected as both polymers presented similar molecular weights (M_n ~ 80 kDa). AuNP-polymer conjugates prepared using the molar ratios 1:100, 1:500 and 1:1,000 (AuNP:polymer) were selected for further characterisation by DLS (Figure 4.23). **P13NPs** showed an increase in the hydrodynamic diameter relative to uncoated AuNPs, with particle size ~ 50 nm for particles coated with 1:100 and 1:500 molar ratios and particle size ~ 70 nm for particles prepared at 1:1,000 molar ratio. Moreover, the nanocarriers presented narrow size distribution and low polydispersity (PdI = 0.2) (Figure 4.23 A). A similar behaviour was observed for **P15NPs**, where for

all molar ratios used, the particles resulted in average size ~ 70 nm and PdI = 0.3 (Figure 4.23 B).

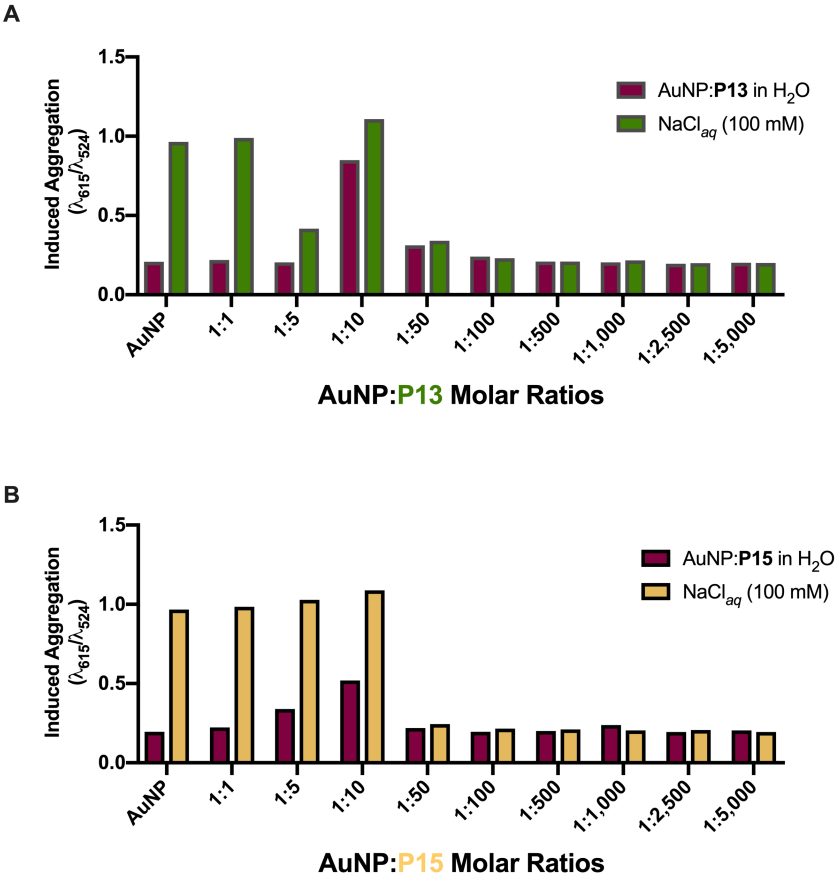

Figure 4.22: Stability of AuNPs coated with (A) **P13** and (B) **P15** at different polymer molar ratios in $NaCl_{(aq)}$ (1 M). Dark red bars show the aggregation factors obtained from UV-Vis experiments of AuNP-polymer conjugates in H_2O. (A) Green and (B) yellow bars represent the aggregation factors after addition of $NaCl_{(aq)}$ (1 M).

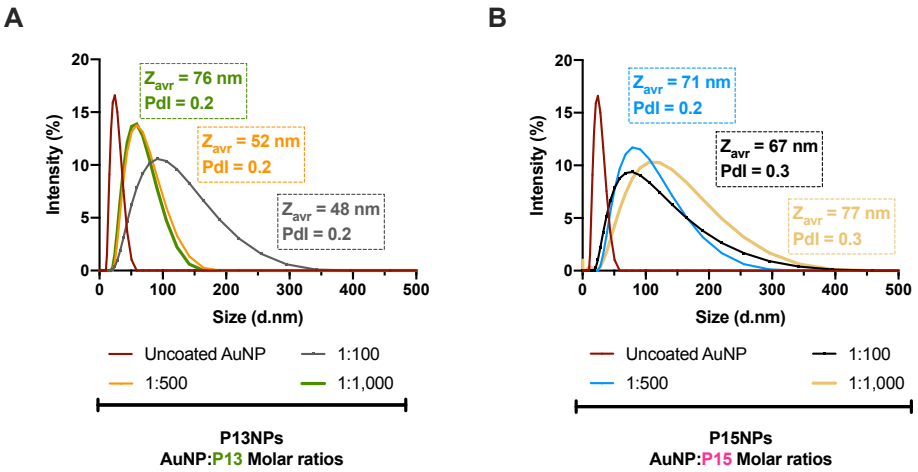

Figure 4.23: Characterisation by DLS of AuNPs coated with (A) **P13** and (B) **P15** at different molar ratios. Particles were prepared by incubation of AuNPs with hydrazone polymer at 1:100, 1:500 and 1:1,000 molar ratios.

4.2.6 Complexation of nanocarriers with siRNA

Polymer-coated AuNP **P13NPs** and **P15NPs** were purified by centrifugation and then incubated with siRNA to obtain **P13siNPs** or **P15siNPs** at different N/P ratios (Figure 4.24). The nanoparticles were named according to nomenclature in Figure 4.25.

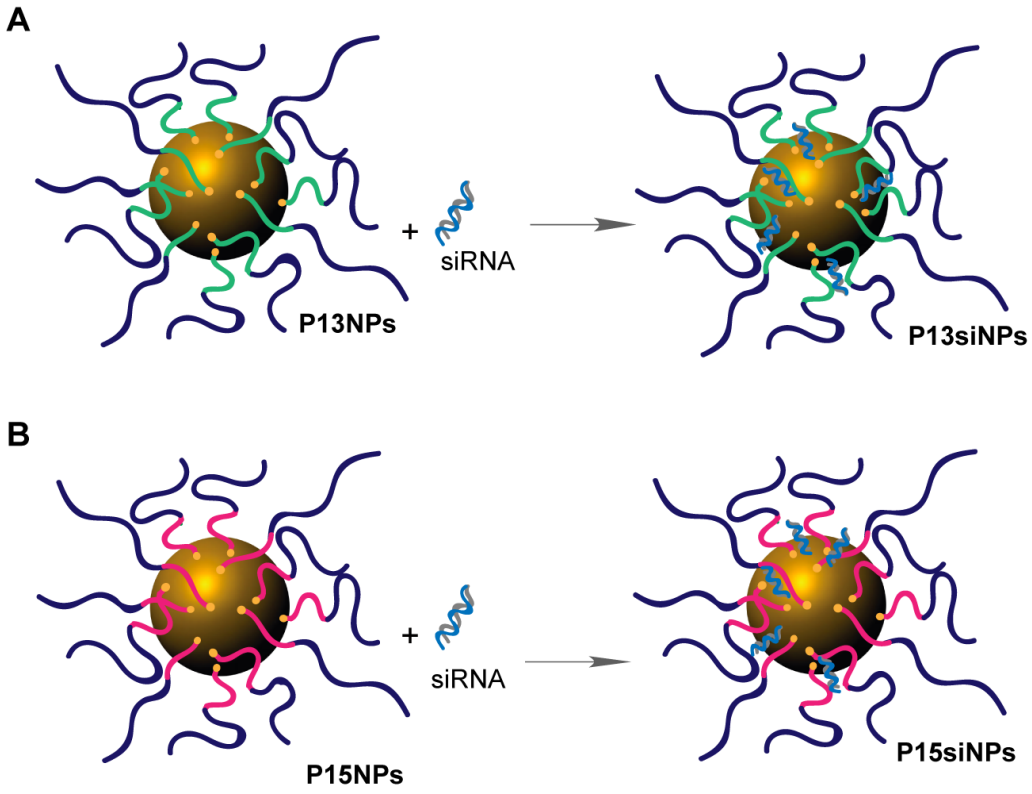

Figure 4.24: Preparation of nanoparticles loaded with siRNA. **P13NPs** and **P15NPs** were incubated with siRNA at different N/P ratios to obtain the nanocarriers **P13siNPs** and **P15siNPS**.

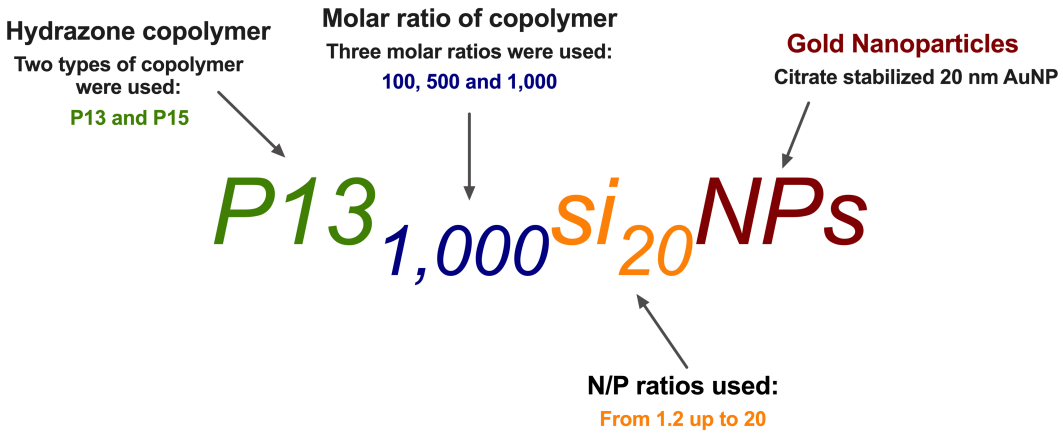

Figure 4.25: Nanoparticle nomenclature. AuNPs were coated with **P13** or **P15** in different molar ratios. After purification, the particles were incubated with siRNA at different N/P ratios to evaluate the loading efficiency of the nanocarriers.

The particles were isolated by centrifugation and the supernatant was collected for quantification of the amount of unloaded siRNA. This method allows an indirect quantification of the amount of siRNA loaded to the particles, and thus, it is possible to calculate the loading efficiency of the nanocarriers. **P13$_{100}$si$_2$NP** and **P13$_{500}$si$_5$NP** did not show loading of siRNA (Figure 4.26 A). The final N/P ratios for these particles were 2 and 5 respectively. However, when more polymer was added to AuNPs (**P13$_{1,000}$si$_{20}$NPs**), the N/P ratio increased to 20, and 60 % of siRNA loading was achieved (Figure 4.26 A). For **P15siNPs**, the particles did not load siRNA for any of the N/P ratios tested (Figure 4.26 B). These results correlate with the gel retardation assay showed in Figure 4.19, where for polyplexes **P13siPP**, high loading of siRNA was observed for N/P ratio > 5 (Figure 4.19 A) and no siRNA loading was observed for polyplexes **P15siPP** (Figure 4.19 B).

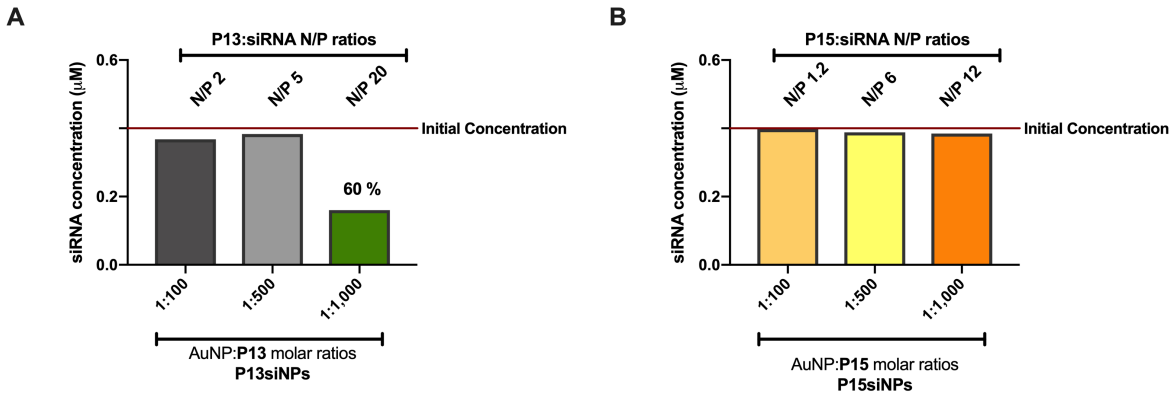

Figure 4.26: Quantification of unloaded siRNA in the supernatants of (A) **P13siNPs** and (B) **P15siNPs**. Unloaded siRNA was determined using a Qubit miRNA assay kit. The red line represents the initial concentration of siRNA added to the formulation.

To evaluate the pH-response of the nanocarriers, **P13$_{1,000}$si$_{20}$NP** were purified by centrifugation and washed three times with Hepes buffer at pH 7.4. The particles were then incubated in phosphate buffer 10 mM at pH 7.0 and pH 5.0. After 24 h, the particles were isolated by centrifugation and the supernatant collected for quantification of siRNA released from the nanocarriers. Figure 4.27 shows the quantification of siRNA after incubation in buffer at pH 7.0 (blue bar) and at pH 5.0 (pink bar). This data indicates that **P13$_{1,000}$si$_{20}$NP** did not alter the siRNA release at any pH, suggesting that the hydrazone polymer is not pH-responsive and that it is likely no C=N bonds hydrolysed, even at pH 5.0. This result is in agreement with the pH-sensitivity screening of hydrazones presented in Figure 4.8, where the hydrazones tested did not hydrolyse when the pH was lowered, even at pH 1.0. Although in the

experiment using **P13$_{1,000}$si$_{20}$NP** much lower concentrations of hydrazone were used (μM concentrations was used for the pH-responsiveness of nanoparticles, whilst mM concentrations were used for the pH-sensitivity of model hydrazones) the hydrazones bonds remained stable at pH 5.0.

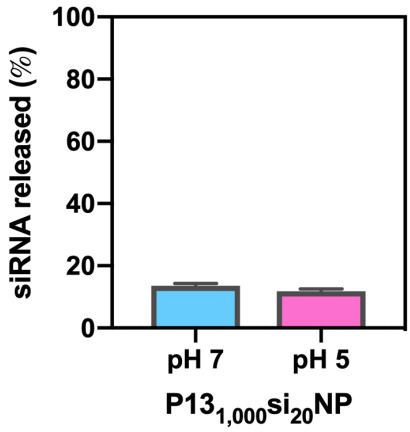

Figure 4.27: Quantification of siRNA released from **P13$_{1,000}$si$_{20}$NPs** at pH 7.0 (blue bar) and at pH 5.0 (pink bar). The samples were isolated by centrifugation and the supernatant collected to determine the amount of siRNA released. The siRNA was quantified using the QuBit miRNA assay kit and the fluorescence readings were obtained at the green emission.

The lack of pH-sensitivity of **P13$_{1,000}$si$_{20}$NP** at pH 5.0 discourages the use of hydrazones as pH-responsive bonds for endosomal release. These findings are in contradiction with the examples in the literature for hydrazones bonds used for siRNA delivery[8,33–35] which claim successful release in acidic environment (tumour loci or endosome vesicle). The pH-sensitivity screening for hydrazones (Figure 4.8) and imines (Figure 4.11) provided a new insight on the design of acid-labile bonds for specific pH-response. The imine **I7** appears to be a promising candidate as a component of a pH-sensitive nanocarrier for siRNA delivery. Therefore, the synthesis of a diblock copolymer featuring an electron withdrawing substituent on the aldehyde moieties is important to evaluate the pH-sensitivity of these bonds for siRNA applications. The imine polymer can be conjugated onto AuNPs to further complexation with siRNA. The pH-sensitivity test can be performed, followed by gene knockdown *in vitro* to determine the capability of the delivery platform to successfully release siRNA into the cytosol of the target cell, and it is hoped this idea will be the topic of future work.

4.3 Conclusions

Work towards the development of a new pH-responsive nanocarrier was discussed. Molecules featuring acid-labile hydrazone or imine bonds were prepared and their stabilities at different pH values were evaluated. The hydrazones tested did not show the appropriate pH-sensitivity for endosomal release, even when a destabilizing EDG was introduced on the aldehyde reaction partner. In fact, the pH hydrolysis experiments showed that hydrazones formed from aromatic aldehydes did not hydrolyse even at pH 1.0, discouraging the use of these bonds for siRNA delivery platforms. These observations are contrary to some described previously in the literature.[8–12] A possible explanation could be attributed to the lower concentration used in delivery platforms (μM and nM) when compared to organic molecules at mM concentrations. These pH-responsive bonds are sensitive to concentrations and usually more hydrolysis occur in diluted conditions. Moreover, several reports in the literature demonstrate the pH-response using amphiphilic polymers. On account of their amphiphilic nature it is possible to assume that only a fraction of the bonds are hydrolysed, decreasing the necessary hydrophobicity of the system to maintain the micelle form and thus, the micelle disassemble occurs releasing the cargo at a specific pH.

The pH hydrolysis profile identified imines **I1** and **I7** as potential candidates as pH-sensitive moieties to be conjugated on nanocarriers. The pH hydrolysis profiles at equivalent molar ratios of the reaction partners showed that the equilibrium position is shifted towards the starting materials when compared with the pH hydrolysis profiles using 10-fold excess of the amine reaction partner. The EWG substituent on the aldehyde reaction partner of **I7** increased the stability of the imine bond, suggesting **I7** is of potential use within a delivery platform due to its adequate pH-sensitivity (stable at pH 7.0 and hydrolysed at pH 5.0). Interestingly, the pH-sensitivity of model imine **I1** changed when it was incorporated within a polymer system, indicating that model studies must also be done within the polymer in addition to the small molecules. After evaluation of the pH hydrolysis profiles at equivalent molar ratios, model imine **I1** showed poor stability at neutral and acidic pH. However, its stability improved when the compound was appended onto the random copolymer **P4**. These observations suggested the polymers featuring imines **I1** and **I7** would be suitable candidates for incorporation into a siRNA delivery platform, since it displays good stability at physiological conditions and hydrolysis in acidic environments. Moreover, the difference of the pH-sensitivity of model compounds *vs* polymer systems was an

important finding, since polymeric architectures are generally components of delivery platforms.

RAFT Polymerisation was performed to obtain diblock copolymer scaffolds with good level of control. The copolymer post-modifications to obtain a diblock featuring cations upon one of the block was successfully achieved by a two-step reaction.

After its complexation with siRNA, the hydrazone copolymer (**P13**) featuring ~ 30 positive charges showed efficient siRNA loading, whilst the copolymer **P15** (~ 16 positive charges) did not show complexation with siRNA. This observation demonstrates that siRNA complexation does not occur at low densities of cations. Moreover, the copolymers were successfully conjugated onto AuNPs resulting in particles presenting ~ 50 – 70 nm size (**P13NP** and **P15NP**). Particles loaded with siRNA (**$P_{1,000}si_{20}NP$**) did not release siRNA at pH 5.0. The stability at pH 7.0 and 5.0 of the polymer-Au conjugates loaded with siRNA confirms the lack of pH-sensitivity of hydrazone bonds demonstrated by the pH-sensitivity screenings of the model hydrazone bonds.

Taken together these studies showed the potential application of pH-sensitive imine bonds for siRNA delivery, as model imine **I7** showed promising pH-response in acidic pH and stability at physiological pH. The synthesis of a diblock copolymer featuring **I7** moieties presents as a potential component within the delivery platform, performing multiple functions to overcome the biological barriers (e.g. prolonged circulation and endosomal escape) associated with *in vivo* siRNA delivery, a feature that is essential for the successful application of siRNA as therapeutics.

4.4 References

1 K. A. Whitehead, R. Langer and D. G. Anderson, *Nat. Rev. Drug Discov.*, 2009, **8**, 129–138.

2 L. Huang and S. Guo, *J. Nanomater.*, , DOI:10.1155/2011/742895.

3 A. A. Kale and V. P. Torchilin, *Bioconjug. Chem.*, 2007, **18**, 363–370.

4 C. Bouillon, Y. Bessin, F. Poncet, M. Gary-Bobo, P. Dumy, M. Barboiu, N. Bettache and S. Ulrich, *J. Mater. Chem. B*, 2018, **6**, 7239–7246.

5 M. E. Belowich and J. F. Stoddart, *Chem. Soc. Rev.*, 2012, **41**, 2003–2024.

6 R. Nguyen, *Chem. Commun.*, 2003, **8**, 942–943.

7 J. Kalia and R. T. Raines, *Angew. Chemie - Int. Ed.*, 2008, **47**, 7523–7526.

8 Y. Bae, N. Nishiyama, S. Fukushima, H. Koyama, M. Yasuhiro and K. Kataoka, *Bioconjug. Chem.*, 2005, **16**, 122–130.

9 J. M. Priegue, D. N. Crisan, J. Martínez-Costas, J. R. Granja, F. Fernandez-Trillo and J. Montenegro, *Angew. Chemie - Int. Ed.*, 2016, **55**, 7492–7495.

10 A. Aissaoui, B. Martin, E. Kan, N. Oudrhiri, M. Hauchecorne, J. P. Vigneron, J. M. Lehn and P. Lehn, *J. Med. Chem.*, 2004, **47**, 5210–5223.

11 G. F. Walker, C. Fella, J. Pelisek, J. Fahrmeir, S. Boeckle, M. Ogris and E. Wagner, *Mol. Ther.*, 2005, **11**, 418–425.

12 L. He, Y. Jiang, C. Tu, G. Li, B. Zhu, C. Jin, Q. Zhu, D. Yan and X. Zhu, *Chem. Commun.*, 2010, **46**, 7569–7571.

13 H. Schiff, *Justus Liebigs Ann. Chem.*, 1864, **131**, 118–119.

14 C. Godoy-Alcántar, A. K. Yatsimirsky and J. M. Lehn, *J. Phys. Org. Chem.*, 2005, **18**, 979–985.

15 C. Wang, G. Wang, Z. Wang and X. Zhang, *Chem. - A Eur. J.*, 2011, **17**, 3322–3325.

16 L. Marin, D. Ailincai, M. Calin, D. Stan, C. A. Constantinescu, L. Ursu, F. Doroftei, M. Pinteala, B. C. Simionescu and M. Barboiu, *ACS Biomater. Sci. Eng.*, 2016, **2**, 104–111.

17 C. Monfardini and F. M. Veronese, *Bioconjug. Chem.*, 1998, 9, 418–450.

18 J. Lee, P. E. Saw, V. Gujrati, Y. Lee, H. Kim, S. Kang, M. Choi, J. Il Kim and S. Jon, *Theranostics*, 2016, **6**, 192–203.

19 S. B. Yong, H. J. Kim, J. K. Kim, J. Y. Chung and Y. H. Kim, *Sci. Rep.*, 2017, **7**, 133–791.

20 Chemicalize, Chemicalize - Instant Cheminformatics Solutions, https://chemicalize.com/, (accessed 28 July 2019).

21 S. Santos, *J. Mol. Pharm. Org. Process Res.*, 2015, **03**, 1–2.

22 J. V. M. Weaver, I. Bannister, K. L. Robinson, X. Bories-Azeau, S. P. Armes, M. Smallridge and P. McKenna, *Macromolecules*, 2004, **37**, 2395–2403.

23 R. Longenecker, T. Mu, M. Hanna, N. A. D. Burke and H. D. H. Stöver, *Macromolecules*, 2011, **44**, 8962–8971.

24 N. Vanparijs, L. Nuhn and B. G. De Geest, *Chem. Soc. Rev.*, 2017, **46**, 1193–1239.

25 A. Bordat, T. Boissenot, J. Nicolas and N. Tsapis, *Adv. Drug Deliv. Rev.*, 2019, **138**, 167–192.

26 J. F. Lutz, *J. Polym. Sci. Part A Polym. Chem.*, 2008, **46**, 3459–3470.

27 D. J. Gary, N. Puri and Y. Y. Won, *J. Control. Release*, 2007, 121, 64–73.

28 Y. Wu, W. Wang, Y. Chen, K. Huang, X. Shuai, Q. Chen, X. Li and G. Lian, *Int. J. Nanomedicine*, 2010, **5**, 129–136.

29 D. W. Pack, A. S. Hoffman, S. Pun and P. S. Stayton, *Nat. Rev. Drug Discov.*, 2005, **4**, 581–593.

30 V. A. Bloomfield, *Biopolymers*, 1997, **44**, 269–282.

31 D. Pezzoli, E. Giupponi, D. Mantovani and G. Candiani, *Sci. Rep.*, 2017, **7**, 44134.

32 S. T. Chou, K. Hom, D. Zhang, Q. Leng, L. J. Tricoli, J. M. Hustedt, A. Lee, M. J. Shapiro, J. Seog, J. D. Kahn and A. J. Mixson, *Biomaterials*, 2014, **35**, 846–855.

33 H. Zhu, W. Liu, Z. Cheng, K. Yao, Y. Yang, B. Xu and G. Su, *Int. J. Mol. Sci.*, 2017, **18**, 2029.

34 C. Xu, H. Tian, H. Sun, Z. Jiao, Y. Zhang and X. Chen, *RSC Adv.*, 2015, **5**, 103380–103385.

35 I. Dovydenko, I. Tarassov, A. Venyaminova and N. Entelis, *Biomaterials*, 2016, **76**, 408–417.

5. Summary and Future Work

The development of new nanocarriers for siRNA delivery is the tipping point to translate the therapeutic potential of RNAi into clinical applications. In this work the development of nanocarriers based on the loading of phosphorothioate-modified siRNA onto AuNPs was demonstrated. The addition of one or three phosphorothioate modifications did not improve the loading of siRNA onto AuNPs. Studies from the literature indicates that a long polyA tail containing multiple phosphorothioate modifications is able to successfully bind onto AuNPs. Therefore, the addition of a phosphorothioate modified polyA tail in the 3'-end of the sense strand of the siRNA could be a promising strategy to overcome the challenges of loading siRNA onto AuNPs. However, long modifications on the siRNA sequence could interfere in RNAi mechanism, impeding the AGO2 binding sites. Furthermore, long siRNA strands are associated with PKR activation and consequently, cytotoxicity. Thus, further studies needed to be conducted to assess the RNAi efficiency of siRNAs containing phosphorothioate modified polyA tail. The studies will be conducted as shown below:

- Evaluation of RNAi efficiency of siRNAs containing a phosphorothioate modified polyA tail at the 3'-end of the sense strand;
- If the sequences shown the required RNAi efficiency (> 50%), the evaluation of the length and number of phosphorothioate modifications needed to successfully conjugate onto AuNPs will be assessed;
- If successful, the optimal formulation (stable nanocarriers with high loading of siRNA (> 50 %) will be tested *in vitro* and *in vivo*.

The use of cationic copolymers featuring pH-responsive moieties presents a promising strategy to overcome the endosomal escape challenges. This work demonstrated that model imine bonds showed advantageous pH-sensitivity for triggered release in the acidic environment of the endosome. Therefore, further studies should be performed to better understand and optimise the pH-sensitivity of these bonds. The evaluation of the kinetic rates of hydrolysis at a range of pH values would bring further knowledge for the optimisation of the pH-sensitivity. In particular, the kinetic rates of hydrolysis at pH 7.4 and pH 5.5 would be interesting to estimate the stability of the acid-labile bonds for *in vivo* applications, and also estimate the rates of siRNA release. Furthermore, the post-functionalisation of polymer scaffolds to obtain imine moieties will be performed. The conjugation of these polymers onto AuNPs would facilitate the evaluation of this platform for siRNA delivery, and thus, studies of siRNA release at different pH values and evaluation of gene knockdown *in vitro* will be

developed to assess the efficacy of the delivery platforms for siRNA applications. Lastly, for the siRNA therapy to be successful for the treatment of acute myeloid leukaemia, the addition of functional targeting ligands in the delivery platform must be achieved for the selective accumulation of the particle into the target cells. The polymer chains will be functionalised with sialic acid residues targeting the over-expressed CD33 receptor found on leukemic cells. The active targeting of the delivery platform will be assessed *in vitro* and *in vivo* by cellular uptake and gene silencing assays. In summary, the main studies to be conducted are described below:

- Kinetics evaluation of imines at pH 7.4 and 5.5;
- Synthesis of polymers featuring imine bonds
- Development of nanocarriers based on AuNPs and cationic copolymers;
- Evaluation of the siRNA release rates of nanocarriers at pH 7.4 and 5.5;
- Evaluation of the gene and protein silencing *in vitro* and *in vivo*;
- Synthesis of cationic copolymers featuring sialic acid residues for the targeting of AML cells;
- Evaluation of cellular uptake of target and non-target nanocarriers *in vivo*;
- Evaluation of gene and protein silencing of target and non-target nanocarriers *in vivo*.

6. Appendix A

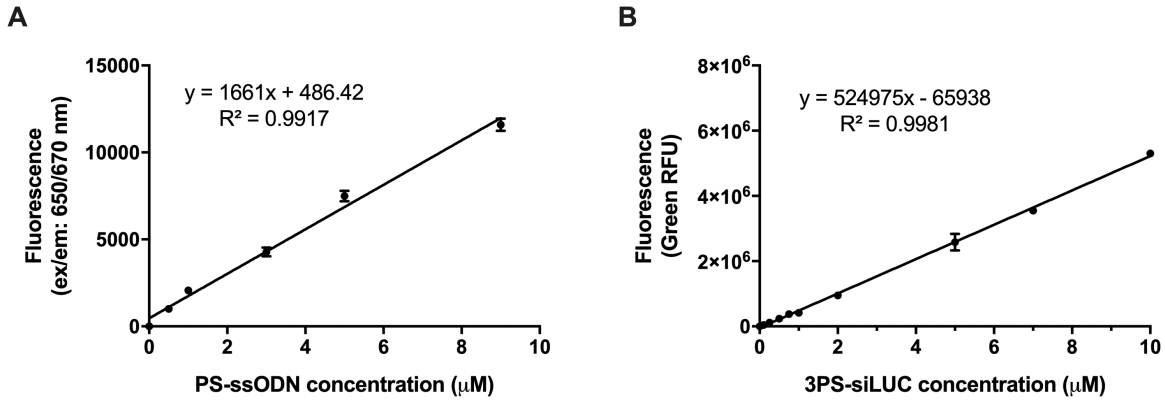

Figure A.1: Standard-curves of (**A**) Cy5-labelled **PS-ssODN** determined by fluorescence spectroscopy and (**B**) 3PS-siRNA targeting the *luciferase* gene (3PS-siLUC) determined using the QuBit miRNA assay.

7. Appendix B

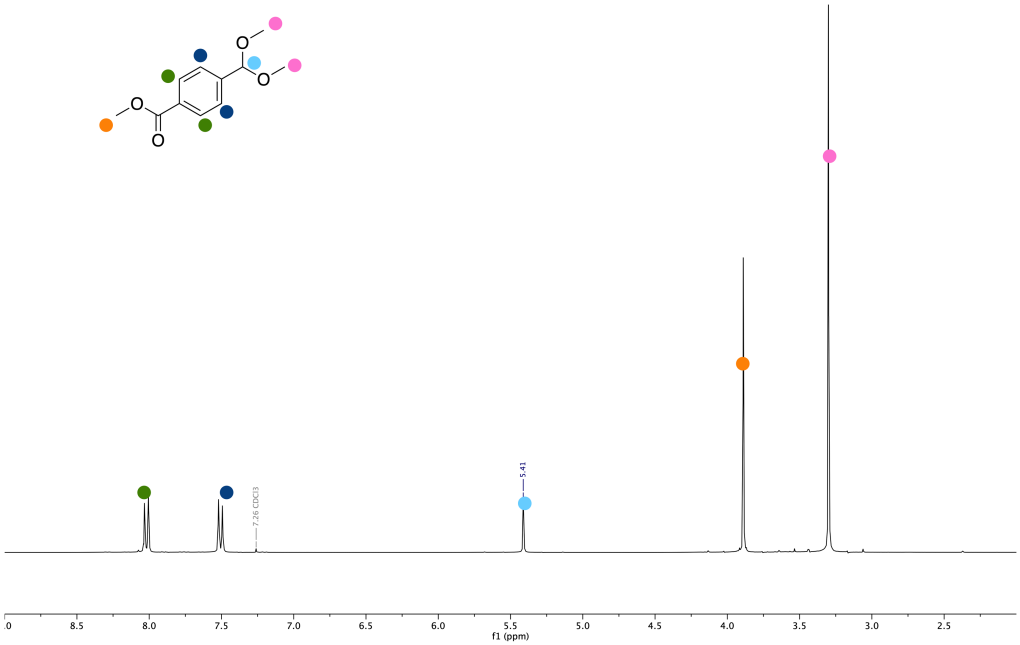

Figure B.1: ^{1}H NMR spectrum (300 MHz, $CDCl_3$) of compound **a**.

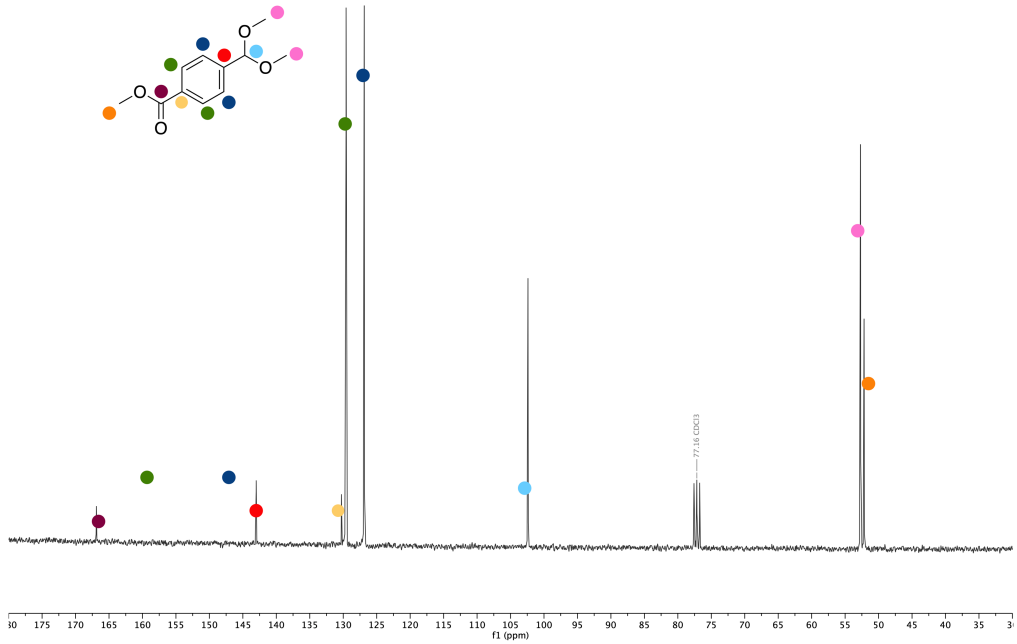

Figure B.2: ^{13}C NMR spectrum (75 MHz, $CDCl_3$) of compound **a**.

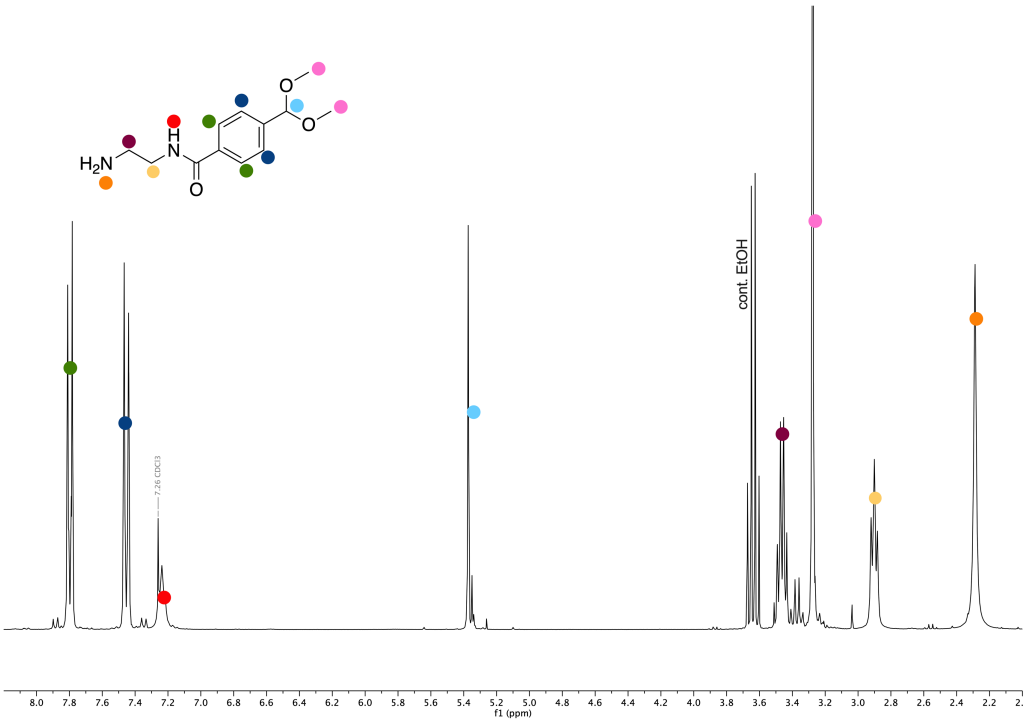

Figure B.3: ^{1}H NMR spectrum (300 MHz, $CDCl_3$) of compound **b**.

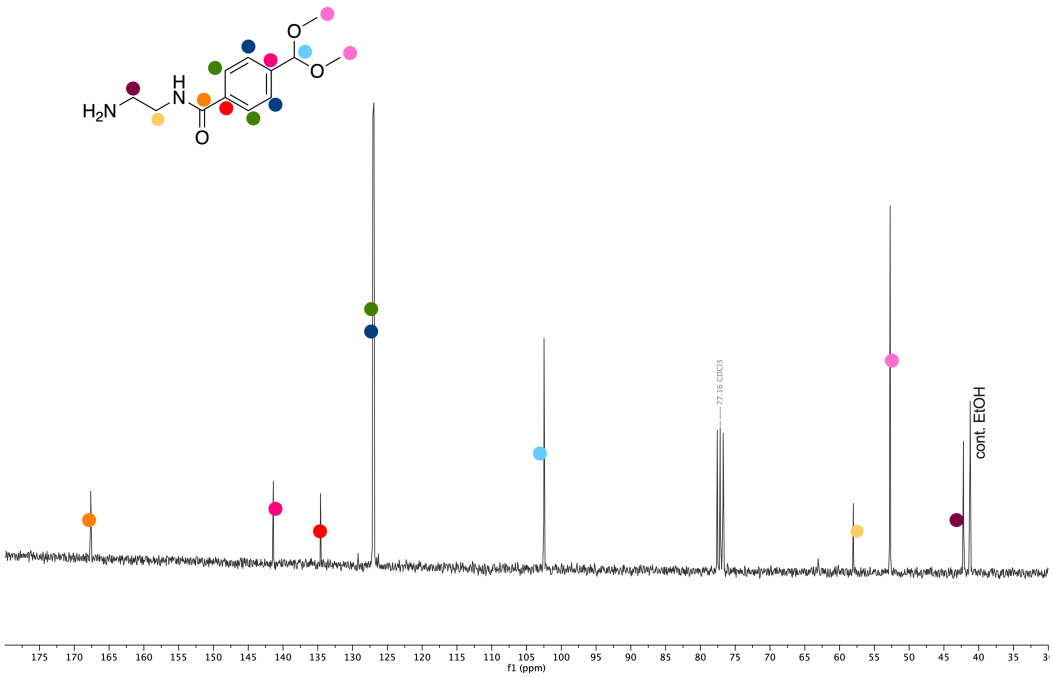

Figure B.4: ^{13}C NMR spectrum (75 MHz, $CDCl_3$) of compound **b**.

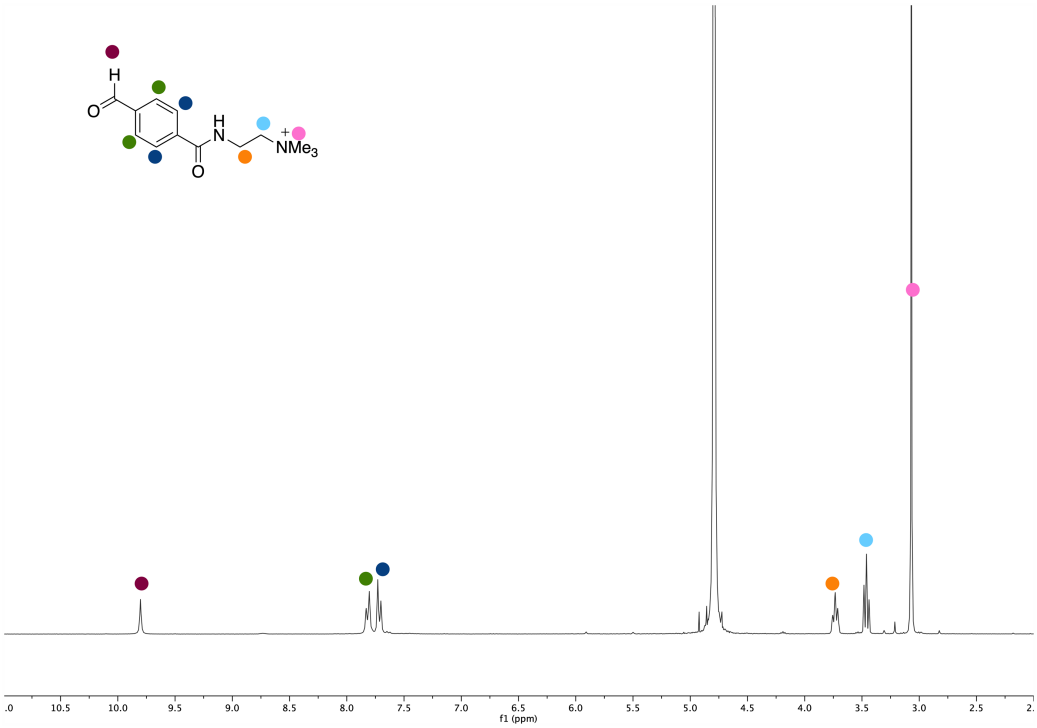

Figure B.5: ^{1}H NMR spectrum (300 MHz, D_2O) of aldehyde **A1**.

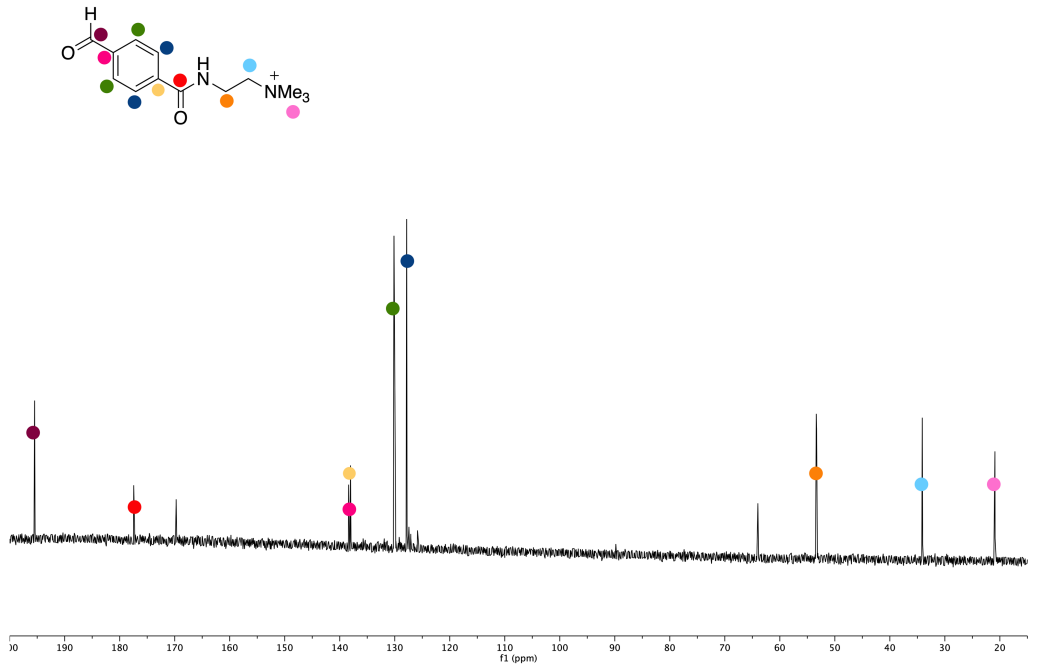

Figure B.6: ^{13}C NMR spectrum (75 MHz, D_2O) of aldehyde **A1**.

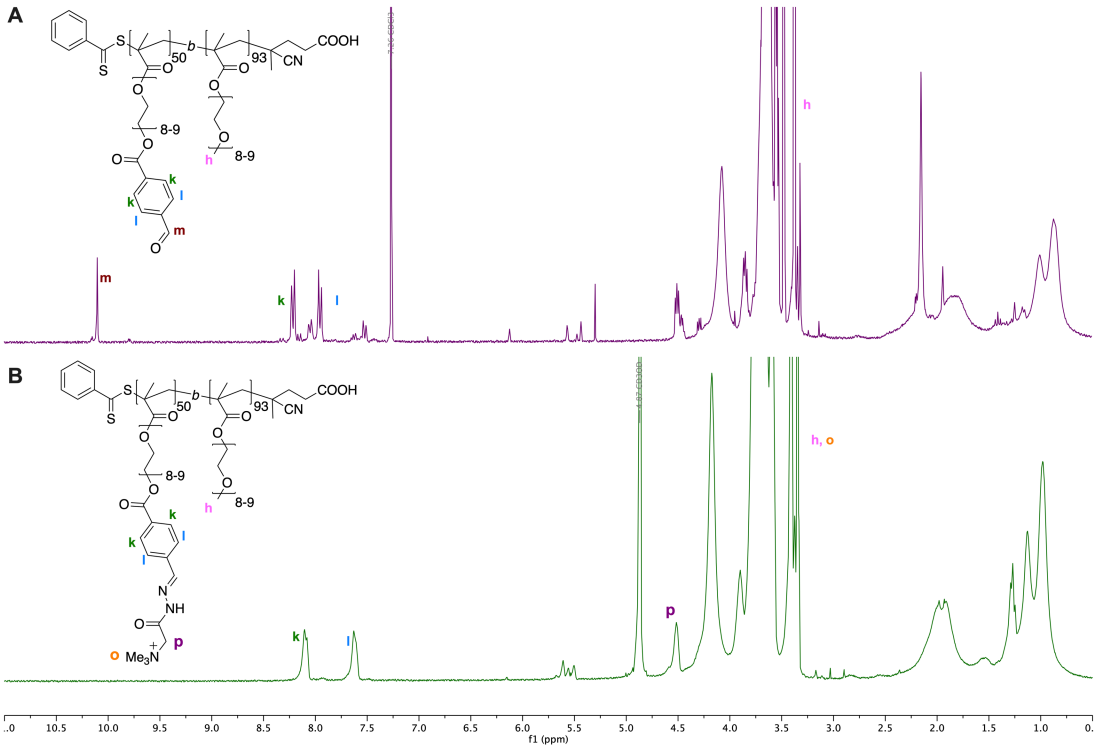

Figure B.7: ^{1}H NMR spectrum of (A) (300 MHz, $CDCl_3$) aldehyde-functionalised copolymer **P14** and (B) (300 MHz, D_2O) hydrazone-functionalised copolymer **P15**.